CONJUGATED POLYMER ACTUATORS AND SENSORS: MODELING, CONTROL, AND APPLICATIONS

By

Yang Fang

A DISSERTATION

Submitted to
Michigan State University
in partial fulfillment of the requirements
for the degree of

DOCTOR OF PHILOSOPHY

Electrical Engineering

2009

ABSTRACT

CONJUGATED POLYMER ACTUATORS AND SENSORS: MODELING, CONTROL, AND APPLICATIONS

By

Yang Fang

Conjugated polymers are soft actuation and sensing materials with promising applications in biomedical devices and micromanipulation systems. However, their sophisticated electro-chemo-mechanical dynamics and nonlinear behaviors present significant challenges in such applications. This dissertation is focused on using systems and control tools to address these challenges. In particular, a systems perspective is taken to model the dynamic and nonlinear behavior of conjugated polymer actuators and sensors, an adaptive control scheme is developed to handle model uncertainties, and a conjugated polymer actuated-micropump is explored both as an interesting application and a platform for validating and extending proposed models. Experimental results on trilayer polypyrrole (PPy) actuators and sensors are presented throughout the dissertation to support the modeling and control studies.

On the modeling aspect, a linear, partial differential equation (PDE) is first used to capture the ion transport dynamics in actuation and sensing. With proper boundary conditions, the PDE is solved to derive an infinite-dimensional transfer function model that is geometrically scalable and amenable to model reduction. Nonlinear behaviors, in both electrical and mechanical domains, are also modeled. In particular, on the electrochemical side, a reduction-oxidation (redox) level-dependent impedance model is obtained by applying perturbation analysis to a nonlinear PDE. On the mechanical side, a nonlinear elasticity theory-based framework is proposed to capture the mechanics involved in large deformation. The framework has not only been effective in modeling a bending actuator, but also motivated the study of a novel, torsional actuator that is based on a fiber-directed PPy tube.

On the control aspect, a robust adaptive control scheme is proposed to tackle the time-varying behavior of conjugated polymer actuators. Based on a reduced, linear model, a self-tuning regulator with parameter projection is designed and implemented. The robust adaptive control scheme has shown in experiments its superiority to traditional PID control schemes and a fixed model-following scheme.

Finally, the application of conjugated polymer actuators to micropumps is explored. A conjugated polymer-actuated diaphragm micropump is designed and fabricated. In contrast to a typical design of clamping an actuation membrane at all edges, a novel, petal-shaped diaphragm design is proposed to alleviate the effect of edge constraints. Transfer function models from the actuation voltage to the diaphragm curvature and to the flow rate are obtained and verified experimentally. A flow rate of 1260 μL/min is achieved for the new diaphragm design, which represents a significant improvement over the traditional design.

DEDICATION

TO MY PARENTS AND MS. FANG XIE.

ACKNOWLEDGMENT

I am very grateful to my advisor Dr. Xiaobo Tan for his careful and kind guidance. His vision and expertise have influenced me a lot during my PhD study, and will also benefit me in the future. I also would like to appreciate his generous help on my job search and career development.

I would like to thank Professor Hassan Khalil, Professor Ning Xi, and Professor Thomas Pence for serving on my advisory committee. Their insightful comments on my research are greatly appreciated. I would like to thank Professor Thomas Pence in particular. His class of Nonlinear Elasticity and his personal guidance enabled me to finish the work on modeling mechanical nonlinearity in this dissertation. I would like to thank Prof. Gürsel Alici at University of Wollongong for providing PPy samples and valuable advice on my research, which contributed to successful completion of this dissertation.

I am grateful to my colleagues in Smart Microsystems Lab: Zheng Chen, Dr. Mart Anton, Stephan Shatara, Freddie Alequin, Alex Esbrook, Dawn Hedgepeth, Chris Gliniecki, John Thon, Andrew Temme, Qingsong Hu, Ernest Mbemmo, and Alex Will. I also would like to thank friends at Michigan State who have offered me generous help: Hua Deng, Guokai Zeng, Li Sun, Yue Huang, Zongliang Cao, Yixin Wang and many others.

I would like to acknowledge the financial support of my research by NSF CAREER grant (ECCS 0547131) and MSU IRGP (05-IRGP-418).

Finally I would sincerely thank my parents Xiaolong Fang and Linhua Liu, and Ms. Fang Xie. It is their support and love that encouraged me to finish this dissertation successfully.

TABLE OF CONTENTS

LIST OF TABLES

LIST OF FIGURES

Chapter 1

Introduction

1.1 Background on Conjugated Polymers

Electroactive polymers (EAPs) are promising actuation and sensing materials with potential applications in robotics and biomedical systems [1–6]. One class of EAP materials are conjugated polymers or conducting polymers [7–9], which are unusual organic materials that exhibit electronic conductivity. In 1977, Hideki Shirakawa, Alan G. MacDiarmid, Alan J. Heeger and coworkers reported high conductivity conjugated polymer, which eventually rewarded them with the 2000 Nobel prize in Chemistry. Polypyrrole (PPy) and polyaniline (PANI) are two of the most investigated conjugated polymers, because of their good chemical stability and substantial strains. The chemical structures of PPy and PANI are shown in Fig. 1.1 and Fig. 1.2. The backbones of conjugated polymers have alternating single and double carbon-carbon bonds (conjugation), which results in positive charge carriers and thus electrical conductivity. Those charge carriers must overcome a band gap in order to be delocalized and thus enable conduction. The band gap is reduced by doping, which involves the addition of charges (dopants) to or removal of charges from the polymer chain. The doping is generally performed chemically or electrochemically. In chemical doping, dopants are donated to or repelled from the polymer backbone through chemical reactions

with dopant molecules.

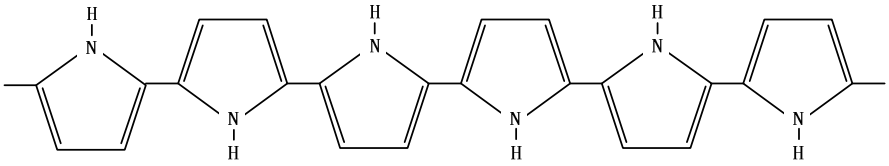

Figure 1.1: The chemical structure of polypyrrole.

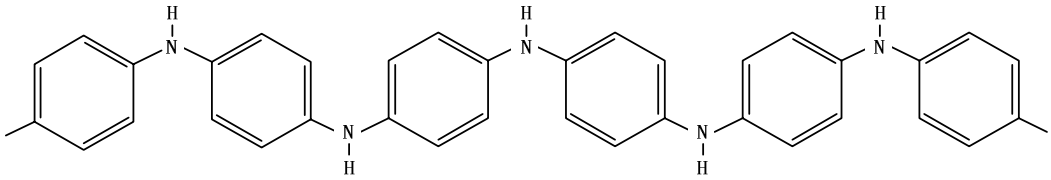

Figure 1.2: The chemical structure of polyaniline.

A conjugated polymer can be electrochemically doped by placing it in contact with an electrode in the electrolyte. When a sufficiently positive potential is applied, electrons are removed from the polymer, and negatively charged anions are incorporated into or positively charged cations are repelled from the polymer backbone to maintain the charge neutrality. Application of a sufficiently negative potential can reverse the process and repel the trapped anions out of or return the cations back to the polymer (reduction). The oxidation/reduction process is called redox, and these cations or anions are called dopants. The mass transport induced by ion movement during redox is considered to be the primary mechanism responsible for volumetric change and thus the actuation of conjugated polymers [7, 8]. The redox process of PPy involving anions can be described as

$$\begin{aligned} \text{Oxidation: } \mathrm{PPy} + \mathrm{A}^- &\rightarrow \mathrm{PPy}^+\mathrm{A}^- + \mathrm{e}^- \\ \text{Reduction: } \mathrm{PPy}^+\mathrm{A}^- + \mathrm{e}^- &\rightarrow \mathrm{PPy} + \mathrm{A}^-, \end{aligned}$$

where PPy represents the neutral state of polypyrrole and PPy^+ is the oxidized state, A^- represents the dopant anions, $\mathrm{PPy}^+\mathrm{A}^-$ indicates that A^- is incorporated into the polymer,

and e^- denotes an electron. Note that an anion-transporting conjugate polymer will expand during oxidation and contract during reduction, while a cation-transporting polymer will demonstrate the opposite behavior.

Conjugated polymer actuators have the following attractive features:

- can be actuated under very low voltages (typically 2 V or less).
- have large strains (3% in-plane to 30% out-of-plane) and considerable stress.
- can operate in liquid electrolytes, including body fluids.
- lightweight and biocompatible.

Linear extenders have been made by immersing a single piece of conjugated polymer in electrolyte [7, 10]. As the potential difference is changed between the polymer and electrolyte, the volume of the conjugated polymer will change, so it can be used to generate linear motion. The bending motion can be generated with a bilayer configuration [8]. When the conjugated polymer layer is expanded or shrunk by accepting or repelling ions, the substrate layer does not change. Due to the strain mismatch within the two layers, the bilayer structure will bend. However, these two configurations require electrolyte environments. A trilayer bender can work without this limitation [11], as illustrated in Fig. 1.3. In the middle is an amorphous, porous polyvinylidene fluoride (PVDF) layer that serves both as a backing material and a storage tank for the electrolyte. On both sides of the actuator are the PPy layers. When a voltage is applied across the actuator, the PPy on the anode side is oxidized while that on the cathode side is reduced. The oxidized layer absorbs anions and expands, while the reduced layer gives up anions and contracts. The differential expansion thus leads to bending of the actuator, as shown in Fig. 1.3 (right).

Conjugated polymers can be used as electrochemical sensors, because of the significant electrical conductivity change over several orders of magnitude in response to change in pH, humidity, or binding to biomolecules. These electrochemical sensors are based on the

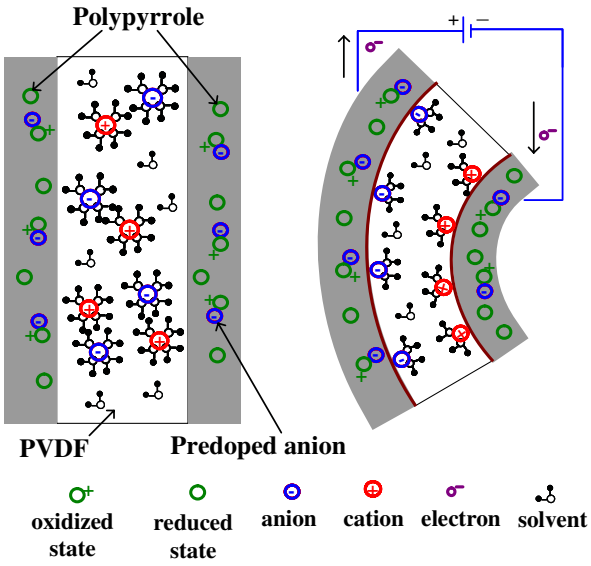

Figure 1.3: Illustration of the actuation mechanism of a trilayer polypyrrole actuator. Left: the sectional view of the trilayer structure; right: bending upon application of a voltage.

property changes of the single and double carbon-carbon structure while interacting with chemical compounds [12].

The conjugate polymers can also be used as electromechanical sensors where an open-circuit voltage or a short-circuit current is generated under deformation. Comparing with the more extensive work on conjugated polymer actuators, the understanding of the electromechanical sensing property of conjugated polymer is still in its infancy, where theory and models are needed to explain and quantify the phenomenon. We will explore a theory to explain the electromechanical sensing capability of conjugated polymer in this thesis.

1.2 Fabrication of Trilayer Conjugated Polymer

Fabrication of trilayer conducting polymer is achieved by electrochemically oxidizing pyrrole monomer from a solution to grow PPy layers on either side of a gold-coated porous PVDF film, which acts as the working electrode. The porous PVDF films are obtained from Sigma-Aldrich, which has the thickness of 110 μm with pore size of 0.45 μm. It is

coated with a thin layer of gold (approximately 100 nm) by using the sputtering coater in W. M. Keck microfabrication cleanroom at Michigan State University. This ensures a good conductivity therefore good electrochemical growth of PPy. The electrolyte is a solution of 0.1 M pyrrole, 0.1 M Li^+TFSI^- in Propylene Carbonate (PC) with 0.5w/w% water. Note that the solution with Li^+TFSI^- will dope the PPy with $TFSI^-$. The dopant can be changed to other ions, such as PF_6^-, by changing Li^+TFSI^- to the salt containing these ion, such as $TBA^+PF_6^-$.

A potentiostat is used in the electrochemical deposition, which is a control and measuring device that keeps the potential of the working electrode at a constant level with respect to the reference electrode in the electrolyte. The one used in the Smart Microsystems Lab is Omni 101B from ESA Biosciences Inc. The cell is a cubic glass container by joining glass together with glass sealant. Two stainless steel meshes are used as the counter electrode and the PVDF membrane is sandwiched between them to ensure even PPy deposition. A part of the film is left protruding out of the electrolyte for electrical connection. The experiment setup is shown in Fig. 1.4, and one piece of fabricated trilayer conjugated polymer is shown in Fig. 1.5.

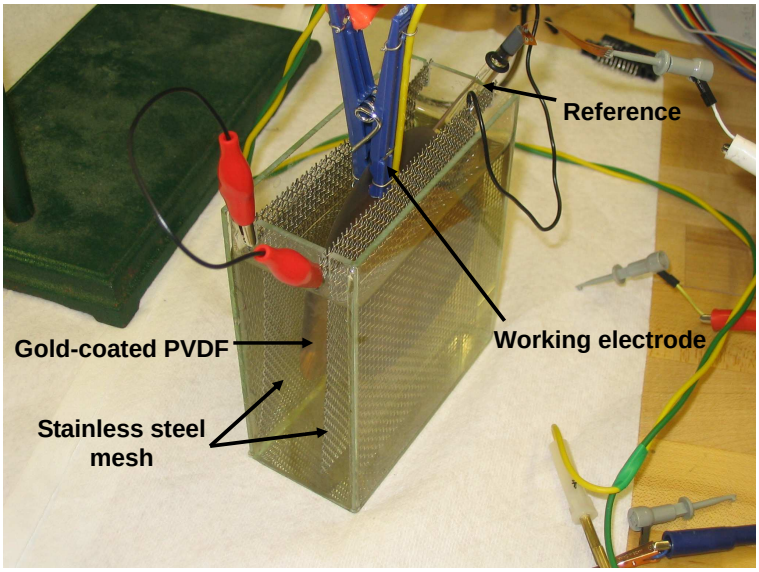

Figure 1.4: The setup for fabricating trilayer conjugated polymer.

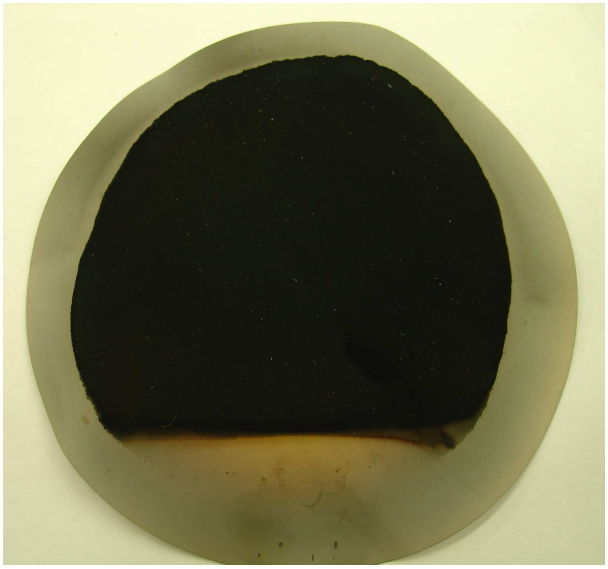

Figure 1.5: Fabricated sample of trilayer conjugated polymer.

After the samples are fabricated, the thickness of the PPy layer can be measured by using the digital imaging system in W. M. Keck microfabrication cleanroom at Michigan State University, which consists of a SPOT digital color camera and an Olympus BX60 optical microscope. The sectional view of the sample is captured by the imaging system, which also includes the measurement tool to obtain the dimensions. One image captured is shown in Fig. 1.6.

1.3 Research Objectives

In this dissertation, we will focus on modeling, control, and application of conjugated polymer actuators and sensors. To fully utilize conjugated polymer in bio/micro manipulation, bio-sensing, and micro robotics, it is crucial to understand the actuation and sensing properties of conjugated polymer. Therefore the first objective is to obtain a physics-based but control-oriented mathematical model for conjugated polymer, which captures its major dynamics and is useful for applications as actuator and sensor. In many applications, large deformation of actuators are required to achieve the tasks. Therefore, the second ob-

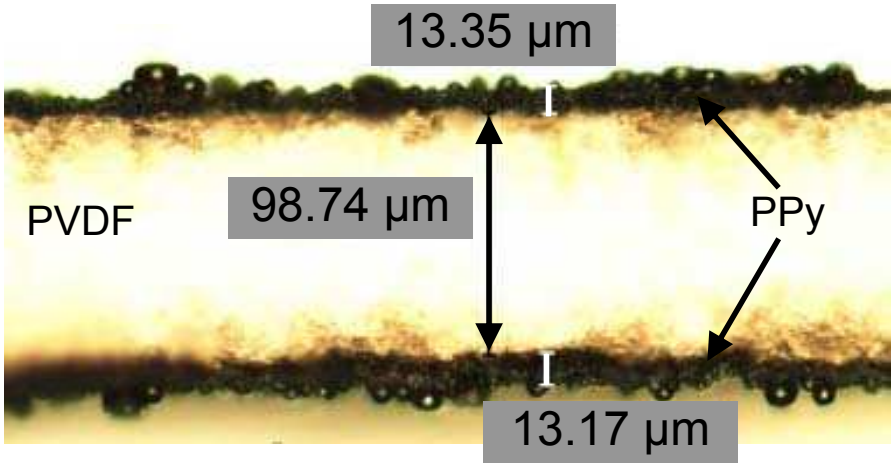

Figure 1.6: Thickness of layers of a trilayer PPy actuator measured with a microscope.

jective is to understand the nonlinearities in conjugated polymer actuators, which become more significant as a higher input voltage is applied to generate larger deformation. The third objective is to utilize feedback control in conjugated polymer-based system to tackle the uncertainties and allow precise control of the actuator, because actuator behaviors are heavily influenced by the materials and processes used during fabrication as well as the environmental conditions during operation. The fourth objective is to explore the use of conjugated polymer in promising applications. In this thesis, the application of conjugated polymer in micropump is explored, because microfluidic devices are in significant development in recent years, and conjugated polymer actuators provide an important potential mechanism for realizing compact micropumps with low actuation voltages.

PPy is used throughout this study. However, we expect that most of the results are directly applicable or can be extended to other conjugated polymer materials.

1.4 Contributions

1.4.1 Linear Models for Actuation and Sensing

Conjugated polymer actuators require low actuation voltage (about 1 V), generate considerable stress and large strain output, and are light and biocompatible. These advantages make them attractive for a wide range of robotic and biomedical applications, such as micro and biomanipulation, biomimetic systems, and biomedical devices [2–4, 8]. For all these applications, it is highly desirable to have quantitative models available that can predict quasi-static and dynamic actuation performance in terms of intrinsic material parameters and actuator dimensions. Such models will be useful in feasibility analysis, design optimization, and even actuator control. Alici and coworkers investigated modeling and geometry optimization of bending curvature and force output for trilayer PPy actuators [11, 13, 14]. Christophersen *et al.* characterized and modeled the bending curvature for bilayer PPy microactuators of different dimensions [15]. All these studies were focused on quasi-static operating conditions, where the bending curvature and/or force output were examined in terms of material stiffness and actuator geometry.

In this thesis, we have developed a scalable, control-oriented model for trilayer conjugated polymer that captures the major electrochemomechanical dynamics. This model consists of three modules: 1) electrochemical dynamics module, adapted from the diffusive-elastic-metal model of Madden [16]; 2) stress-generation module relating transferred charges to internal actuation stress; and 3) mechanical dynamics module. Scaling laws for key parameters of the electrical admittance model are developed, rendering the complete model expressible in intrinsic material parameters and actuator dimensions. Experiments are conducted on trilayer conjugated polymer actuators of different dimensions to validate the scalable model for quasi-static force and displacement output, electrical admittance, and dynamic displacement response.

Comparing with the extensive work on modeling of conjugate polymer actuators [6, 16–

19], research on modeling of conjugate polymers as electromechanical sensors has been relatively limited. Wu *et al.* [20] investigated the sensing behavior of a trilayer PPy beam by considering the perturbation of the Donnan equilibrium of the ion distribution by mechanical stimuli as the primary sensing mechanism. A similar viewpoint was also presented by Takashima and coworkers [21]. For better understanding of the sensing mechanisms, however, quantitative modeling of the sensing dynamics is desired.

We have investigated the dynamic sensing behavior of conjugated polymers. The model derivation starts with a partial differential equation (PDE) that governs the ion redistribution dynamics subject to diffusion and migration (due to electrostatic interactions). However, for real-time sensing applications, it is desirable to have an analytical model. For this purpose, we linearized and solved this PDE analytically in the Laplace domain, which leads to a transfer function that relates the open-circuit sensing voltage to the applied mechanical deformation. Experimental measurement of the open-circuit voltage matches the model prediction reasonably well. This work provides the first step towards fundamental understanding of mechanical sensing mechanisms of conjugated polymers.

1.4.2 Modeling Nonlinearities in Conjugated Polymer Actuators

Nonlinearities in conjugated polymer actuator become significant as a relatively high input voltage is applied. Nonlinearity exist in both electromechanical and mechanical domains.

In electromechanical domain, the redox level, i.e., the amount of ions incorporated in the conjugated polymer during reduction-oxidation, has significant impact on the electromechanical properties and dynamics of the material and consequently the actuation performance. While the effect of redox level on conductivity and Young's modulus has been documented [15, 22–26], its influence on dynamics of ion transport is more subtle and has received inadequate attention in terms of fundamental understanding and modeling.

We have developed a redox level-dependent impedance model for conjugated polymers, which is physically based yet has a compact, explicit form. We start with a governing par-

tial differential equation (PDE) that incorporates the dynamics of ionic diffusion, ionic migration, and redox reactions. The PDE is linearized around a given redox level via perturbation analysis, and an exact, analytical solution is obtained by converting the PDE into the Laplace domain and enforcing appropriate boundary conditions. This model captures double-layer charging, diffusion, and migration effects. Experiments have shown that the proposed model are comparable to the diffusive-elastic-metal model [16] when the redox level is low, but shows clear advantage in predicting the impedance at higher redox levels.

In the mechanical domain, the classical beam theory has been used to model the bending curvature for bilayer PPy actuators [15,27] and trilayer actuators [17]. However, this linear elastcity-based model is only valid when the ion movement-induced swelling is small so that: 1) the strain and the stress can be related linearly; 2) the geometry nonlinearities can be neglected. Alici and coworkers modeled the bending curvature and force output for trilayer PPy actuators by using finite element analysis in analogy with a thermally driven beam, but no analytical model was presented [28]. The tensile strength experiments have shown that the strain and stress relationship of PPy film becomes clearly nonlinear as the strain is increased over 4% [29,30]. These results indicate that the linear model based on the assumption that the stress varies linearly with the strain becomes invalid as the deformation gets large. Therefore, it is imperative to develop a nonlinear model to predict the actuator performance for the applications where large actuation is involved.

In this thesis, a nonlinear elasticity-based method is proposed to capture the mechanical deformation induced by transferred ions. Neo-Hookean type strain energy functions are used for both PPy and PVDF to capture the nonlinear stress-strain relationship, which incorporates the effect of swelling [31]. The actuation-induced stresses are derived from the strain energy functions. The equilibrium configuration under a quasi-static actuation voltage is then obtained by solving the force and moment balance equations simultaneously. Experiments have shown that when the applied voltages are small, predictions by both models are close to experimental data. But the nonlinear elasticity model fits the ex-

perimental data better as the input voltage increases, which shows the superiority of the method in modeling large deformations of conjugated polymers.

Different configurations of conjugated polymer actuators have been exploited, including bilayer and trilayer benders [8, 32], linear extenders [7]. However, more complicated actuator motions will be required. Fiber-directed material can generate torsional motion because of the anisotropy associated with the interaction between the fibers and the material matrix [33].

We fabricated a fiber-directed conjugated polymer tube by integrating platinum wires into conjugated polymer during the deposition process of conjugated polymer. We have further proposed a nonlinear elasticity-based model to capture the relationship between the actuation voltage and the torsional motion of the conjugated polymer tube. Compared with a linear elasticity-based model, this model is able to capture the complicated deformations and large deformation. The model has been verified with experimental measurements by using samples with different sizes.

1.4.3 Control of Conjugated Polymer Actuators

It is critical to precisely control the force and/or displacement output of conjugated polymer actuators in many of their intended applications such as manipulation of single cells and micro-surgical operations. There has been extensive work on understanding the actuation mechanism of conjugated polymers as well as improving their actuation performance (strain output, strain rate, force output, work per cycle, lifetime, etc.) [7–9, 34]. However, control and control-oriented modeling of conjugated polymers remain largely unexplored. A proportional controller was used by Qi *et al.* to speed up the transient responses of an polyaniline actuator [35]. P. Madden treated the actuation dynamics as a first-order system and designed a PID controller for a polypyrrole actuator, where his main interest was to demonstrate a feedback loop consisting of polypyrrole actuator and sensor [17]. Taking again a first-order empirical model, Bowers did simulation studies on PID and adaptive

control of conjugated polymers, but no experimental results were presented [36]. The primitive state of conjugated polymer control study is mainly dictated by the sophisticated electrochemomechanical processes during redox reactions, which makes it challenging to have a physical (non-empirical) model suitable for real-time control. In addition, actuator behaviors are difficult to characterize since they are heavily influenced by the materials and processes used during fabrication as well as the environmental conditions (temperature, humidity, electrolyte, etc.) during operation.

In this thesis, we have developed a robust adaptive control scheme for conjugated polymer actuators with demonstrated performance in trajectory tracking experiments. A key component of the work is a simple model structure reduced from a full, infinite-dimensional physical model through model reduction, which captures essential actuation dynamics and is amenable to efficient real-time control. It enables compact, embedded controller implementation for various micro, robotic, or biomedical applications. The resulting model is of second order with a zero, after we further discarding a pole and a zero considering the typical range of physical parameters. A recursive-least squares algorithm is then used to identify online the parameters of the reduced model. A self-tuning regulator [37] is designed based on the identified parameters to make the closed-loop system follow a reference model. A parameter projection step ensures that the parameter estimates stay within the physically-meaningful region, and thus makes the system robust against measurement noises, and unmodeled dynamics and nonlinearities. Experiments are conducted when the conjugated polymer actuator is operating in air, where its actuation behavior shows significant variation over time because of the solvent evaporation. Experimental results have shown that the proposed scheme is superior to the commonly used PID scheme and to the fixed model-following scheme in terms of both tracking accuracy and required control effort.

1.4.4 Conjugated Polymer Micropump

Microfluidic devices have been a topic of extensive research in recent years because of the significant development of biomedical industry. For many microfluidic systems, micropumps are desired to integrate and simplify complex analytical procedures. The methods of actuation that have been investigated mainly include electroosmotic pumps, centrifugal pumps, and diaphragm pumps. An electroosmotic pump induces motion of liquid by applying a voltage across a capillary tube, which drags the clustered ions in the liquid and consequently the fluid. However, its application is limited by the drawback that fluid flow cannot be generated when the ion concentration is below 10^{-5} M or above 10^{-2} M [38]. Centrifugal pumps are not very effective for fluid flows with low Reynolds numbers and have only been miniaturized to a limited size [39]. Diaphragm pumps have shown promise because of their compact sizes and the ability to deliver different kinds of fluid precisely. Different actuation mechanisms and materials have been investigated for diaphragm micropumps. A thermopneumatic micropump utilizes an electric heater to increase the chamber temperature and therefore the pressure which leads to fluid flow [40], but the bandwidth of the device is limited by the heating and cooling process. Electrostatic actuation [41], piezoelectric films [42], and P(VDF-TrFE) based electroactive polymer [43] have been explored, but the high actuation voltages required may change the properties of the samples. Shape memory alloy thin film was also proposed [44], but the possible damage to the fluid sample due to the high transition temperature hindered its use in biological applications.

We present a novel, conjugated polymer petals-actuated diaphragm micropump, which is in contrast to the typical whole diaphragm design [43,45,46]. We show through modeling analysis that the new design, by alleviating the edge constraints, can provide significantly larger diaphragm deformation and consequently the higher flow rate. The modeling of mechanical module for the diaphragm is developed using the energy method [47], which incorporates the elastic energy stored in the diaphragm and the work done on the fluid by the

diaphragm. The final model for the petal-shape diaphragm pump, after model reduction, is represented as a finite-dimensional transfer function that captures the fundamental physics of conjugated polymer actuators and their interactions with flexible diaphragm and fluid. The rest of the pump is fabricated through PDMS-based MEMS processes. Experiments are conducted to evaluate the pump performance and the effectiveness of the model.The measured admittance, deformation curvature, and flow rate are found to match the models well. The complete model predicts that there is an optimal operating frequency to generate the largest flow rate, which is verified in experiments.

1.5 Chapter Descriptions

The electrochemomechanical dynamics of conjugated polymer actuators and sensors are investigated in Chapter 2, where the nonlinearities are ignored and transfer function models are presented to capture the actuation and sensing dynamics. The nonlinearities in both electromechanical and mechanical domains are modeled in Chapter 3. The redox level is introduced to capture the nonlinearity in the electrical domain, while nonlinear elasticity is used to model the mechanical nonlinearity. A fiber-directed conjugated polymer actuator that can generate torsional motion is also proposed in Chapter 3. Its deformation is modeled by using nonlinear elasticity-based method. In Chapter 4 a robust adaptive control methodology is presented based on the proposed actuation model, and experimental results are provided to verify the effectiveness of the control strategy. The application of conjugated polymer actuator in a micropump is studied in Chapter 5, where both modeling and experiments are conducted to investigate the micropump performance. The conclusion of this dissertation is provided in Chapter 6.

Chapter 2

Linear Models for Conjugated Polymer Actuators and Sensors

The complete actuator model consists of three modules: 1) the electrical admittance module relating the current (and thus the charge transferred) to the voltage input; 2) the electromechanical coupling module expressing the generated stress in terms of the transferred charge; and 3) the mechanical module connecting the stress to the displacement or force output. This structure is shown in Fig. 5.7, where V is the input voltage, I is the current, ε is the corresponding strain, and Y is the mechanical output.

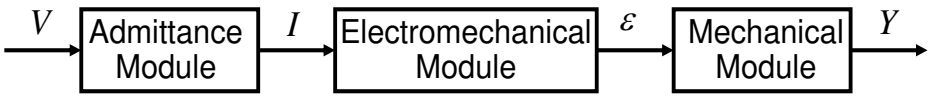

Figure 2.1: The complete model structure for conjugated polymer actuators.

2.1 Electrical Admittance Module

It is desired to obtain the electrical admittance module relating the current (and thus the charge transferred) to the voltage input in order to obtain the complete actuation model.

Consequently, one will be able to predict the mechanical output of the actuator under the applied voltage. There are two possible mechanisms for the accumulated anions to enter the polymer matrix, diffusion and migration. J. Madden proposed a diffusive-elastic-metal model for one piece of PPy immersing in the electrolyte, where it was assumed that the polymer matrix is perfectly conducting and the ion transport within the polymer is solely determined by diffusion [16]. This model can be adapted to model the trilayer PPy actuator in our work and shows good agreement with experimental data for a wide frequency range from 10^{-4} to 10^{5} Hz.

2.1.1 Review of Diffusive-elastic-metal Model and Adaptation to the Trilayer PPy Actuator

Firstly, the method in [16] is briefly described. And then we present a different and more straightforward derivation of the final admittance expression than the one in [16].

The voltage input of the actuator is applied across the two PPy layers. This produces a potential difference between each PPy layer and the electrolyte, as illustrated in Fig. 2.2(a). Note that only one side of the PPy is in contact with the electrolyte. Under the potential difference, the anions in the electrolyte migrate toward the polymer, which results in double-layer charges at the polymer/electrolyte interface - like a double-layer capacitance with an equivalent thickness of δ. Fig. 2.2 (b) shows an equivalent circuit model of the polymer impedance, where the faradaic current has been ignored. C denotes the double-layer capacitance at the polymer/electrolyte interface, R is the electrolyte and contact resistance, and Z_D represents the "diffusion impedance", which will be clarified in the derivation below.

In the Laplace domain the total current $I(s)$ in the circuit is the sum of the double-layer charging current $I_C(s)$ and the current $I_D(s)$ diffusing into polymer:

$$I(s) = I_C(s) + I_D(s). \tag{2.1}$$

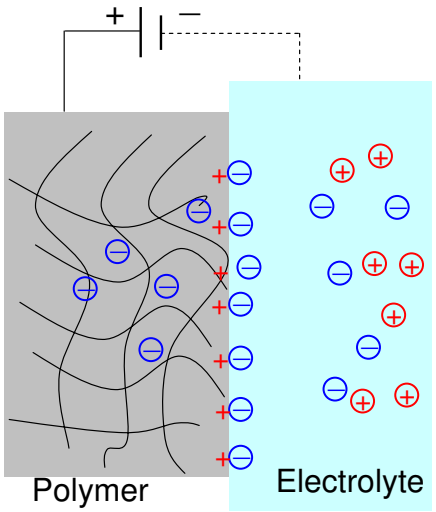

(a)

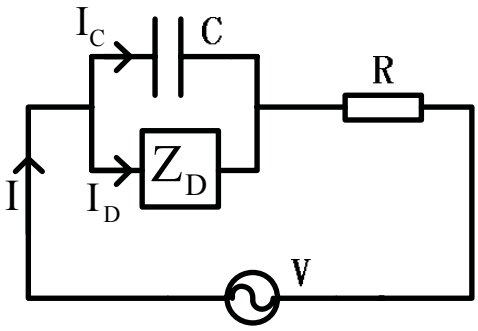

(b)

Figure 2.2: (a) Illustration of double-layer charging and diffusion for a conjugated polymer film with one side in contact with electrolyte; (b) equivalent circuit model for the polymer impedance.

The Kirchhoff's voltage law gives

$$V(s) = I(s) \cdot R + \frac{1}{s \cdot C} \cdot I_C(s). \tag{2.2}$$

Let x denote the thickness direction of the polymer, with $x = 0$ representing the polymer/electrolyte interface. Assume that the ion concentration varies only in the x-direction, which will be denoted as $c(x,s)$. From Fick's law of diffusion, one has

$$I_D(s) = -F \cdot A \cdot d \cdot \frac{\partial c}{\partial x}(x,s)|_{x=0}, \tag{2.3}$$

where A is the surface area of the polymer, F is the Faraday constant, d is the diffusion coefficient, and $\frac{\partial c}{\partial x}(x,s)|_{x=0}$ represents the gradient of ion concentration at the interface. To compute $I_C(s)$, one first calculates the charges $Q_C(s)$ stored in the double-layer capacitor. Assume that the double layer has a thickness δ and that the ion concentration within the (thin) double-layer is uniform, which equals $c(0,s)$. Then $Q_C(s) = F \cdot A \cdot \delta \cdot c(0,s)$, which leads to

$$I_C(s) = s \cdot Q_C(s) = F \cdot A \cdot \delta \cdot s \cdot c(0,s). \tag{2.4}$$

The last equation needed for the derivation is the diffusion equation, which reads in the time domain:

$$\frac{\partial c}{\partial t} = d \frac{\partial^2 c}{\partial x^2}, \quad 0 < x < h_2 - h_1, \tag{2.5}$$

where $h_2 - h_1$ is the thickness of the polymer layer according to Fig. 2.3, which defines the dimensional parameters in this chapter. The generic solution of (2.5) in the frequency domain is obtained as [48]:

$$c(x,s) = \gamma_1(s) e^{-\sqrt{s/d}\, x} + \gamma_2(s) e^{\sqrt{s/d}\, x}, \tag{2.6}$$

where

$$\begin{cases} \gamma_1(s) = \dfrac{I_C(s)}{2F \cdot A \cdot \delta \cdot s} + \dfrac{I_D(s)}{2F \cdot A \cdot \sqrt{d \cdot s}} \\ \gamma_2(s) = \dfrac{I_C(s)}{2F \cdot A \cdot \delta \cdot s} - \dfrac{I_D(s)}{2F \cdot A \cdot \sqrt{d \cdot s}} \end{cases} . \tag{2.7}$$

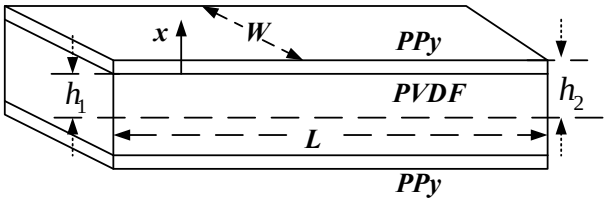

Figure 2.3: Definitions of dimensional parameters used in actuation model.

For the trilayer polypyrrole actuator, there is no ionic flux at the other surface of the polypyrrole layer, which gives the boundary condition at $x = h_2 - h_1$:

$$\frac{\partial c(x,s)}{\partial x}|_{x=h_2-h_1} = -\sqrt{\frac{s}{d}}\gamma_1(s)e^{-\sqrt{s/d}(h_2-h_1)} + \sqrt{\frac{s}{d}}\gamma_2(s)e^{\sqrt{s/d}(h_2-h_1)} = 0. \tag{2.8}$$

From (2.1) and (2.2), $I_C(s)$ and $I_D(s)$ can be written in terms of $V(s)$ and $I(s)$:

$$I_C(s) = s \cdot C \cdot (V(s) - I(s) \cdot R), \tag{2.9}$$

$$I_D(s) = I(s) - s \cdot C \cdot (V(s) - I(s) \cdot R). \tag{2.10}$$

Plugging (2.9) and (2.10) into (2.8), one gets the following equation in terms of $V(s)$ and $I(s)$

$$\begin{aligned} &[\ \frac{C}{2\delta}\frac{e^{\sqrt{s/d}\,(h_2-h_1)} - e^{-\sqrt{s/d}\,(h_2-h_1)}}{e^{\sqrt{s/d}\,(h_2-h_1)} + e^{-\sqrt{s/d}\,(h_2-h_1)}} + \frac{C}{2}\sqrt{\frac{s}{d}}\ ]V(s) = \\ &[\ \frac{R \cdot C}{2\delta}\frac{e^{\sqrt{s/d}\,(h_2-h_1)} - e^{-\sqrt{s/d}\,(h_2-h_1)}}{e^{\sqrt{s/d}\,(h_2-h_1)} + e^{-\sqrt{s/d}\,(h_2-h_1)}} + (\frac{1+s \cdot R \cdot C}{2d})\sqrt{\frac{d}{s}}\ ]I(s). \end{aligned} \tag{2.11}$$

Since

$$\frac{e^{\sqrt{s/d}\,(h_2-h_1)} - e^{-\sqrt{s/d}\,(h_2-h_1)}}{e^{\sqrt{s/d}\,(h_2-h_1)} + e^{-\sqrt{s/d}\,(h_2-h_1)}} = \tanh((h_2-h_1)\sqrt{\frac{s}{d}}),$$

the admittance model of a trilayer conjugated polymer can be derived from (2.11) as

$$\frac{I(s)}{V(s)} = \frac{s[\frac{\sqrt{d}}{\delta}\tanh((h_2-h_1)\sqrt{s/d}) + \sqrt{s}\,]}{\frac{\sqrt{s}}{C} + R\cdot s^{3/2} + R\cdot\frac{\sqrt{d}}{\delta}\cdot s\cdot\tanh((h_2-h_1)\sqrt{s/d})}. \tag{2.12}$$

It is highly desirable to have quantitative models available that can predict quasi-static and dynamic actuation performance in terms of intrinsic material parameters and actuator dimensions. Such models will be useful in feasibility analysis, design optimization, and even actuator control. A scalable electrochemomechanical model is presented for trilayer conjugated polymer actuators, by developing the scaling laws for key parameters of the electrical admittance model.

2.1.2 Scaling Laws for Double-layer Capacitance and Circuit Resistance

Two key parameters in the electrical admittance model (and thus in the force or displacement response model) are the double-layer capacitance C and the resistance R. It is of interest to know how they scale with the actuator dimensions. From the analogy to parallel-plate capacitors, one expects C to be proportional to the interface area between the PPy and the electrolyte, i.e.,

$$C = C_0 WL, \tag{2.13}$$

where C_0 is the double-layer capacitance per unit area.

The scaling of R is more involved. A transmission line model is proposed considering the nonzero (although low) resistivity of PPy, as shown in Fig. 2.4. Here the top and bottom layers represent PPy resistance while the middle layer represents the electrolyte resistance. Let ρ_1 and ρ_2 denote the resistivity of the PPy and that of the electrolyte, respectively. Then

the resistances R_1 and R_2 per unit distance are:

$$R_1 = \frac{\rho_1}{(h_2 - h_1)W},\ R_2 = \frac{2\rho_2 h_1}{W}.$$

From the basic transmission line theory [49],

$$R = \frac{\sqrt{\frac{4\rho_1\rho_2 h_1}{(h_2 - h_1)W^2}}}{\tanh(L\sqrt{\frac{4\rho_1\rho_2 h_1}{(h_2 - h_1)W^2}})}, \tag{2.14}$$

which is expressed in terms of fundamental material parameters and layer dimensions.

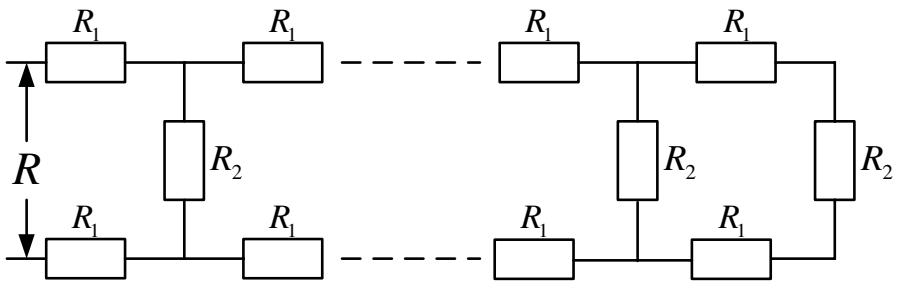

Figure 2.4: The transmission line model for the circuit resistance.

The scaling laws (2.13) and (2.14) can then be plugged into (2.12) to obtain scalable models for the admittance and the bending dynamics of trilayer actuators.

To measure the double-layer capacitance C, a step voltage U of 0.4 V is applied. The transferred charge Q into the PPy layer is computed by integrating the charging current, which is obtained by subtracting the faradaic current from the total current. It can be shown from (2.12) (using the Final Value Theorem [50]) that

$$Q = \frac{1}{2}U(1 + \frac{h_2 - h_1}{\delta})C, \tag{2.15}$$

and thus C is computed by

$$C = \frac{2Q}{U(1+\frac{h_2-h_1}{\delta})}. \tag{2.16}$$

The double-layer thickness δ is hard to measure directly and an estimate of 25 nm is used based on the range reported in [51]. To measure the resistance R, a high-frequency sinusoidal input $U\sin(\omega t)$ is applied. From (2.12), the admittance $Y(j\omega) \to \frac{1}{2R}$ as $\omega \to \infty$, i.e., the polymer becomes resistive for high-frequency inputs. Thus R is obtained from $R = \frac{1}{2|Y(j\omega)|}$. In experiments an input of frequency 250 Hz is used.

Fig. 2.5 shows the comparison between the measured double-layer capacitance and the predicted value from (2.13) for different actuator sizes (L $\times$ W), where C_0 is identified to be $7.86 \times 10^{-7}\,\mathrm{F/mm^2}$. Fig. 2.6 compares the measured resistance R and the predicted value from (2.14) as a function of actuator width, while the length of actuators is fixed to 20 mm. The resistivity values of $\rho_1 = 9 \times 10^{-5}\,\Omega$m and $\rho_2 = 2.7\,\Omega$m are obtained by fitting the experimental data points in Fig. 2.6, where ρ_1 is restricted within the typical range [52] during tuning. As an independent validation step, the identified ρ_1 and ρ_2 are further used to predict the resistance for five 3mm-wide actuators with different lengths. As shown in Fig. 2.7, the comparison between the measured resistances and their theoretical values based on (2.14) confirms the prediction capability of the scaling law.

The agreement between measurement and simulation in Figs. 2.5-2.7 validates the proposed laws for C and R, which will be used in the prediction of quasi-static force/displacement, electrical admittance, and dynamic displacement response in the following subsections.

2.2 Electromechanical Coupling

As introduced in Chapter 1, the fundamental actuation mechanism of the conjugated polymer actuator is the mass transport due to the ion movement during redox that further induces the strain changes in the polymer. Therefore, the early works have focused on the

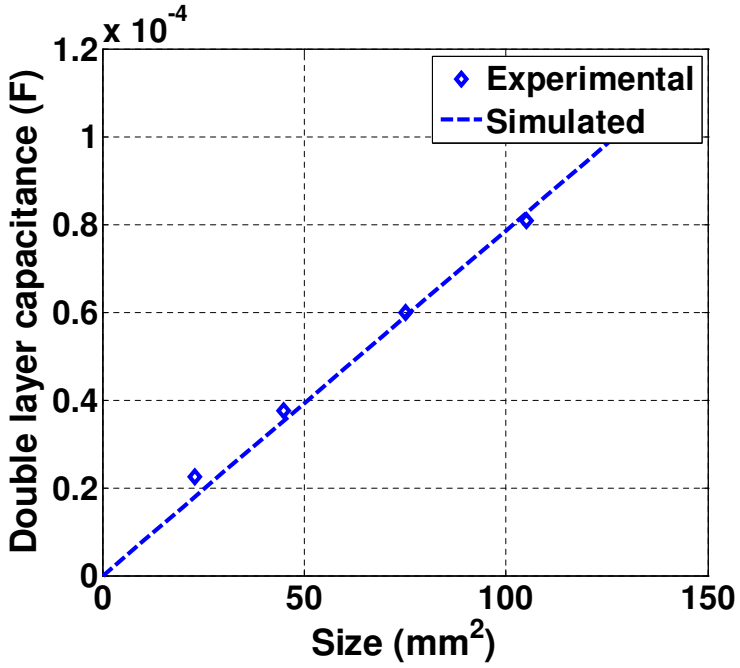

Figure 2.5: Double-layer capacitance versus actuator size.

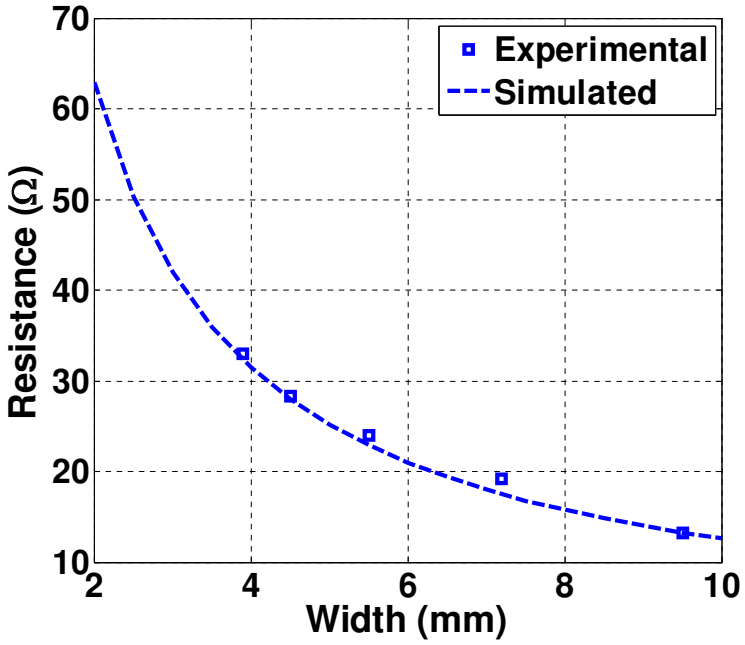

Figure 2.6: Resistance versus actuator width (length = 20 mm).

static electro-mechanical relationship between the charges transferred into the conjugated polymer and the corresponding strain generated. It was shown that the strain is propor-

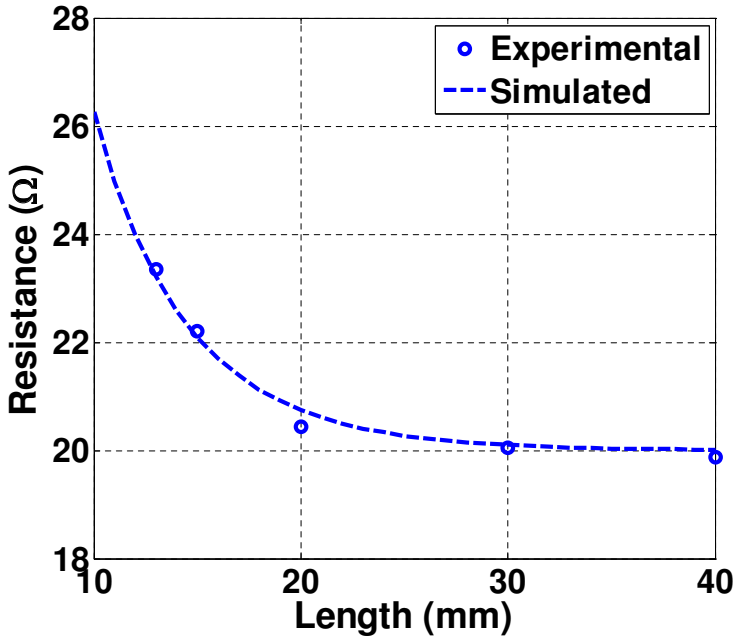

Figure 2.7: Resistance versus actuator length (width = 3 mm).

tional to the transferred charge density in the conjugated polymer [16, 53], which can be described as:

$$\varepsilon = \vartheta \rho, \tag{2.17}$$

where ϑ is the strain-to-charge ratio, ρ is the charge density. Equivalently, the induced stress by the transferred charges is

$$\sigma = \vartheta E_{ppy} \rho, \tag{2.18}$$

where E_{ppy} denotes the Young's modulus of the PPy layer.

2.3 Mechanical Output

When a voltage is applied across the actuator, the PPy layer on the anode side is oxidized while the other layer on the cathode side is reduced. The oxidized layer absorbs anions and expands, while the reduced layer gives up anions and contracts. The differential ex-

pansion thus leads to bending of the actuator, as shown in Fig. 1.3. The bending of the trilayer beam can be predicted based on the linear elasticity theory after the swelling ratios are determined for different layers. One key assumption for the linear model is that the relationship between the stress and strain is linear, given by the small strain Young's modulus, which is reasonable when the strain is sufficiently small. The elastic strain is obtained through the elementary beam theory by assuming that the strain changes linearly in the thickness direction with the distance from an appropriately located neutral line in the thickness direction [17]:

$$\varepsilon(x) = \kappa \cdot x, \tag{2.19}$$

where κ is the curvature to be determined.

When there is no external load, the beam curvature can be obtained by solving the force and moment balance equations simultaneously

$$\int_{-h_2}^{-h_1} \sigma_{PPy1}(x)dx + \int_{-h_1}^{h_1} \sigma_{PVDF}(x)dx + \int_{h_1}^{h_2} \sigma_{PPy2}(x)dx = 0, \tag{2.20}$$

$$\int_{-h_2}^{-h_1} \sigma_{PPy1}(x)xdx + \int_{-h_1}^{h_1} \sigma_{PVDF}(x)xdx + \int_{h_1}^{h_2} \sigma_{PPy2}(x)xdx = 0, \tag{2.21}$$

where h_1 and h_2 are as defined in Fig. 2.3. By superimposing the bending effect term upon the swelling term, the normal stresses in the PPy and PVDF layers along the beam direction are taken to be

$$\sigma_{PPy1}(x) = E_{PPy}\varepsilon(x) - E_{PPy}\vartheta\rho, \tag{2.22}$$

$$\sigma_{PVDF}(x) = E_{PVDF}\varepsilon(x), \tag{2.23}$$

$$\sigma_{PPy2}(x) = E_{PPy}\varepsilon(x) + E_{PPy}\vartheta\rho, \tag{2.24}$$

where E_{PPy} and E_{PVDF} are the small strain Young's moduli of the PPy and PVDF, and $PPy1$ and $PPy2$ represent the reduced and oxidized PPy layers, respectively. For a symmetrical

trilayer actuator, with the assumption that the thickness of the two PPy layers remains constant, it follows from (2.20) that the neutral line is the beam center line. Therefore, the actuation-induced curvature κ can be obtained as [17]:

$$\kappa = \frac{3\vartheta}{2h_1} \cdot \frac{(1+\frac{h_2-h_1}{h_1})^2 - 1}{(1+\frac{h_2-h_1}{h_1})^3 + \frac{E_{pvdf}}{E_{ppy}} - 1} \cdot \rho, \tag{2.25}$$

where E_{pvdf} is the Young's modulus of the PVDF layer, and h_{pvdf} denotes half of its thickness.

Note that the mechanical dynamics is not considered in the derivation, which means that the results only hold in the quasi-static condition. One needs to consider the mechanical dynamics of the trilayer beam at high frequencies. The actuation bandwidth of a PPy actuator is typically much lower than its natural frequencies. For example, a sample of dimensions $20 \times 5 \times 0.17$ mm was measured to have an actuation bandwidth of 0.5 Hz while its natural frequency was measured to be 65 Hz. Thus the inertial dynamics will be ignored. Therefore, only the material damping effect is considered. The standard linear solid model, illustrated in Fig. 2.8, can capture the viscoelasticity of solid polymer [54], and is adopted for modeling the dynamic moduli of PVDF and PPy. The equivalent modulus E' in Fig. 2.8 is

$$E'(s) = E\frac{\eta\chi + \chi}{\chi} \cdot \frac{s + \frac{1}{\eta\chi+\chi}}{s + \frac{1}{\chi}}. \tag{2.26}$$

Therefore one can furthermore modify (2.25) to be (2.27) to capture the higher frequency dynamics

$$\kappa = \frac{3\vartheta}{2h_1} \cdot \frac{(1+\frac{h_2-h_1}{h_1})^2 - 1}{(1+\frac{h_2-h_1}{h_1})^3 + \frac{E'_{pvdf}}{E'_{ppy}} - 1} \cdot \rho. \tag{2.27}$$

In experiments the beam tip displacement is measured by a laser distance sensor, as illustrated in Fig. 2.9. One can relate the measured displacement $y = d_0 - d$ to the curvature

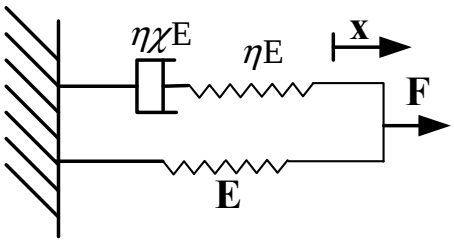

Figure 2.8: Standard linear solid model for capturing polymer viscoelasticity.

κ via simple geometric calculations:

$$\kappa = \frac{1}{r} = \frac{2y}{y^2 + l^2},$$

where l is the distance between the clamped end and the laser incident point when the beam is at rest. For small bending ($y << l$), the curvature is approximately linear with respect to the displacement:

$$\kappa \approx \frac{2y}{l^2}. \tag{2.28}$$

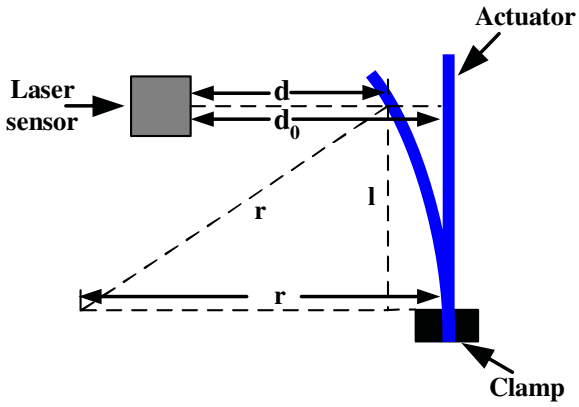

Figure 2.9: Geometric relationship between the beam curvature and the tip displacement.

2.4 Complete Actuation Model and Experimental Verification

2.4.1 Complete Actuation Model

One can obtain the complete scalable actuation model as follows by combining Eq. (2.12), (2.18), and (2.27):

$$\frac{\kappa}{V}=\frac{3\vartheta}{2LWh_1(h_2-h_1)}\cdot\frac{(\frac{h_2}{h_1})^2-1}{(\frac{h_2}{h_1})^3+\frac{E'_{pvdf}}{E'_{ppy}}-1}\cdot\frac{s^2[\frac{\sqrt{d}}{\delta}\tanh((h_2-h_1)\sqrt{\frac{s}{d}})+\sqrt{s}\,]}{\frac{\sqrt{s}}{C}+R\cdot s^{3/2}+R\cdot\frac{\sqrt{d}}{\delta}\cdot s\cdot\tanh((h_2-h_1)\sqrt{\frac{s}{d}})}, \tag{2.29}$$

where C and R follow the scaling laws in (2.13) and (2.14). Considering Eq. (2.28), one can obtain the actuation model with tip displacement as the output:

$$\frac{y}{V}=\frac{3\vartheta L}{Wh_1(h_2-h_1)}\cdot\frac{(\frac{h_2}{h_1})^2-1}{(\frac{h_2}{h_1})^3+\frac{E'_{pvdf}}{E'_{ppy}}-1}\cdot\frac{s^2[\frac{\sqrt{d}}{\delta}\tanh((h_2-h_1)\sqrt{\frac{s}{d}})+\sqrt{s}\,]}{\frac{\sqrt{s}}{C}+R\cdot s^{3/2}+R\cdot\frac{\sqrt{d}}{\delta}\cdot s\cdot\tanh((h_2-h_1)\sqrt{\frac{s}{d}})}. \tag{2.30}$$

Consider a trilayer actuator clamped at one end, as shown in Fig. 2.10. Under quasi-static conditions, it can be shown through moment balance (2.21) that the following equation holds to characterize the relationship between force and displacement:

$$F=-\gamma_1 y+\gamma_2\rho, \tag{2.31}$$

where γ_1 and γ_2 are defined by

$$\gamma_1=\frac{4WE_{ppy}h_{pvdf}^3}{3L_f^3}[(1+\frac{h}{h_{pvdf}})^3-1+\frac{E_{pvdf}}{E_{ppy}}],$$
$$\gamma_2=\frac{E_{ppy}\theta Wh_{pvdf}^2}{L_f}[(1+\frac{h}{h_{pvdf}})^2-1],$$

and E_{pvdf} denotes the Young's modulus of the PVDF layer.

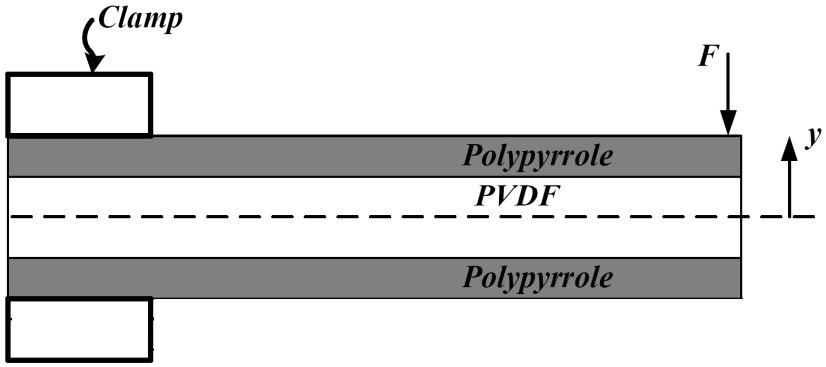

Figure 2.10: Geometry of the trilayer actuator.

2.4.2 Experimental Verification

Quasi-static force/displacement measurement is conducted using an experimental setup illustrated in Fig. 2.11. Through the slide, a PVDF micro-force sensor [55] can measure the actuation force at different deflection levels under a given actuation voltage, from the free-bending configuration $F = 0$ to the fully-blocked configuration ($y = 0$). A picture of the actual setup is shown in Fig. 2.12.

Two sets of PPy actuators are used with widths of 3.5 and 6 mm respectively. In each set there are three samples with lengths of 20, 30 and 40 mm. Given a constant voltage input, the current can be predicted by (2.12) and thus the charge density ρ. Therefore the force versus displacement curve can be computed using (2.31), where $E_{ppy} = 80$ MPa, $E_{pvdf} = 440$ MPa [14], $\vartheta = 1.3 \times 10^{-10}$ m$^3 \cdot$C^{-1} [16]. Fig. 2.13 shows the comparison between the measured force-displacement curve and the model prediction for the set of actuators with width 3.5 mm under an actuation voltage of 0.4 V. Fig. 2.14 shows the results for the set of actuators with width 6 mm. It can be seen that in both figures reasonable agreement between measurement and simulation is achieved. Experiments are also conducted for other actuation voltages with satisfactory agreement with model prediction. Those results

will not be presented here due to space limitation. One of the implications of the results in Figs. 2.13 and 2.14 is that the longer the actuator is, the smaller is the force output, and vice versa. This fact is in agreement with the results presented in [14].

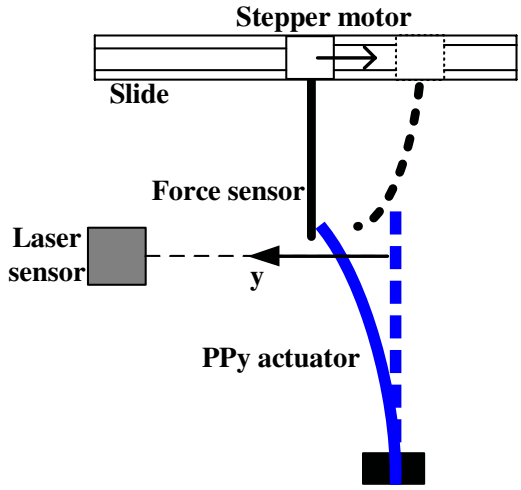

Figure 2.11: Schematic of the experimental setup for joint force-displacement measurement.

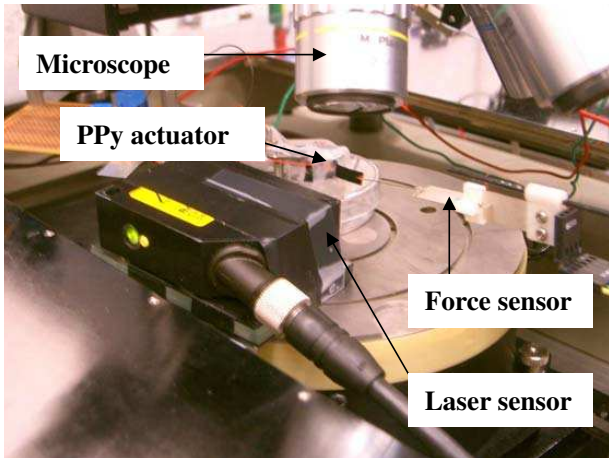

Figure 2.12: The setup for force/displacement measurement.

In Fig. 2.15, the measured admittance is compared to the predicted one for an actuator of size 30×5 mm, while in Fig. 2.16 the same is presented for an actuator of size 40×5 mm. In both figures the agreement in magnitude plots is excellent. In the mean time the match for the phase plots is good except for the relatively big discrepancy at the low-

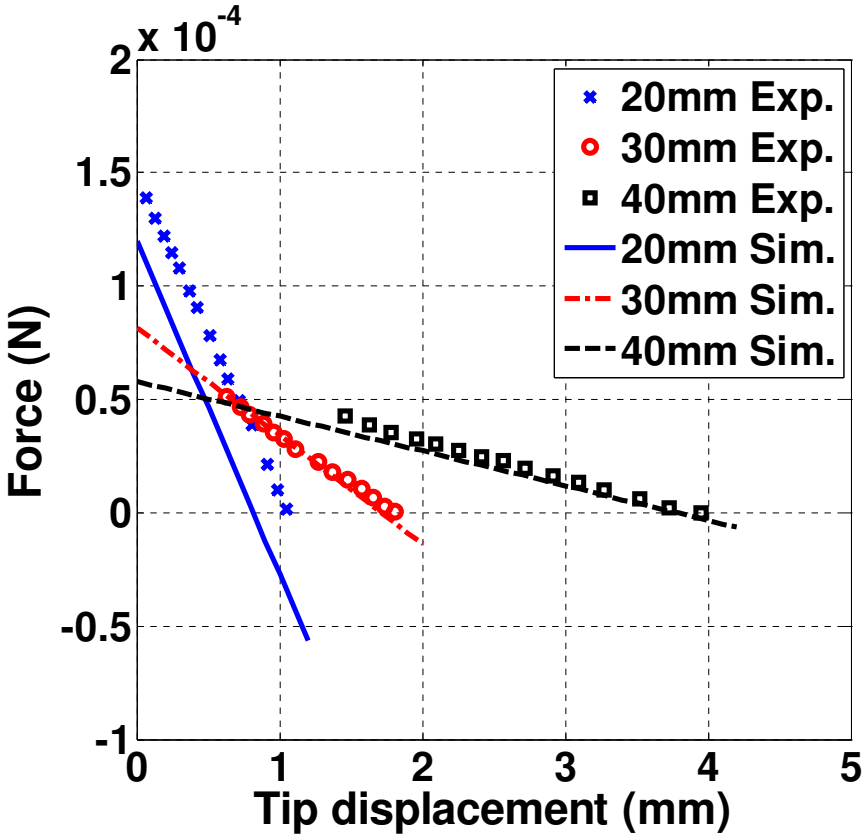

Figure 2.13: Force versus displacement under an actuation voltage of 0.4 V (width = 3.5 mm).

frequency end. The low-frequency phase mismatch is likely due to the change of actuation behavior in air when the solvent evaporates over time (the high-frequency measurements are done in a short period of time and the behavior change there is minimal).

The model (2.30) for the dynamic displacement response is verified for a range of actuation frequencies for two different actuator sizes, 30×5 mm and 40×5 mm. The comparison between the experimental measurement and the model prediction is shown in Fig. 2.17 and Fig. 2.18. The coefficients related to dynamic modulus in (2.26) for PPy and PVDF are identified based on curve fitting: $\eta = 5.02$ and $\chi = 0.83$ for PPy, and $\eta = 4.68$ and $\chi = 0.044$ for PVDF. From the figures the agreement between measurement and simulation is good for the magnitude plots. However, mismatch exists in the low-frequency portion of the phase plots. The cause of this, other than the possible behavior change due

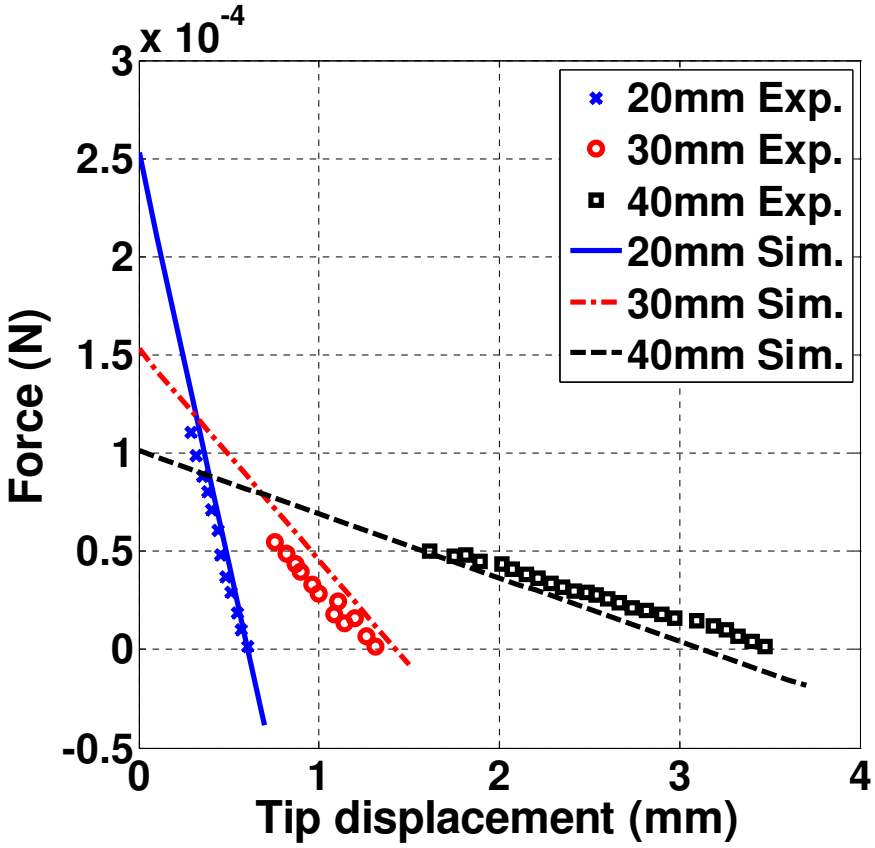

Figure 2.14: Force versus displacement under an actuation voltage of 0.4 V (width = 6 mm).

to solvent evaporation, requires further investigation.

2.5 Conjugated Polymer Electromechanical Sensor

Research on the possibility to use conjugate polymers as electromechanical sensors has been relatively limited, comparing with the extensive work on modeling of conjugate polymer actuators [6, 16–19]. Wu *et al.* [20] investigated the sensing behavior of a trilayer PPy beam by considering the perturbation of the Donnan equilibrium of the ion distribution by mechanical stimuli as the primary sensing mechanism. A similar viewpoint was also presented by Takashima and coworkers [21]. For better understanding of the sensing mechanisms, however, more experiments and quantitative modeling of the sensing dynam-

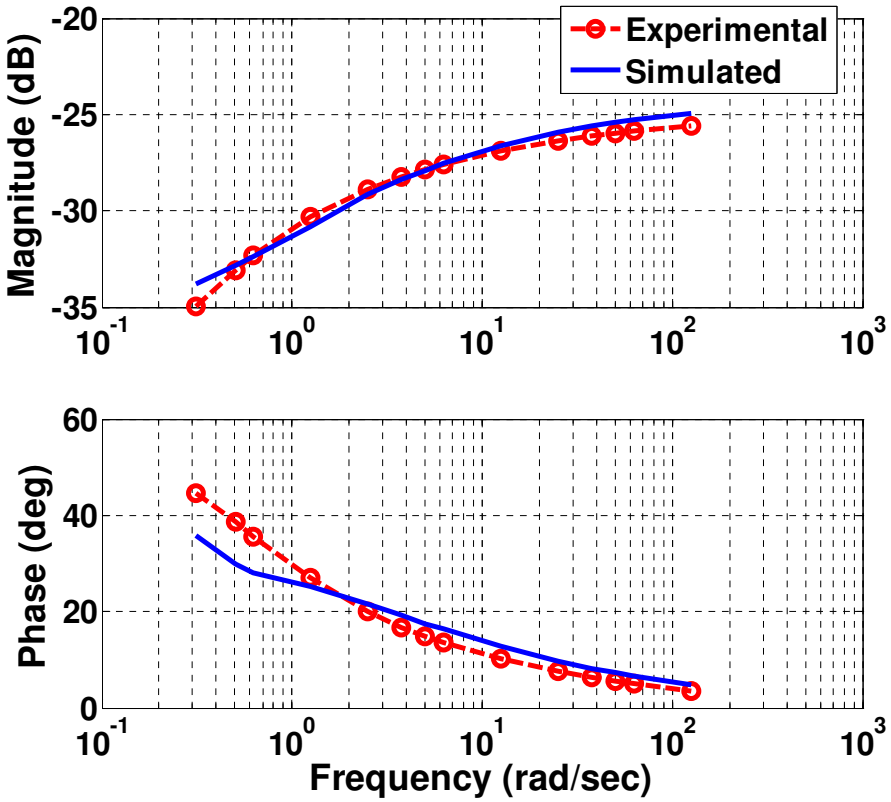

Figure 2.15: Electrical admittance spectrum (size: 30×5 mm).

ics are desired.

A preliminary model is proposed to explain the sensing mechanism, which starts with a partial differential equation (PDE) that governs the ion redistribution dynamics subject to diffusion and migration (due to electrostatic interactions). Two boundary conditions are postulated: 1) the ion concentration at the PPy/PVDF interface is proportional to the applied mechanical strain, as the latter directly influences the pore sizes of the PPy layer; and 2) there is no diffusion flux at the interface between the PPy layer and the air. This PDE can be solved numerically. However, for real-time sensing applications, it is desirable to have an analytical model. For this purpose, we ignore the migration term of the PDE, which makes the equation linear. The latter can be solved analytically in the Laplace domain, which leads to a transfer function that relates the open-circuit sensing voltage to the applied mechanical deformation. The obtained solution shows good approximation to the

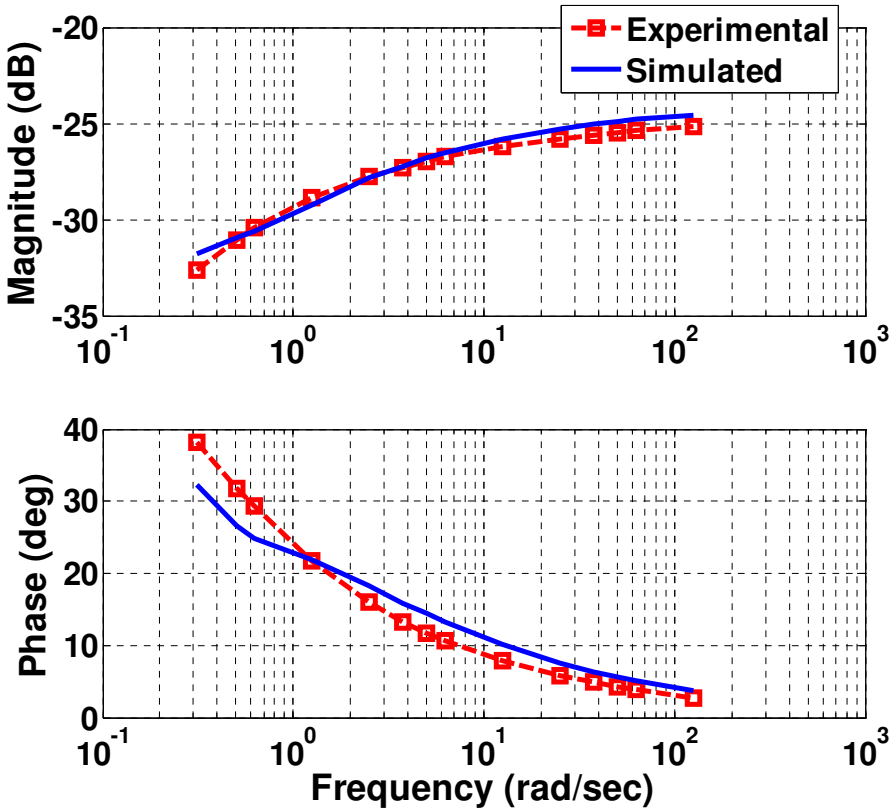

Figure 2.16: Electrical admittance spectrum (size: 40×5 mm).

solution of the original PDE when the ion concentration is relatively low and matches the experimental data for conjugated polymer sensors with different lengths and widths. However, some recent experimental results by using conjugated polymer with different PPy thickness show discrepancy from the model prediction, which implies the model has not captured all the sensing phenomenon.

2.5.1 Full Sensing Model

The Nernst-Planck equation is used widely to describe the flux of ions under the influence of both an ionic concentration gradient and an electric field [56]:

$$\mathbf{J} = -d(\nabla C + \frac{CF}{RT}\nabla\phi). \tag{2.32}$$

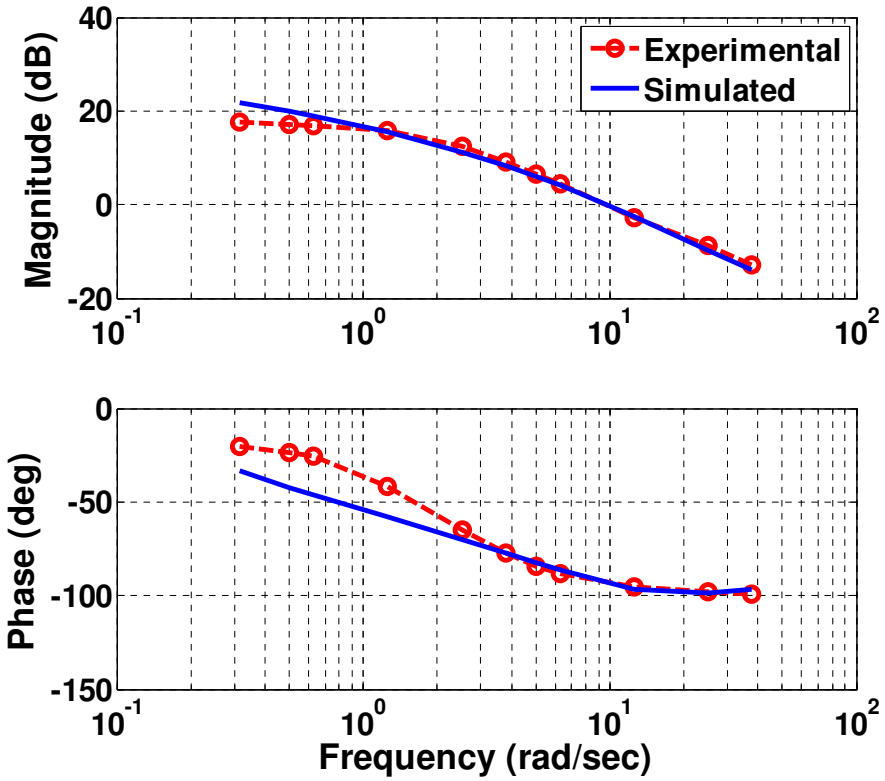

Figure 2.17: Dynamic displacement response (size: 30×5 mm).

The continuity equation holds:

$$\nabla \cdot \mathbf{J} = -\frac{\partial C}{\partial t}. \tag{2.33}$$

Since the thickness of the PPy layer is much smaller than its length or width, one can assume that dominant changes are all restricted to the thickness direction (denoted as x direction). This enables one to drop the boldface notation for these variables. From (2.33), we can derive

$$\frac{\partial C}{\partial t} = d\left(\frac{\partial^2 C}{\partial x^2} + \frac{F}{RT}\frac{\partial C}{\partial x}\frac{\partial \phi}{\partial x} + \frac{FC}{RT}\frac{\partial^2 \phi}{\partial x^2}\right). \tag{2.34}$$

One can relate ϕ to the ionic concentrations through the Gauss's law:

$$\mathbf{E} = \frac{D}{\kappa_e} = -\nabla\phi \tag{2.35}$$

$$\nabla \cdot \mathbf{D} = F \cdot (C^+ - C^-), \tag{2.36}$$

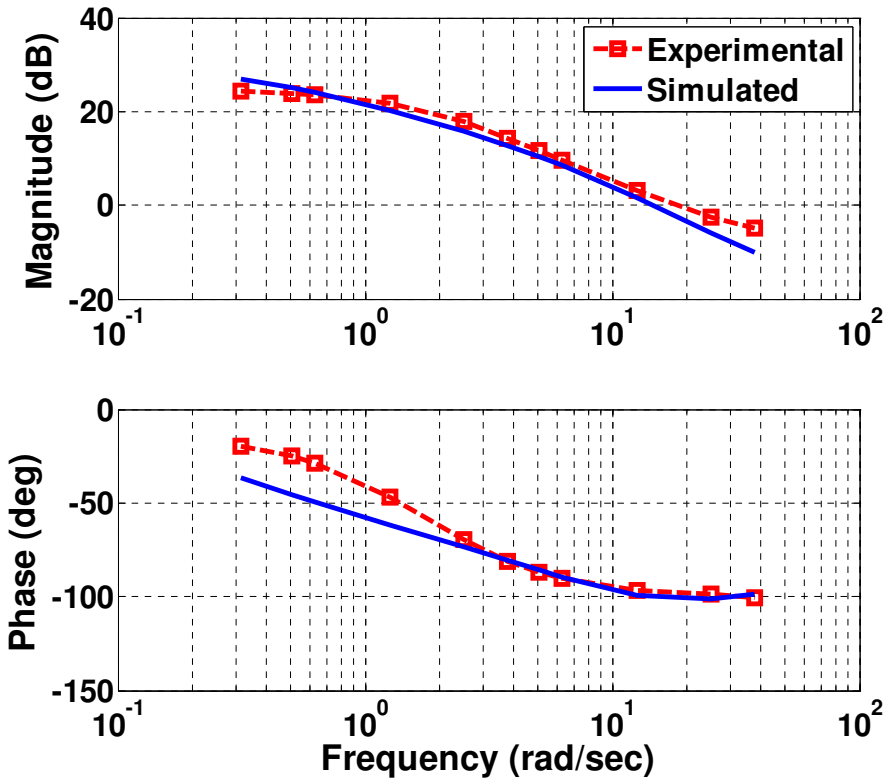

Figure 2.18: Dynamic displacement response (size: 40×5 mm).

where **D** denotes the electric displacement, **E** denotes the electric field, and κ_e is the dielectric permittivity of PPy. Therefore, the following equations can be derived based on (2.35) and (2.36):

$$\frac{\partial \phi}{\partial x} = \frac{F}{\kappa_e}\int_0^x C(\xi,t)d\xi + \frac{\partial \phi}{\partial x}(0,t), \tag{2.37}$$

$$\frac{\partial^2 \phi}{\partial x^2} = \frac{F}{\kappa_e}C(x,t). \tag{2.38}$$

In mechanical sensing, one can assume that $C(x,t)$ fluctuates about some equilibrium concentration C_0:

$$C(x,t) = C_0 + C_1(x,t), \tag{2.39}$$

with $C_0 \gg C_1(x,t)$. Further assume that the electrolyte has high ionic conductivity, which implies $\frac{\partial \phi}{\partial x}(0,t) = 0$ in (2.37). Therefore, (2.37) can be approximated by

$$\frac{\partial \phi}{\partial x} \approx \frac{FC_0}{\kappa_e} x. \tag{2.40}$$

Combining (2.34), (2.38), (2.39) and (2.40), and ignoring the C_1^2 term, one obtains

$$\frac{\partial C_1}{\partial t} = d\left(\frac{\partial^2 C_1}{\partial x^2} + \frac{F^2}{RT\kappa_e}\frac{\partial C_1}{\partial x} C_0 x + \frac{F^2}{RT\kappa_e}(C_0^2 + 2C_0 C_1)\right). \tag{2.41}$$

Two boundary conditions are imposed on (2.41):

$$C_1(0,t) = KC_0\varepsilon_0(t), \tag{2.42}$$

$$\frac{\partial C_1}{\partial x}|_{x=h_2-h_1} = 0, \tag{2.43}$$

where $\varepsilon_0(t)$ represents the strain at the PPy/PVDF interface. Note that $x = 0$ denotes the PPy/PVDF boundary while $x = h_2 - h_1$ denotes the PPy/air interface. The first boundary condition implies that the concentration perturbation at $x = 0$ has a linear correlation with the applied deformation. The second one means that there is no diffusion flux on the other side of the PPy layer.

2.5.2 Simplified Sensing Model

Eq. (2.41) is difficult to solve analytically. However, it is desirable to obtain an analytical model for conjugated polymer sensors. Such a model can facilitate fundamental understanding of the sensing mechanisms and be instrumental in sensor design and real-time sensing applications. An analytical model from (2.41) can be obtained by further ignoring the terms involving C_0. Equivalently, this is to ignore the effect of electric field-induced ion migration. The approximation is valid when the nominal anion concentration C_0 is low.

The approximated PDE contains only the diffusion term:

$$\frac{\partial C_1}{\partial t} = d\frac{\partial^2 C_1}{\partial x^2}. \tag{2.44}$$

To solve this PDE, (2.44) is firstly converted into the Laplace domain

$$\frac{\partial^2 C_1(x,s)}{\partial x^2} = \frac{sC_1(x,s)}{d}. \tag{2.45}$$

One can obtain the following analytical solution to (2.45):

$$C_1(x,s) = \frac{KC_0\varepsilon_0 e^{\sqrt{\frac{s}{d}}(h_2-h_1)}}{e^{\sqrt{\frac{s}{d}}(h_2-h_1)}+e^{-\sqrt{\frac{s}{d}}(h_2-h_1)}}e^{-\sqrt{\frac{s}{d}}x} + \frac{KC_0\varepsilon_0 e^{-\sqrt{\frac{s}{d}}(h_2-h_1)}}{e^{\sqrt{\frac{s}{d}}(h_2-h_1)}+e^{-\sqrt{\frac{s}{d}}(h_2-h_1)}}e^{\sqrt{\frac{s}{d}}x}. \tag{2.46}$$

Furthermore one can obtain the potential difference across one PPy layer based on (2.35) and (2.36):

$$\begin{aligned}
\Delta V_1 &= \phi(h,s) - \phi(0,s) \\
&= \frac{dFKC_0\varepsilon_0}{s\kappa_e}\left[\frac{2}{e^{\sqrt{\frac{s}{d}}(h_2-h_1)}+e^{-\sqrt{\frac{s}{d}}(h_2-h_1)}} + (h_2-h_1)\sqrt{\frac{s}{d}}\tanh((h_2-h_1)\sqrt{\frac{s}{d}}) - 1\right] \\
&\quad + \frac{FC_0}{2\kappa_e}(h_2-h_1)^2.
\end{aligned} \tag{2.47}$$

Due to the symmetry of the trilayer structure, the potential across the other PPy layer is

$$\begin{aligned}
\Delta V_2 &= -\frac{dFKC_0\varepsilon_0}{s\kappa_e}\left[\frac{2}{e^{\sqrt{\frac{s}{d}}(h_2-h_1)}+e^{-\sqrt{\frac{s}{d}}(h_2-h_1)}} + (h_2-h_1)\sqrt{\frac{s}{d}}\tanh((h_2-h_1)\sqrt{\frac{s}{d}}) - 1\right] \\
&\quad + \frac{FC_0}{2\kappa_e}(h_2-h_1)^2.
\end{aligned} \tag{2.48}$$

Therefore, an analytical model for the total open-circuit sensing voltage is:

$$\begin{aligned} V &= \Delta V_1 - \Delta V_2 \\ &= \frac{2dFKC_0\varepsilon_0}{s\kappa_e}\left[\frac{2}{e^{\sqrt{\frac{s}{d}}(h_2-h_1)}+e^{-\sqrt{\frac{s}{d}}(h_2-h_1)}}+(h_2-h_1)\sqrt{\frac{s}{d}}\tanh((h_2-h_1)\sqrt{\frac{s}{d}})-1\right]. \end{aligned} \tag{2.49}$$

From (2.49), one can obtain the transfer function relating the sensing voltage $V(s)$ to the applied deformation $\varepsilon_0(s)$ (strain at the PPy/PVDF interface):

$$\frac{V(s)}{\varepsilon_0(s)} = \frac{2dFKC_0}{s\kappa_e}\left[\frac{2}{e^{\sqrt{\frac{s}{d}}(h_2-h_1)}+e^{-\sqrt{\frac{s}{d}}(h_2-h_1)}}+(h_2-h_1)\sqrt{\frac{s}{d}}\tanh((h_2-h_1)\sqrt{\frac{s}{d}})-1\right]. \tag{2.50}$$

The following equation holds for the strain and the curvature

$$\varepsilon(x) = \kappa \cdot x. \tag{2.51}$$

The strain ε_0 at the boundary of PPy layer and PVDF layer can be further related to the tip displacement:

$$\varepsilon_0 = \frac{2h_1}{l^2}y. \tag{2.52}$$

Now taking the applied tip displacement y as the input, from (2.50), one can obtain the transfer function for the sensing dynamics:

$$\frac{V(s)}{Y(s)} = \frac{4dFKC_0h_1}{sl^2\kappa_e}\left[\frac{2}{e^{\sqrt{\frac{s}{d}}(h_2-h_1)}+e^{-\sqrt{\frac{s}{d}}(h_2-h_1)}}+(h_2-h_1)\sqrt{\frac{s}{d}}\tanh((h_2-h_1)\sqrt{\frac{s}{d}})-1\right]. \tag{2.53}$$

We have compared the numerical solution of the full model with the analytical model derived above. In the computation, C_0 was taken to be 0.05 M. A sequence of sinusoidal inputs $\varepsilon_0(t)$, up to 100 Hz, was used. For each input, the numerical solution of $V(t)$ was computed, and the gain and phase shift at that frequency were evaluated. Fig. 2.19 com-

pares the Bode plots obtained through numerical computation with those of the analytical model (2.50). As one can see, overall the discrepancy is not significant; in particular, as the frequency gets high, the discrepancy vanishes.

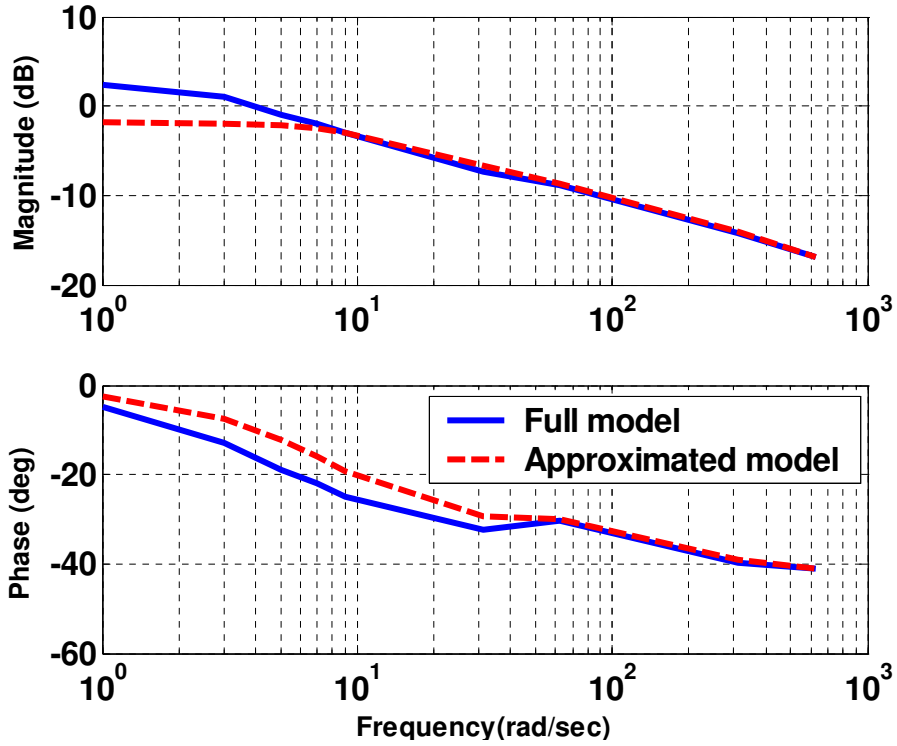

Figure 2.19: Comparison between the numerical solution of the full model and the analytical solution of the simplified model (2.50) when C_0 is 0.05 M.

2.5.3 Experiments and Discussions

Fig. 2.20 and Fig. 2.21 show the experimental characterization of the dynamic sensing behavior of the conjugated polymer samples. Predictions from the model (2.53) are also shown in the figures for comparison purposes. The parameters used for the model are listed in Table 2.1. It can be seen that the predictions from the analytical model in general fit the experimental data. In particular, the magnitude plots show good fitting with the experimental data and predict the decaying trend as the frequency becomes higher. Although there is

some discrepancy in the phase plots, the general trend of the experimental data is predicted by the model.

The model (2.53) predicts that the sensing voltage is independent of the sample width. This is supported by the experimental data in Fig. 2.20, where one can see that the sensing behaviors of three samples, with different widths, are close to each other. The model also predicts that the sample length will influence the magnitude but not the phase of the transfer function, which is again verified by the experiments (Fig. 2.21).

Table 2.1: Parameter values used for the model (2.53).

Parameter	Value
F	9.65×10^4 C/mol
K	0.072
h_2	85 μm
h_1	55 μm
d	1×10^{-8} m^2/s
κ_e	5.31×10^{-10} C^{2}N^{-1}m^{-2}
C_0	0.1 M

2.6 Chapter Summary

A full electrochemomechanical model is presented for trilayer PPy actuators. The scaling laws for two important parameters, the double-layer capacitance and the resistance, are proposed and experimentally verified. The model can thus be written in terms of fundamental material parameters and actuator dimensions. Through experiments with actuators of different dimensions (length and width), the following aspects of the scalability of the model are independently validated: quasi-static force/displacement output, electrical admittance, and dynamic displacement response. The model will be instrumental in feasibility analysis for new applications of conjugated polymer actuators and in optimization of actuator fabrication and design.

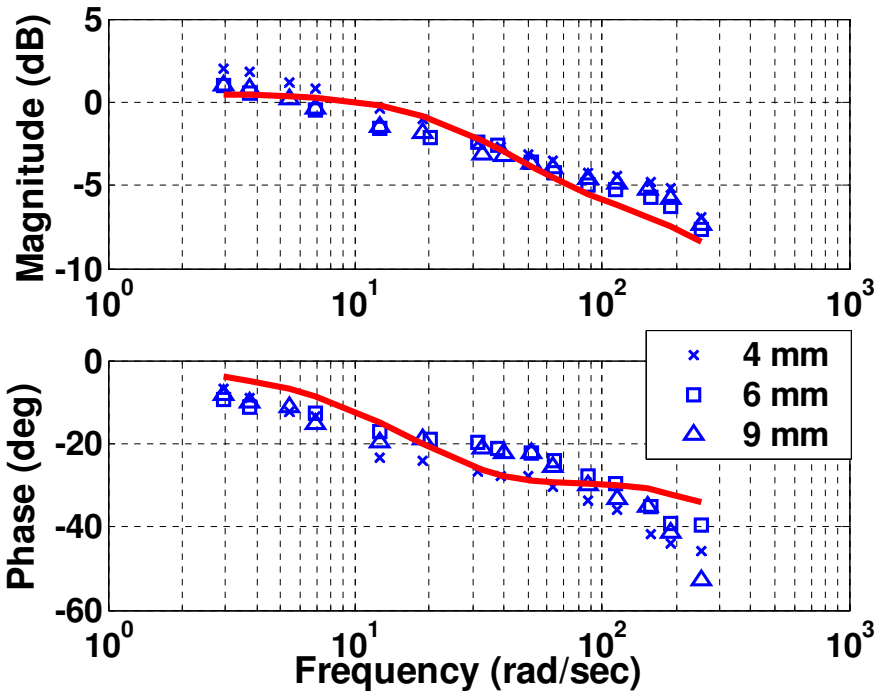

Figure 2.20: Dynamic response of conjugated polymer sensors: Experimental measurement (marks) versus model prediction (line). Three samples with different widths (fixed length: 30 mm).

Besides investigating sensing properties, we also proposed a model to explain the sensing mechanism of conjugated polymers sensor. The model accounts for the ion transport dynamics within the polymer, including both ion diffusion and electric field-induced migration. A key assumption of the model is that the applied deformation prescribes the ion concentration at the polymer/electrolyte interface. The model was further simplified by dropping the migration term. In that case, an analytical solution was obtained in the Laplace domain, leading to an (infinite-dimensional) transfer function model for the sensing dynamics. Experimental results were also reported to support the modeling effort.

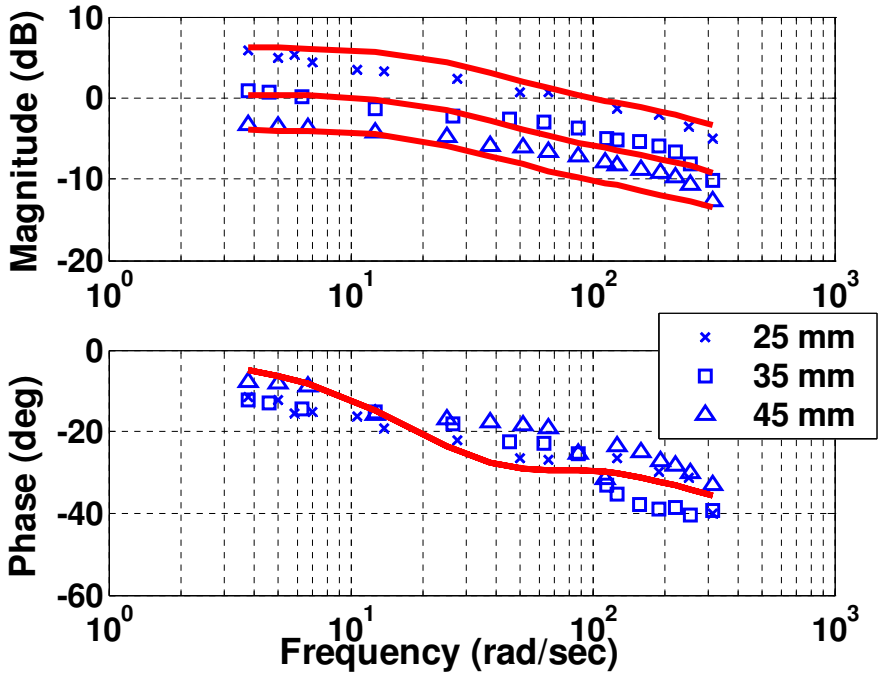

Figure 2.21: Dynamic response of conjugated polymer sensors: Experimental measurement (marks) versus model prediction (line). Three samples with different lengths (fixed width: 5 mm).

Chapter 3

Modeling Nonlinearities in Conjugated Polymer Actuators

3.1 Redox Level-dependent Impedance Model

It is known that the redox level of conjugated polymer has significant impact on its material properties [22, 23, 57], which will further influence the actuation performances [34]. However, understanding and modeling the influence of redox level are inadequate in the previous work. Therefore the ions transport phenomenon is modeled as follows by a redox level-dependent impedance model, which is developed by including both ionic diffusion and migration effects and by using perturbation analysis. Experiments are conducted under various redox conditions to verify the proposed model.

3.1.1 The Governing Partial Differential Equation

The anion flux **J** inside the polymer is captured by the Nernst-Planck equation [56], including both a diffusion term and an electric field-induced migration term:

$$\mathbf{J} = -d(\nabla C^{-} + \frac{C^{-}F}{RT}\nabla\phi), \tag{3.1}$$

where d is the ionic diffusion coefficient, F is the Faraday's constant, R is the gas constant, T is the absolute temperature, ϕ is the electric potential, and ∇ denotes the gradient. The continuity equation gives

$$\begin{aligned} \frac{\partial C^-}{\partial t} &= -\nabla \cdot \mathbf{J}, \\ &= d\left(\nabla \cdot \nabla C^- + \nabla \cdot \left(\frac{C^- F}{RT} \nabla \phi\right)\right), \end{aligned} \tag{3.2}$$

where $\nabla\cdot$ denotes the divergence.

Since the thickness of the PPy layer is much smaller than its length or width, one can assume that, inside the polymer, $\mathbf{J}$, $\mathbf{D}$, $\mathbf{E}$, and other changes are all restricted to the thickness direction (denoted as x direction). This enables one to drop the boldface notation for these variables; in particular, D and E will be used to represent the electric displacement and the electric field (along the x direction). Furthermore, (3.2) can be simplified as

$$\frac{\partial C^-}{\partial t} = d\left(\frac{\partial^2 C^-}{\partial x^2} + \frac{F}{RT}\frac{\partial C^-}{\partial x}\frac{\partial \phi}{\partial x} + \frac{C^- F}{RT}\frac{\partial^2 \phi}{\partial x^2}\right). \tag{3.3}$$

A pure delay is adopted to capture the oxidation dynamics, i.e.,

$$C^+(x,t) = C^-(x, t - T_0), \tag{3.4}$$

where T_0 is the time taken for an anion A^- to react with PPy. Finally, there are two boundary conditions for (3.3): 1) C^- at $x = 0$ equals the concentration in the PPy/PVDF double layer; 2) The ionic flux $J(x,t)$ at $x = h_2 - h_1$ (the other boundary of PPy layer) vanishes, assuming no ions leaking outside.

Equations (2.35), (2.36), (3.3), (3.4), and the boundary conditions form a complete description of the ionic dynamics inside PPy.

3.1.2 Perturbation Analysis

From (2.35) and (2.36), one can express $\frac{\partial \phi}{\partial x}$ and $\frac{\partial^2 \phi}{\partial x^2}$ as

$$\begin{aligned} \frac{\partial \phi}{\partial x} &= -\frac{F}{\kappa_e}\int_0^x (C^+ - C^-)d\xi + \frac{\partial \phi}{\partial x}(0,t) && (3.5) \\ \frac{\partial^2 \phi}{\partial x^2} &= -\frac{F}{\kappa_e}(C^+ - C^-). && (3.6) \end{aligned}$$

Supposing that the double layer charging process is relatively fast comparing to the ionic dynamics in PPy (which is usually the case), the net charge inside the double layer is zero. Further assume that the electrolyte in PVDF has good ionic conductivity, and thus the electric field within is negligible. Under these assumptions, one can apply Gauss's law to a small volume containing the double layer and conclude $\frac{\partial \phi}{\partial x}(0,t) = 0$ in (3.5). Plugging (3.5), (3.6), and (3.4) into (3.3), one obtains

$$\begin{aligned} \frac{\partial C^-}{\partial t} &= d\Big(\frac{\partial^2 C^-}{\partial x^2} - \frac{F^2}{RT\kappa_e}C^-(C^-(x,t-T_0) - C^-(x,t)) \\ &\quad -\frac{F^2}{RT\kappa_e}\frac{\partial C^-}{\partial x}\int_0^x (C^-(\xi,t-T_0) - C^-(\xi,t))d\xi\Big). \qquad (3.7) \end{aligned}$$

Eq. (3.7) is a nonlinear integro-differential equation that cannot be solved analytically. We introduce perturbation analysis to linearize it around a nominal concentration C_0, which represents the redox level of the conjugated polymer. To proceed, let

$$C^-(x,t) = C_0 + \varepsilon C_1^-(x,t), \qquad (3.8)$$

with $0 < \varepsilon << 1$. In (3.8), $\varepsilon C_1^-(x,t)$ represents the small perturbation imposed on C_0. Plugging (3.8) into (3.7) and neglecting terms involving ε^2, one gets the following linearized equation that depends on the redox level C_0:

$$\frac{\partial C_1^-}{\partial t} = d\left(\frac{\partial^2 C_1^-}{\partial x^2} - \frac{F^2}{RT\kappa_e}C_0(C_1^-(x,t-T_0) - C_1^-(x,t))\right). \qquad (3.9)$$

To obtain an analytical solution, one can convert (3.9) from the time domain to the Laplace domain:

$$sC_1^- = d\left(\frac{\partial^2 C_1^-}{\partial x^2} + \frac{F^2 C_0^-}{RT\kappa_e}\cdot(1-e^{-sT_0})C_1^-\right), \tag{3.10}$$

where s is the Laplace variable.

Eq. (3.10) can be further written as

$$\frac{\partial^2 C_1^-}{\partial x^2} = \frac{s - K_1 C_0(1-e^{-sT_0})}{d} C_1^-, \tag{3.11}$$

with the constant

$$K_1 \triangleq \frac{dF^2}{RT\kappa_e}.$$

The solution of (3.11) has a generic form

$$C_1^-(x,s) = \alpha_1(s)e^{\beta(s)x} + \alpha_2(s)e^{-\beta(s)x}, \tag{3.12}$$

with

$$\beta(s) = \sqrt{\frac{s - K_1 C_0(1-e^{-sT_0})}{d}}. \tag{3.13}$$

The functions $\alpha_1(s)$ and $\alpha_2(s)$ are determined by the boundary conditions. The boundary condition at the PPy/PVDF interface, $x = 0$, is

$$C_1^-(0,s) = C_{dl}(s), \tag{3.14}$$

where $C_{dl}(s)$ denotes the ionic concentration in the double layer. Combining (3.12) and (3.14) gives

$$\alpha_1(s) + \alpha_2(s) = C_{dl}(s). \tag{3.15}$$

The other boundary condition, at $x = h_2 - h_1$, requires that the ionic flux be zero. Using (3.1), (3.5), and (3.8), and ignoring terms involving ε^2, the zero flux condition at $x = h_2 - h_1$

reads

$$\frac{\partial C_1^-}{\partial x}(h_2-h_1,s)+\frac{C_0F^2}{RT\kappa_e}(1-e^{-sT_0})\int_0^{h_2-h_1}C_1^-(\xi,s)d\xi=0. \tag{3.16}$$

Plugging (3.12) into (3.16), one gets

$$s(\alpha_1(s)e^{\beta(s)(h_2-h_1)}-\alpha_2(s)e^{-\beta(s)(h_2-h_1)})=(s-d\beta^2(s))(\alpha_1(s)-\alpha_2(s)). \tag{3.17}$$

Combining (3.15) and (3.17), one can solve for α_1 and α_2:

$$\alpha_1(s) = \frac{se^{-\beta(s)(h_2-h_1)}-(s-d\beta^2(s))}{\Delta(s)}C_{dl}(s), \tag{3.18}$$

$$\alpha_2(s) = \frac{se^{\beta(s)(h_2-h_1)}-(s-d\beta^2(s))}{\Delta(s)}C_{dl}(s). \tag{3.19}$$

with $\Delta(s)$ defined as

$$\Delta(s)=s\left(e^{\beta(s)(h_2-h_1)}+e^{-\beta(s)(h_2-h_1)}\right)-2(s-d\beta^2(s)). \tag{3.20}$$

3.1.3 Impedance Model

Fig. 3.1 shows the equivalent circuit for the proposed impedance model. The total current I consists of three components, the double layer charging current I_C, the diffusion current I_D, and the migration current I_M. In the figure C denotes the double layer capacitance, R_1 is the ohmic resistance of the oxidized PPy layer, and R_2 denotes the resistance of the reduced PPy layer, the PVDF (electrolyte) layer, and the contacts. Z_D and Z_M represent the diffusion dynamics and the migration dynamics, respectively. Each of the current components is discussed next. We will be concerned with the voltage/current associated with the charge concentration perturbation εC_1^-.

Double layer charging current I_C. Double-layer charges are established at the PPy/PVDF interface in response to an applied voltage, which can be captured equivalently through a

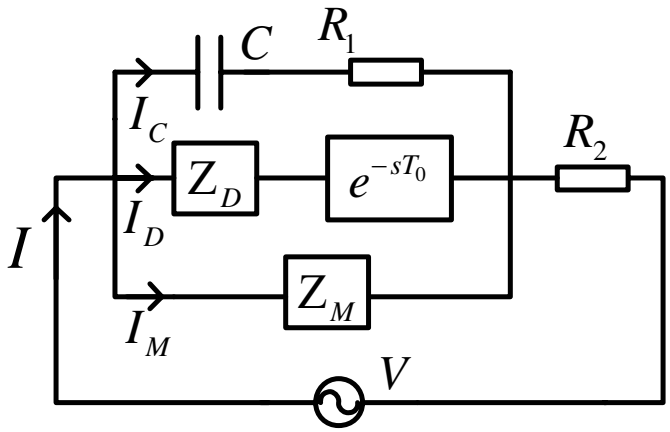

Figure 3.1: Equivalent circuit for the impedance model.

double layer capacitance C. The total stored charge in the double layer is $\varepsilon FA\delta C_{dl}(s)$, where A and δ denote the area of PPy layer and the thickness of the double layer, respectively. The time derivative of the stored charge gives I_C:

$$I_C(s) = \varepsilon FA\delta s C_{dl}(s). \tag{3.21}$$

Diffusion current I_D. The diffusion flux at the PPy/PVDF interface (i.e., $x = 0$) is given by the Fick's law and equals $-d\varepsilon\frac{\partial C_1^-}{\partial x}(0,s)$. But an electron is not released until the oxidation takes place after T_0 delay. I_D is thus expressed as

$$\begin{aligned} I_D(s) &= -\varepsilon FAde^{-sT_0}\frac{\partial C_1^-}{\partial x}(0,s) \\ &= -\varepsilon FAde^{-sT_0}\beta(s)(\alpha_1(s)-\alpha_2(s)) \qquad (3.22) \\ &= \frac{\varepsilon FAdse^{-sT_0}\beta(s)(e^{\beta(s)(h_2-h_1)}-e^{-\beta(s)(h_2-h_1)})}{\Delta(s)}C_{dl}(s), \qquad (3.23) \end{aligned}$$

where the second equality follows from (3.12).

Migration current I_M. I_M is induced by the net charges Q_P inside the PPy layer. Applying the integral form of Gauss's law to the PPy layer and recalling $E(0,s) = 0$, one can

obtain

$$\begin{aligned} Q_P(s) &= AD(h_2-h_1,s) = A\kappa_e E(h_2-h_1,s) = -A\kappa_e \frac{\partial \phi}{\partial x}(h_2-h_1,s) \\ &= -\varepsilon FA(1-e^{-sT_0})\int_0^{h_2-h_1} C_1^-(\xi,s)d\xi \qquad (3.24) \\ &= -\varepsilon FA(1-e^{-sT_0})\frac{\alpha_1 e^{\beta(h_2-h_1)} - \alpha_2 e^{-\beta(h_2-h_1)} - (\alpha_1-\alpha_2)}{\beta}, \qquad (3.25) \end{aligned}$$

where (3.24) follows from (3.5) and (3.25) follows from (3.12). I_M is then expressed as

$$\begin{aligned} I_M(s) &= sQ_P(s) \\ &= -\varepsilon FAs(1-e^{-sT_0})\frac{\alpha_1 e^{\beta(h_2-h_1)} - \alpha_2 e^{-\beta(h_2-h_1)} - (\alpha_1-\alpha_2)}{\beta} \\ &= -\frac{\varepsilon FAds(1-e^{-sT_0})\beta(s)(e^{\beta(s)(h_2-h_1)} - e^{-\beta(s)(h_2-h_1)})}{\Delta(s)} C_{dl}(s). \end{aligned} \qquad (3.26)$$

Since the total current is

$$I(s) = I_C(s) + I_D(s) + I_M(s), \qquad (3.27)$$

and the total potential drop (see Fig. 3.1) is

$$V(s) = \frac{I_C(s)}{sC} + R_1 I_C(s) + R_2 I(s), \qquad (3.28)$$

the impedance of the trilayer conjugated polymer actuator can be calculated using (3.21), (3.23), and (3.26):

$$Z(s) = \frac{V(s)}{I(s)} = R_2 + \frac{\delta\Delta(s)(1+sR_1C)}{sC\left(\delta\Delta(s) + d\beta(s)(2e^{-sT_0}-1)(e^{\beta(s)(h_2-h_1)} - e^{-\beta(s)(h_2-h_1)})\right)}. \qquad (3.29)$$

The model captures the dependence on the redox level C_0 through $\beta(s)$ defined in (3.13).

The model is consistent with the diffusive-elastic-metal model [16] when the migration dynamics and the oxidation dynamics are ignored.

3.1.4 Experiments and Discussions

The samples used in the experiments are fabricated by the Intelligent Polymer Research Institute at the University of Wollongong, Australia, and a description of the fabrication process can be found in, e.g., [58]. The PVDF layer is 110 μm thick, while each PPy layer is 30 μm thick. The electrolyte used is tetrabutylammonium hexafluorophosphate ($TBA^+PF_6^-$) in the solvent propylene carbonate (PC), where PF_6^- is the mobile anions that can transfer into and out of the PPy layer. Each actuator is soaked in the electrolyte for two hours before testing. The electrolyte stored in the PVDF layer enables the actuator to work in air for several hours. Notice that both PPy layers were already doped with certain PF_6^- during fabrication.

A dSPACE system (DS1104, dSPACE Inc) is used for data acquisition and processing. A trilayer actuator is clamped on one end, where electrical contacts are made using copper tapes coated with silver. The applied actuation voltage and the corresponding current are measured. All the experiments are conducted at temperatures between 22 °C and 24 °C.

The samples were predoped with PF_6^- during fabrication, and the nominal concentration C_0 in the absence of DC bias is estimated to be 1000 $\mathrm{mol/m^3}$ based on the deposition conditions. Different C_0 is obtained by applying DC biases of 0.5 V and 1 V, respectively, where the change in C_0 is calculated by dividing the transferred charges before reaching the steady state by the PPy volume. Sinusoidal voltages of amplitude 0.05 V and frequency 0.08 - 200 Hz are superimposed on the DC voltage, as perturbations, for the measurement of impedance spectrum. Electrolyte is prepared for two concentrations, 0.35 M and 0.25 M, for two sets of experiments. In each set, three samples of same dimensions and from the same fabrication batch are prepared and subject to DC voltages of 0 V, 0.5 V, and 1 V, respectively. The samples prepared with 0.35 M electrolyte have dimensions 15×5mm,

while those with 0.25 M electrolyte have dimensions 30×6mm. For the convenience of referencing, the samples with 0.35 M electrolyte are named Sample 1 (0 V), Sample 2 (0.5 V) and Sample 3 (1 V). The samples with 0.25 M electrolyte are named Sample 4, 5 and 6 in the same manner.

Some parameters of the model (3.29) are physical constants or can be measured directly, including gas constant $R = 8.3143$ J/mol $\cdot$ K, Faraday's constant $F = 96487$ C/mol, absolute temperature $T = 300$ K, and PPy thickness $h_2 - h_1 = 3 \times 10^{-5}$ m. Based on studies on the dielectric properties of conjugated polymers [59–61], the dielectric permittivity κ_e is taken to be $60\varepsilon_0$, where ε_0 represents the permittivity in vacuum. The double layer thickness δ is difficult to measure, and an estimation of 25 nm is used based on the range reported in [51].

Experiments are conducted to estimate the double-layer capacitance C, the nominal redox level C_0, and the resistances R_1 and R_2. If we assume that the internal capacitance of the polymer per unit volume is close to the double-layer capacitance per unit volume [16], C can be estimated using

$$C = \frac{Q}{U} \cdot \frac{\delta}{h_2 - h_1}, \tag{3.30}$$

where Q is the charge transferred under an applied DC voltage U. Fig. 3.2 shows the transferred charges under DC voltages from 0.2 V to 1.2 V for different samples, from which Q/U is estimated to be 0.13 for Sample 1, 2, 3, and 0.37 for Sample 4, 5, 6. Estimated values of C based on (3.30) are listed in Table 3.1. Also listed in the table are the values for the resistance R_1, which are estimated with a conductivity of 200 S/cm based on the studies on PPy doped with PF_6^- [52, 62] under room pressure and temperature. The results in Fig. 3.2, together with the sample dimensions, also enables us to compute the nominal anion concentrations (redox level) C_0, which are listed in Table 3.2. Finally, to measure R_2, a sinusoidal input $0.05\sin(500\pi t)$ V is applied. Note that the small amplitude ensures minimal influence on C_0. At this high frequency, the trilayer actuator is almost resistive

and the measured impedance is approximately $R_1 + R_2$. It is observed that R_1 is negligible compared with the measured resistance, thus R_2 is chosen to be the measured resistance. Since the redox level has impact on the resistance of the reduced PPy layer, values of R_2 will be different for different samples, as shown in Table 3.2. The only remaining parameters are the diffusion constant d and the time delay of oxidation T_0, which will be identified through curve fitting.

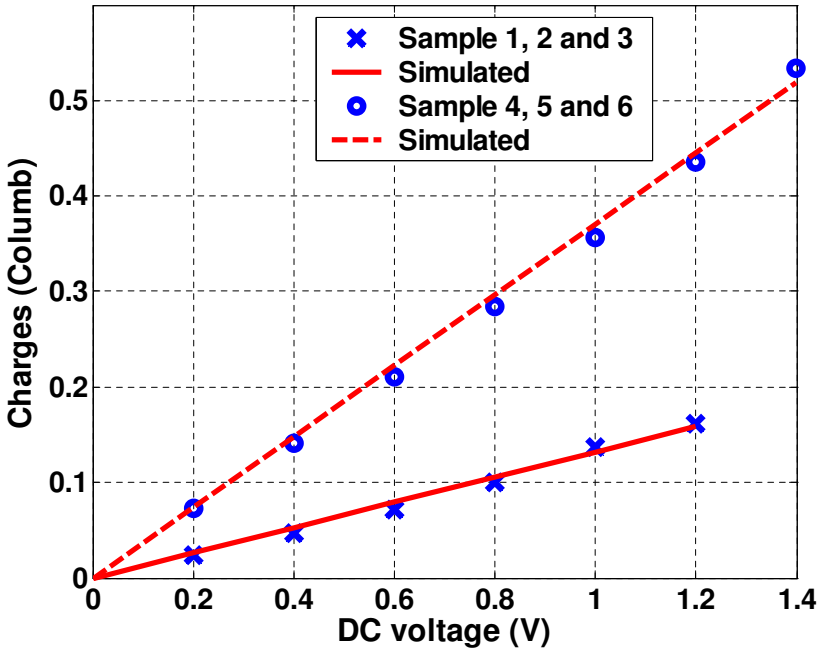

Figure 3.2: The relationship between transferred charges and applied voltage for different samples.

Table 3.1: Estimated values for C and R_1.

Parameter	Sample 1, 2 and 3	Sample 4, 5 and 6
C (F)	1.03×10^{-4}	3.17×10^{-4}
R_1 (Ω)	2×10^{-5}	8.3×10^{-6}

Experimentally measured impedance spectra have been used to verify the proposed redox level-dependent impedance model. For comparison purposes, the diffusive-elastic-metal model [16] has also been used. Besides the parameters estimated in the previous

Table 3.2: Estimated values for C_0 and R_2.

	$C_0(\text{mol}/\text{m}^3)$	$R_2(\Omega)$
Sample 1	1000	34.0
Sample 2	1323	46.3
Sample 3	1646	56.7
Sample 4	1000	26.6
Sample 5	1363	30.2
Sample 6	1726	50.3

subsection, the only free parameter for the diffusive-elastic-metal model is the diffusion constant d. For each set of experiments (0.35 M or 0.25 M electrolyte), the value of d is estimated by fitting the diffusive-elastic-metal model to the measured impedance spectrum under a DC voltage of 0 V. The same value will be used for the proposed model as well. The last parameter, T_0, for the proposed model, is obtained by fitting the measured impedance spectrum under a DC bias of 0.5 V. Then the measured spectra under DC voltages of 0 V and 1 V are compared to the predictions by the redox level-dependent model, without further tuning of any parameters, thus serving as independent checks on the proposed model. Note that the predictions by the diffusive-elastic-metal model do not vary with the DC bias.

Fig. 3.3 through Fig. 3.5 show the results for Sample 1 through Sample 3. Using the aforementioned methods, the values of d and T_0 are identified as: $d = 2.5 \times 10^{-}11\text{m}^2/\text{s}$, $T_0 = 1.9$ ns. It is found that, while the two models are comparable at a low redox level, the proposed model shows clear advantage at higher redox levels, as can be seen in Fig. 3.4 and Fig. 3.5. Consistent results are obtained for Sample 4 - Sample 6. Here d and T_0 are estimated to be $d = 1.5 \times 10^{-}11\text{m}^2/\text{s}$, $T_0 = 4$ ns. It is again seen that the proposed model is able to capture the redox-level dependent impedance, as shown in Fig. 3.6 through Fig. 3.8.

This work, for the first time, incorporates the effect of redox level into the dynamics of conjugated polymers in an integrative way, which enhances fundamental understanding of conjugated polymers and and facilitates the use of nonlinear control methods for effectively controlling these materials. The proposed method applies to general conjugated polymers

as well.

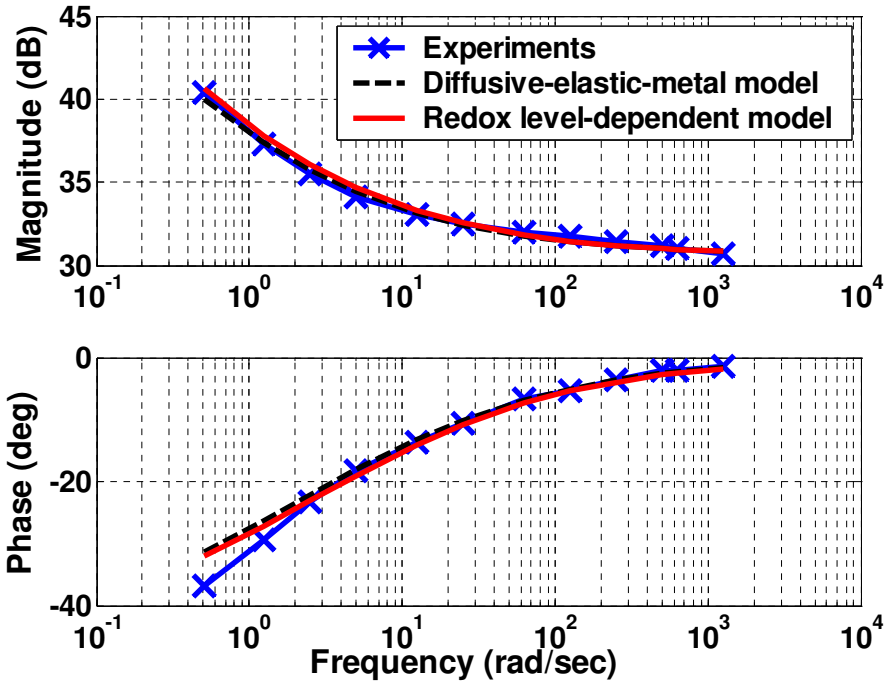

Figure 3.3: Model predictions versus experimental impedance for Sample 1 (0.35 M electrolyte, 0 V DC voltage).

3.2 Nonlinear Mechanical Model Based on a Swelling Framework

The complete actuation model structure has been discussed in Chapter 2. Extensive works have been done to understand the dynamic relationship between the amount of transferred ions and the applied potential. Another important aspect is to predict the mechanical output based on the swelling introduced by the transferred ions. The classical beam theory has been applied to model the bending curvature for bilayer PPy actuators [15, 27] and trilayer actuators as shown in Eq. (2.27). However, the model is only valid when the ion movement-induced swelling is small so that the following two assumptions hold: 1) the strain and

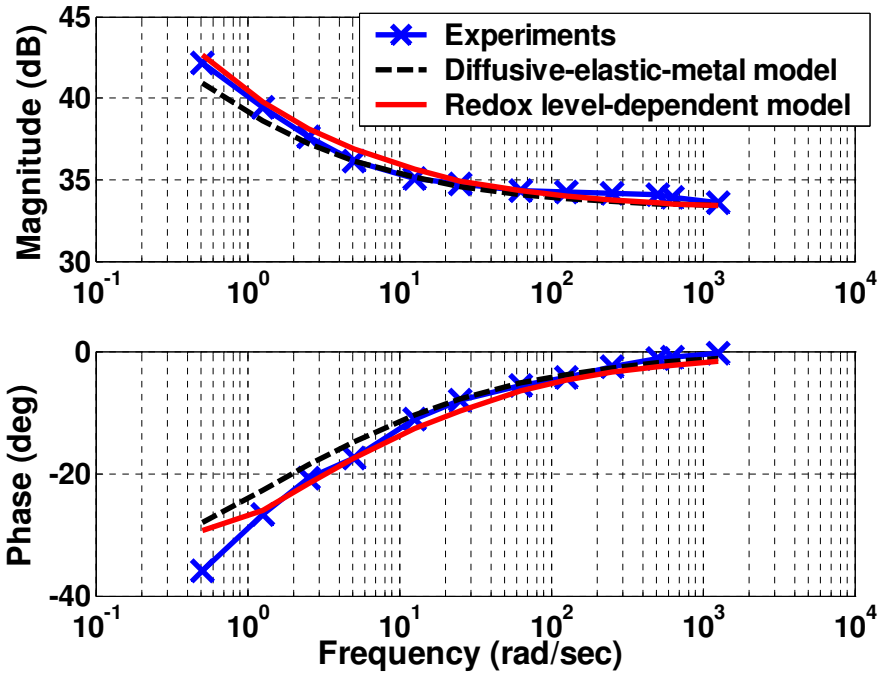

Figure 3.4: Model predictions versus experimental impedance for Sample 2 (0.35 M electrolyte, 0.5 V DC voltage).

the stress can be related linearly; 2) the geometry nonlinearities can be neglected. The tensile strength experiments have shown that the strain and stress relationship of PPy films becomes clearly nonlinear as the strain is increased over 4% [29,30]. These results indicate that the linear model based on the assumption that the stress varies linearly with the strain becomes invalid as the deformation gets large. Therefore, it is imperative to develop a nonlinear model to predict the actuator performance for applications where large actuation is involved.

Large swelling and bending present challenges to the mechanical model based on the linear elasticity theory. Firstly, when the deformation is large, the swelling effect and the bending effect are coupled and thus cannot be superimposed as those in (2.22) and (2.24) because of the geometric nonlinearities. Secondly, the strain-stress relationships of PVDF and PPy films become nonlinear as the strain increases [29,30,63,64]. Thirdly, under large swelling, the symmetrical trilayer arrangement generates a neutral line that is no longer at

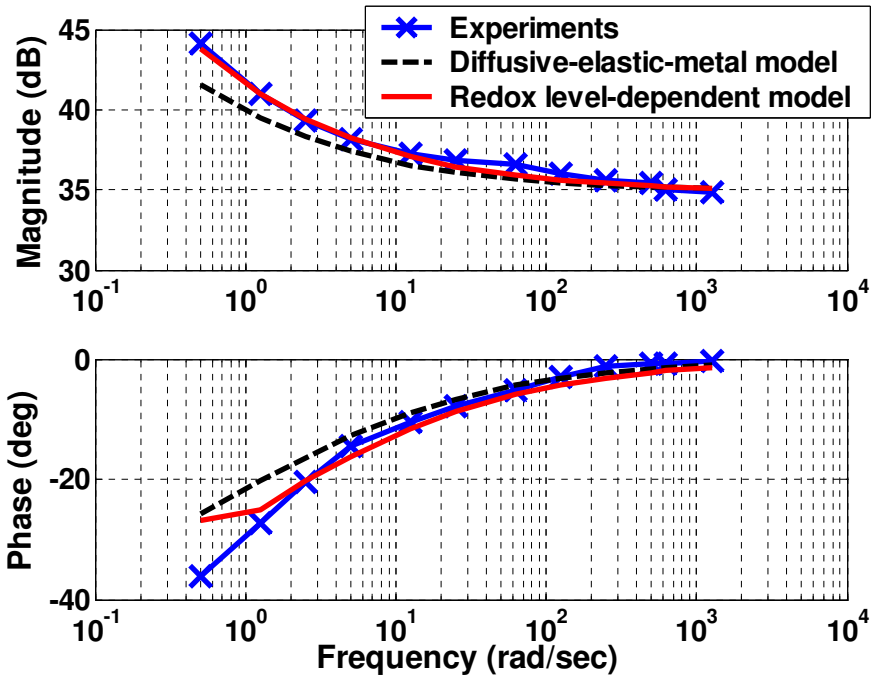

Figure 3.5: Model predictions versus experimental impedance for Sample 3 (0.35 M electrolyte, 1 V DC voltage).

the center line due to the geometric nonlinearity. Therefore, the nonlinear elasticity theory-based method is introduced in this section to model large bending motions.

We use ν_1 and ν_2 to denote the swellings of the reduced and oxidized PPy layer, respectively. The swelling is defined as the ratio between the volume after electrical actuation and the original volume. If $\nu_i > 1$, the volume is increased; if $\nu_i < 1$, the volume is decreased. Assuming that the volume change is proportional to the transferred charge density, one can calculate ν_1 and ν_2 at the steady state

$$\nu_1 = \frac{V_0 - k_2 \rho V_0}{V_0} = 1 - k_2 \rho, \tag{3.31}$$

$$\nu_2 = \frac{V_0 + k_2 \rho V_0}{V_0} = 1 + k_2 \rho, \tag{3.32}$$

where V_0 represents the original volume. The value of k_2 can be determined by experimental data, which has the order of $10^{-10}\mathrm{m}^3 \cdot \mathrm{C}^{-1}$ [16]. When one PPy layer is reduced and

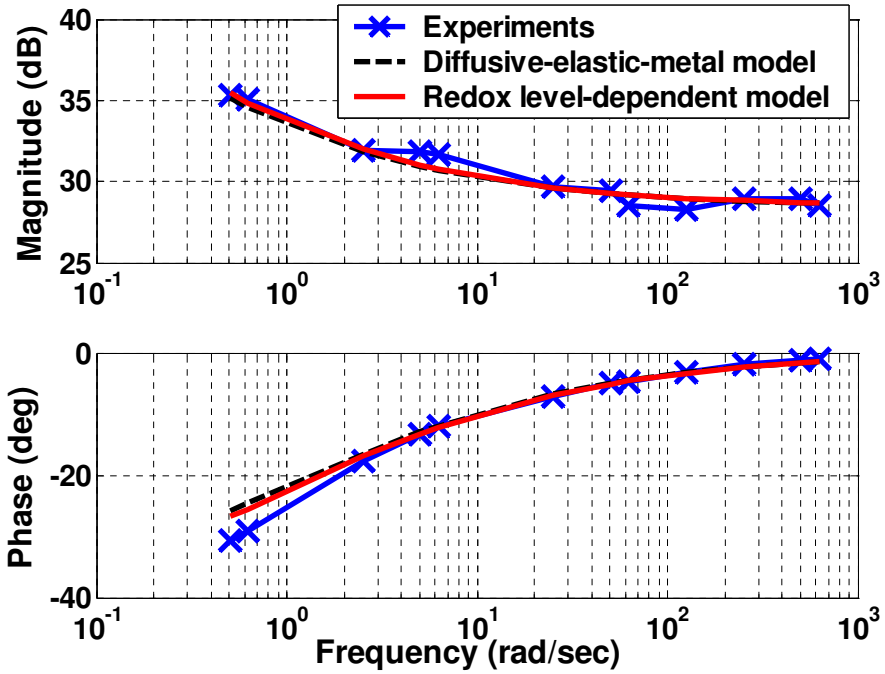

Figure 3.6: Model predictions versus experimental impedance for Sample 4 (0.25 M electrolyte, 0 V DC voltage).

repels dopants, the other PPy layer is oxidized and accepts dopants. Therefore, the PVDF layer is merely an ion conducting layer, and we assume that its volume does not change.

3.2.1 Finite Strain Tensors

In linear elasticity the infinitesimal strain tensor is used to capture the structural deformation, where "infinitesimal" implies that the theory is only valid as the displacement gradient is vanishingly small. However, the strain can be significant in many applications. Thus the finite strain tensors are introduced in nonlinear elasticity, which will be adopted below.

Consider a trilayer beam that bends because of differential swellings in the two outer layers. The reference configuration is in Cartesian coordinates, while the deformed configuration is in cylindrical coordinates for the convenience of modeling the bending. This is shown in Fig. 3.9, where x represents the thickness coordinate, y represents the length coordinate, and z stands for the width coordinate. The axes in the cylindrical coordinates are

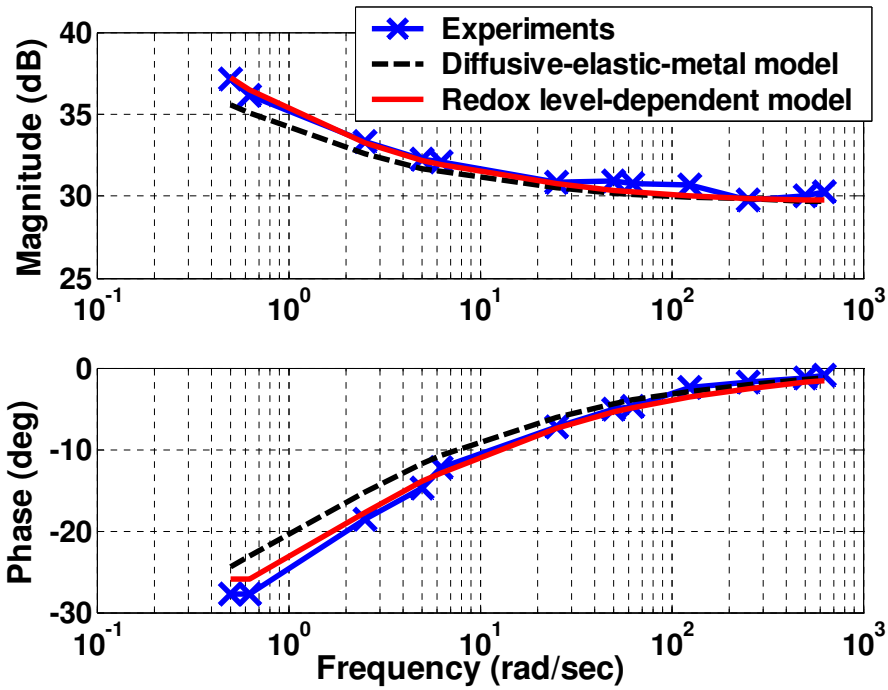

Figure 3.7: Model predictions versus experimental impedance for Sample 5 (0.25 M electrolyte, 0.5 V DC voltage).

labeled by r, θ and ς, which represent the radius, azimuth, and width coordinates, respectively. Because the length of the beam is usually much larger than the width, it is assumed that the there are no changes along the width direction z, which means

$$\varsigma = z. \tag{3.33}$$

The bending angle θ is considered to be proportional to the position along the y axis in the reference configuration,

$$\theta = \alpha y, \tag{3.34}$$

where α is a proportionality constant that will be determined by the analysis. The bending radius r is assumed to be independent of y and z,

$$r = r(x). \tag{3.35}$$

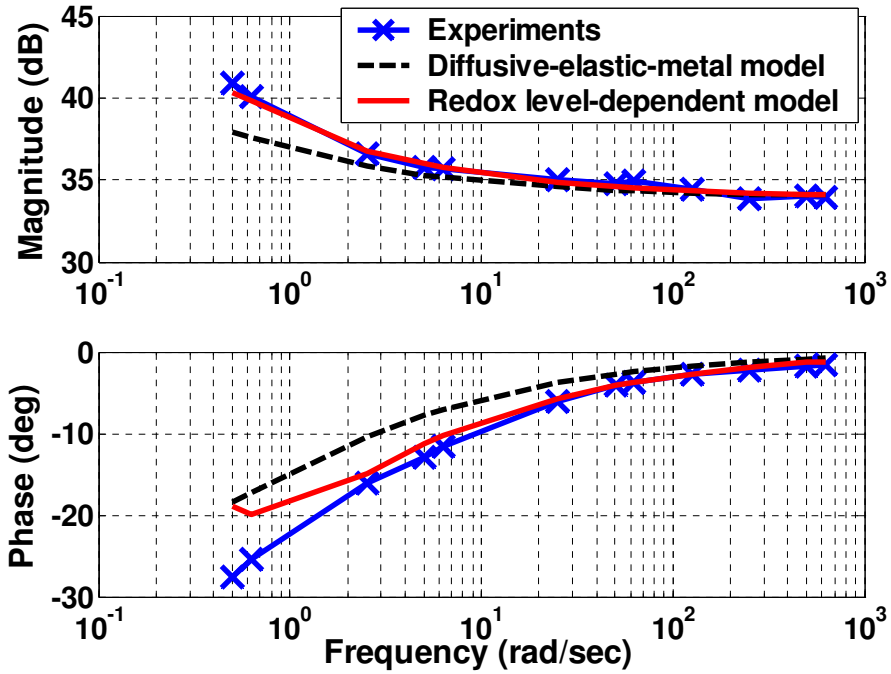

Figure 3.8: Model predictions versus experimental impedance for Sample 6 (0.25 M electrolyte, 1 V DC voltage).

The orthonormal basis vectors in the Cartesian coordinates are denoted by $\mathbf{e_x}$, $\mathbf{e_y}$, and $\mathbf{e_z}$, and they are denoted by $\mathbf{e_r}$, $\mathbf{e}_\theta$, and $\mathbf{e}_\varsigma$ in the cylindrical coordinates. By definition, these vectors are represented by

$$\begin{aligned}
\mathbf{e_x} &= \begin{pmatrix} 1 & 0 & 0 \end{pmatrix}', \quad \mathbf{e_r} = \begin{pmatrix} 1 & 0 & 0 \end{pmatrix}', \\
\mathbf{e_y} &= \begin{pmatrix} 0 & 1 & 0 \end{pmatrix}', \quad \mathbf{e}_\theta = \begin{pmatrix} 0 & 1 & 0 \end{pmatrix}', \\
\mathbf{e_z} &= \begin{pmatrix} 0 & 0 & 1 \end{pmatrix}', \quad \mathbf{e}_\varsigma = \begin{pmatrix} 0 & 0 & 1 \end{pmatrix}',
\end{aligned}$$

where " $'$ " denotes the transpose operation.

For ease of analysis, the dyadic product operation is denoted by the symbol $\otimes$. The

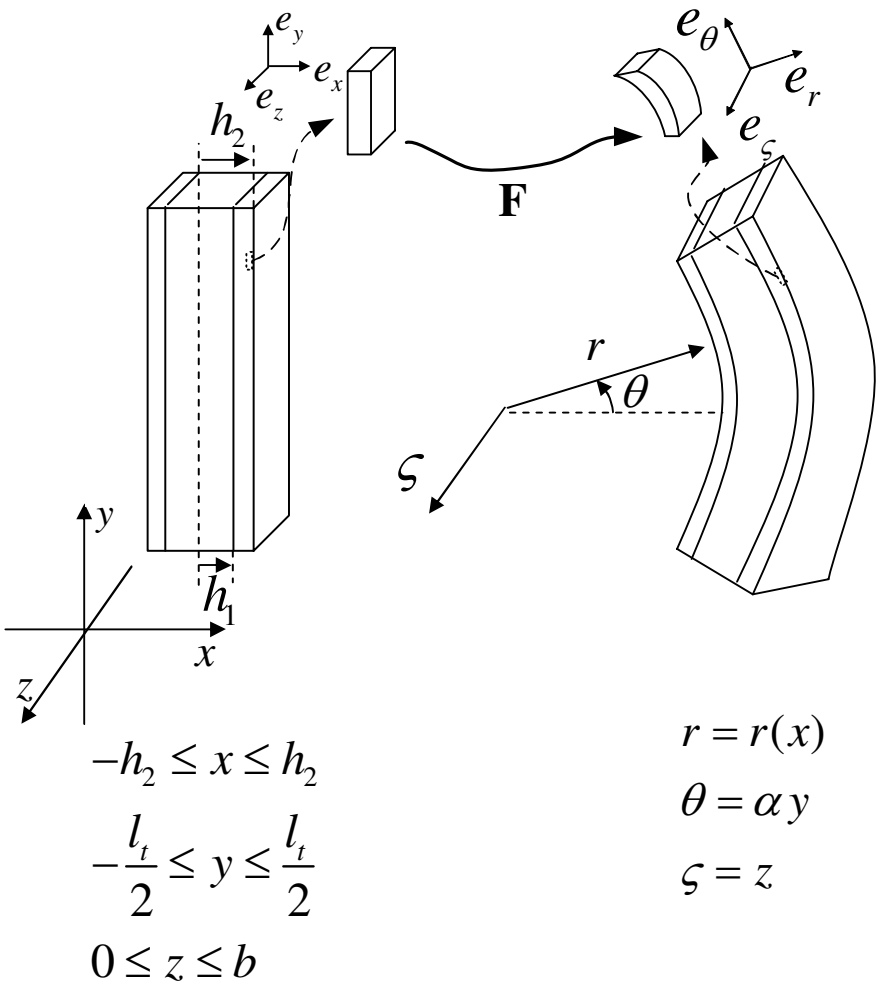

Figure 3.9: Illustration of the reference configuration and the deformed configuration.

meaning of $\otimes$ is illustrated as follows:

$$\begin{pmatrix} x_1 & x_2 & x_3 \end{pmatrix}' \otimes \begin{pmatrix} y_1 & y_2 & y_3 \end{pmatrix}' = \begin{pmatrix} x_1y_1 & x_1y_2 & x_1y_3 \\ x_2y_1 & x_2y_2 & x_2y_3 \\ x_3y_1 & x_3y_2 & x_3y_3 \end{pmatrix}. \tag{3.36}$$

This gives the matrix representations

$$\mathbf{e_r} \otimes \mathbf{e_x} = \begin{pmatrix} 1 & 0 & 0 \\ 0 & 0 & 0 \\ 0 & 0 & 0 \end{pmatrix}, \tag{3.37}$$

$$\mathbf{e}_\theta \otimes \mathbf{e_y} = \begin{pmatrix} 0 & 0 & 0 \\ 0 & 1 & 0 \\ 0 & 0 & 0 \end{pmatrix}, \tag{3.38}$$

$$\mathbf{e}_\varsigma \otimes \mathbf{e_z} = \begin{pmatrix} 0 & 0 & 0 \\ 0 & 0 & 0 \\ 0 & 0 & 1 \end{pmatrix}. \tag{3.39}$$

Suppose that the deformation takes $\mathbb{X} = (x, y, z)^T$ in the reference configuration to $\Psi = (r, \theta, \varsigma)^T$ in the deformed configuration. The deformation gradient is defined as

$$\mathbf{F} = \frac{\partial \Psi}{\partial \mathbb{X}} \quad \Longleftrightarrow \quad d\Psi = \mathbf{F} d\mathbb{X}, \tag{3.40}$$

where

$$\begin{aligned} d\Psi &= dr \cdot \mathbf{e_r} + r d\theta \mathbf{e}_\theta + d\varsigma \mathbf{e}_\varsigma, \\ d\mathbb{X} &= dx \mathbf{e_x} + dy \mathbf{e_y} + dz \mathbf{e_z}. \end{aligned}$$

From (3.33), (5.21), and (3.35), the deformation gradient is written as

$$\begin{aligned} \mathbf{F} &= \frac{dr}{dx} \mathbf{e_r} \otimes \mathbf{e_x} + r\alpha \mathbf{e}_\theta \otimes \mathbf{e_y} + \mathbf{e}_\varsigma \otimes \mathbf{e_z} \\ &= \begin{pmatrix} \frac{dr}{dx} & 0 & 0 \\ 0 & r\alpha & 0 \\ 0 & 0 & 1 \end{pmatrix}. \end{aligned} \tag{3.41}$$

The left Cauchy-Green deformation tensor is [65]

$$\begin{aligned}\mathbf{B} &= \mathbf{F}\mathbf{F}' = \lambda_r^2 \mathbf{e_r} \otimes \mathbf{e_r} + \lambda_\theta^2 \mathbf{e}_\theta \otimes \mathbf{e}_\theta + \mathbf{e}_\varsigma \otimes \mathbf{e}_\varsigma \\ &= \begin{pmatrix} \lambda_r^2 & 0 & 0 \\ 0 & \lambda_\theta^2 & 0 \\ 0 & 0 & 1 \end{pmatrix}, \end{aligned} \tag{3.42}$$

where

$$\lambda_r \triangleq \frac{dr}{dx}, \;\; \lambda_\theta \triangleq r\alpha. \tag{3.43}$$

For incompressible materials, the deformation satisfies the constraint that the volume is not changed by the bending after swelling, which means

$$\det \mathbf{F} = \nu, \tag{3.44}$$

where ν is defined to be the swelling ratio in the different layers,

$$\nu = \begin{cases} \nu_1, & \text{for the reduced PPy layer} \\ 1, & \text{for the PVDF layer} \\ \nu_2, & \text{for the oxidized PPy layer} \end{cases}. \tag{3.45}$$

From (3.83), the above equation can be written as

$$\frac{dr}{dx} = \frac{\nu}{\alpha r}, \tag{3.46}$$

implying that λ_r is a function of r, α, and ν. One can integrate (3.86) and obtain the following equation for the reduced PPy layer:

$$r(x) = \sqrt{r_1^2 + \frac{2}{\alpha}\int_{-h_2}^{x} \nu_1 dx}, \;\; -h_2 \leqslant x \leqslant -h_1, \tag{3.47}$$

where r_1 is defined as the radius at the inner surface of the beam, as shown in Fig. 3.10. Since the swelling is assumed to be uniform over the reduced PPy layer, one can simplify (3.47) to be

$$r(x) = \sqrt{r_1^2 + \frac{2\nu_1(x+h_2)}{\alpha}}, \quad -h_2 \leqslant x \leqslant -h_1. \tag{3.48}$$

Similar equations can be obtained for the PVDF and the oxidized PPy layers:

$$r(x) = \sqrt{r_2^2 + \frac{2(x+h_1)}{\alpha}}, \quad -h_1 \leqslant x \leqslant h_1, \tag{3.49}$$

$$r(x) = \sqrt{r_3^2 + \frac{2\nu_2(x-h_1)}{\alpha}}, \quad h_1 \leqslant x \leqslant h_2, \tag{3.50}$$

where r_2 is defined as the radius of the boundary between the reduced PPy layer and the PVDF layer, r_3 as the radius of the boundary between the PVDF layer and the oxidized PPy layer, and r_4 as the radius of the outer surface of the beam. The expressions for r_2, r_3 and r_4 are thus

$$r_2 = \sqrt{r_1^2 + \frac{2\nu_1(h_2-h_1)}{\alpha}}, \tag{3.51}$$

$$r_3 = \sqrt{r_2^2 + \frac{4h_1}{\alpha}}, \tag{3.52}$$

$$r_4 = \sqrt{r_3^2 + \frac{2\nu_2(h_2-h_1)}{\alpha}}. \tag{3.53}$$

3.2.2 Stresses

For an isotropic incompressible material, the Cauchy stress tensor depends on the elastic energy density function $\hat{W}$ as follows [65],

$$\boldsymbol{\sigma} = \frac{2}{\nu}\left[\frac{\partial \hat{W}}{\partial I_1}\mathbf{B} + \frac{\partial \hat{W}}{\partial I_2}(I_1\mathbf{B} - \mathbf{B^2})\right] - p\mathbf{I}, \tag{3.54}$$

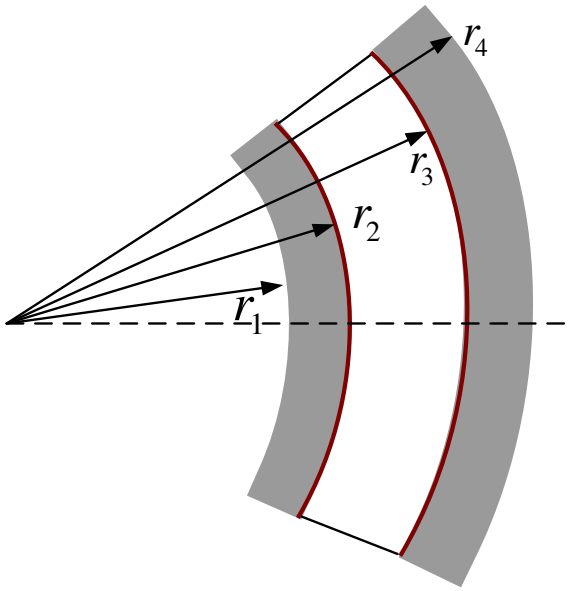

Figure 3.10: Definition of the bending radii at different locations.

where **I** is the identity matrix. Here p has the interpretation of unknown hydrostatic pressure. I_1 and I_2 are the invariants defined as follows,

$$I_1 = \text{trace}(\mathbf{B}) = 1 + \lambda_r^2 + \lambda_\theta^2 \tag{3.55}$$

$$I_2 = \frac{1}{2}[(\text{trace}(\mathbf{B}))^2 - \text{trace}((\mathbf{B})^2)] = \lambda_r^2 + \lambda_\theta^2 + \lambda_r^2\lambda_\theta^2. \tag{3.56}$$

Since I_1 and I_2 are functions of λ_r, λ_θ, which are in turn functions of r, α, and ν, it is possible to write

$$\hat{W}(I_1, I_2, \nu) = \tilde{W}(\lambda_r, \lambda_\theta, \nu) = W(r, \alpha, \nu). \tag{3.57}$$

In the development that follows, each of these is useful in different places.

Combining (3.54), (3.55), (3.56), and (3.57), one can verify that the principal Cauchy

stresses are given by

$$\sigma_{rr} = \frac{\lambda_r}{v}\frac{\partial \tilde{W}}{\partial \lambda_r} - p, \tag{3.58}$$

$$\sigma_{\theta\theta} = \frac{\lambda_\theta}{v}\frac{\partial \tilde{W}}{\partial \lambda_\theta} - p. \tag{3.59}$$

In the absence of body forces, the equilibrium configuration gives

$$\mathrm{div}\sigma = \mathbf{0}, \tag{3.60}$$

which holds within each of the three layers. From (3.46) and (3.58), σ_{rr} is a function of r only. Eq. (3.60) in the $\mathbf{e_r}$ direction then gives [31]

$$\frac{d\sigma_{rr}}{dr} + \frac{1}{r}(\sigma_{rr} - \sigma_{\theta\theta}) = 0. \tag{3.61}$$

Subtracting (3.59) from (3.58) and utilizing (3.57), one has

$$\sigma_{rr} - \sigma_{\theta\theta} = -\frac{r}{v}\frac{\partial W}{\partial r}. \tag{3.62}$$

We will use "PPy1" to denote the reduced PPy layer, and "PPy2" to denote the oxidized PPy layer. Considering the boundary condition $\sigma_{rr}^{PPy1}(r_1, \alpha, v_1) = 0$ and combining (3.61) and (3.62), one obtains the following expression for the principal Cauchy radial stress in the reduced PPy layer:

$$\sigma_{rr}^{PPy1} = \frac{1}{v_1}(W^{PPy1}(r, \alpha, v_1) - W^{PPy1}(r_1, \alpha, v_1)). \tag{3.63}$$

From (3.62) and (3.63), the principal Cauchy hoop stress in the reduced PPy layer is

$$\sigma_{\theta\theta}^{PPy1} = \frac{1}{v_1}(W^{PPy1}(r, \alpha, v_1) - W^{PPy1}(r_1, \alpha, v_1) + r\frac{\partial W^{PPy1}}{\partial r}). \tag{3.64}$$

Similar analysis can be used to derive the stresses in the PVDF and the oxidized PPy layer, which results in

$$\sigma_{rr}^{PVDF} = W^{PVDF}(r,\alpha) - W^{PVDF}(r_2,\alpha) + \sigma_{rr}^{PVDF}(r_2,\alpha), \tag{3.65}$$

$$\sigma_{rr}^{PPy2} = \frac{1}{\nu_2}(W^{PPy2}(r,\alpha,\nu_2) - W^{PPy2}(r_3,\alpha,\nu_2)) + \sigma_{rr}^{PPy2}(r_3,\alpha,\nu_2), \tag{3.66}$$

where $\sigma_{rr}^{PVDF}(r_2,\alpha)$ and $\sigma_{rr}^{PPy2}(r_3,\alpha,\nu_2)$ specify the interface values. Note that we have used the assumption of no swelling for the PVDF layer in (3.65). When there are no fractures or delamination between different layers, σ_{rr} on the interfaces of these layers is continuous, which gives

$$\sigma_{rr}^{PVDF}|_{r=r_2} = \sigma_{rr}^{PPy1}|_{r=r_2} =: \sigma_{rr}|_{r_2}, \quad \sigma_{rr}^{PPy2}|_{r=r_3} = \sigma_{rr}^{PVDF}|_{r=r_3} =: \sigma_{rr}|_{r_3}.$$

It follows from (3.63) and (3.65) that

$$\sigma_{rr}|_{r_2} = \frac{1}{\nu_1}(W^{PPy1}(r_2,\alpha,\nu_1) - W^{PPy1}(r_1,\alpha,\nu_1)),$$
$$\sigma_{rr}|_{r_3} = W^{PVDF}(r_3,\alpha) - W^{PVDF}(r_2,\alpha) + \frac{1}{\nu_1}(W^{PPy1}(r_2,\alpha,\nu_1) - W^{PPy1}(r_1,\alpha,\nu_1)).$$

Similar to (3.64), the following equations for hoop stresses in the PVDF layer and the other PPy layer can be derived,

$$\sigma_{\theta\theta}^{PVDF} = \sigma_{rr}^{PVDF} + r\frac{\partial W^{PVDF}}{\partial r}, \tag{3.67}$$

$$\sigma_{\theta\theta}^{PPy2} = \sigma_{rr}^{PPy2} + \frac{r}{\nu_2}\frac{\partial W^{PPy2}}{\partial r}. \tag{3.68}$$

3.2.3 Equilibrium

The force and bending moment at any cross section of the beam are zero at the equilibrium, which is similar to (2.31) and (2.21) but takes different expressions in the cylindrical

coordinates:

$$\int_{r_1}^{r_2} \sigma_{\theta\theta}^{PPy1} dr + \int_{r_2}^{r_3} \sigma_{\theta\theta}^{PVDF} dr + \int_{r_3}^{r_4} \sigma_{\theta\theta}^{PPy2} dr = 0, \tag{3.69}$$

$$\int_{r_1}^{r_2} \sigma_{\theta\theta}^{PPy1} r dr + \int_{r_2}^{r_3} \sigma_{\theta\theta}^{PVDF} r dr + \int_{r_3}^{r_4} \sigma_{\theta\theta}^{PPy2} r dr = 0. \tag{3.70}$$

To capture the nonlinear strain-stress relationship of the PVDF and PPy as the strain increases [29,30,63,64], the energy functions for PVDF and PPy layers are assumed to be of neo-Hookean types [66], which means that they take the general form of

$$W = \frac{\mu}{2}(I_1 - 3\nu^{2/3}), \tag{3.71}$$

where μ is the shear modulus. It therefore follows from (3.43), (3.86), (3.55), and (3.56) that

$$W_{PPy1}(r,\alpha,\nu_1) = \frac{1}{2}\mu_{PPy}[(\frac{\nu_1}{\alpha r})^2 + (\alpha r)^2 + 1 - 3\nu_1^{2/3}], \tag{3.72}$$

$$W_{PVDF}(r,\alpha) = \frac{1}{2}\mu_{PVDF}[(\frac{1}{\alpha r})^2 + (\alpha r)^2 - 2], \tag{3.73}$$

$$W_{PPy2}(r,\alpha,\nu_2) = \frac{1}{2}\mu_{PPy}[(\frac{\nu_2}{\alpha r})^2 + (\alpha r)^2 + 1 - 3\nu_2^{2/3}]. \tag{3.74}$$

The shear modulus μ_i is related to the small strain Young's modulus E_i by $\mu_i = E_i/3$, since the constraint (3.46) implies a Poisson ratio of 0.5. It is assumed that the energy functions for PVDF and PPy layers are of neo-Hookean types, because the neo-Hookean model contains the quadratic terms of the mechanical deformation gradient, and it has been adopted to model the nonlinear strain-stress relationships of different smart materials, such as PVDF [67, 68] and ionic polymer-metal composite (IPMC) [69]. Substituting (3.72),

(3.73), and (3.74) into (3.64), (3.67) and (3.68), one obtains

$$\sigma_{\theta\theta}^{PPy1} = \frac{\mu_{PPy}}{2\nu_1}[\alpha^2(3r^2 - r_1^2) - \frac{\nu_1^2}{\alpha^2}(\frac{1}{r^2} + \frac{1}{r_1^2})], \tag{3.75}$$

$$\sigma_{\theta\theta}^{PVDF} = \frac{\mu_{PVDF}}{2}[\alpha^2(3r^2 - r_2^2) - \frac{1}{\alpha^2}(\frac{1}{r^2} + \frac{1}{r_2^2})] + \sigma_{rr}|_{r_2}, \tag{3.76}$$

$$\sigma_{\theta\theta}^{PPy2} = \frac{\mu_{PPy}}{2\nu_2}[\alpha^2(3r^2 - r_3^2) - \frac{\nu_2^2}{\alpha^2}(\frac{1}{r^2} + \frac{1}{r_3^2})] + \sigma_{rr}|_{r_3}. \tag{3.77}$$

From (3.75), (3.76) and (3.77), the left hand side of (3.69) is expressed as

$$\begin{aligned}
&\int_{r_1}^{r_2} \sigma_{\theta\theta}^{PPy1} dr + \int_{r_2}^{r_3} \sigma_{\theta\theta}^{PVDF} dr + \int_{r_3}^{r_4} \sigma_{\theta\theta}^{PPy2} dr \\
&= \frac{r_4}{\nu_2}(W^{PPy2}(r_4, \alpha, \nu_1) - W^{PPy2}(r_3, \alpha, \nu_1)) + \sigma_{rr}|_{r_3} \cdot (r_4 - r_3) \\
&+ r_3(W^{PVDF}(r_3, \alpha, \nu_1) - W^{PVDF}(r_2, \alpha, \nu_1)) + \sigma_{rr}|_{r_2} \cdot (r_3 - r_2) \\
&+ \frac{r_2}{\nu_1}(W^{PPy1}(r_2, \alpha, \nu_1) - W^{PPy1}(r_1, \alpha, \nu_1)).
\end{aligned} \tag{3.78}$$

Substituting (3.72), (3.73), and (3.74) into (3.78), one finds that the force balance (3.69) becomes

$$\begin{aligned}
&\frac{\mu_{PPy}}{2\nu_2}[\frac{\nu_2^2}{\alpha^2}(\frac{1}{r_4^2} - \frac{1}{r_3^2}) + \alpha^2(r_4^2 - r_3^2)] + \frac{\mu_{PVDF}}{2}[\frac{1}{\alpha^2}(\frac{1}{r_3^2} - \frac{1}{r_2^2}) + \alpha^2(r_3^2 - r_2^2)] \\
&+ \frac{\mu_{PPy}}{2\nu_1}[\frac{\nu_1^2}{\alpha^2}(\frac{1}{r_2^2} - \frac{1}{r_1^2}) + \alpha^2(r_2^2 - r_1^2)] = 0.
\end{aligned} \tag{3.79}$$

Note that (3.79) also ensures the boundary condition $\sigma_{rr}^{PPy2}(r_4, \alpha, \nu_2) = 0$. From (3.75), (3.76) and (3.77), one can find that the moment balance (3.70) becomes

$$\begin{aligned}
&\frac{\mu_{PPy}}{\nu_1}\{\frac{3}{4}\alpha^2(r_2^4 - r_1^4) + (\frac{\nu_1}{\alpha})^2 \ln\frac{r_1}{r_2} + \frac{1}{2}(r_1^2 - r_2^2)[(\frac{\nu_1}{\alpha r_1})^2 + (\alpha r_1)^2]\} \\
&+ \mu_{PVDF}\{\frac{3}{4}\alpha^2(r_3^4 - r_2^4) + (\frac{\nu_1}{\alpha})^2 \ln\frac{r_2}{r_3} + \frac{1}{2}(r_2^2 - r_3^2)[(\frac{1}{\alpha r_2})^2 + (\alpha r_2)^2]\} \\
&+ \frac{\mu_{PPy}}{\nu_2}\{\frac{3}{4}\alpha^2(r_4^4 - r_3^4) + (\frac{\nu_1}{\alpha})^2 \ln\frac{r_3}{r_4} + \frac{1}{2}(r_3^2 - r_4^2)[(\frac{\nu_1}{\alpha r_3})^2 + (\alpha r_3)^2]\} = 0.
\end{aligned} \tag{3.80}$$

In summary, the problem is now formulated as solving the nonlinear equations (3.79) and (3.80) simultaneously to obtain the two unknown variables r_1 and α. These two variables capture the deformed configuration for given swellings ν_1 and ν_2. Note that in the linear elasticity theory-based method, the force balance is automatically satisfied for a symmetrical trilayer structure. However, (3.79) is required in the nonlinear elasticity theory-based method. Newton's method is applied to numerically solve (3.79) and (3.80) with the aid of (3.51)−(3.53). Thus a large bending strain model is established for the trilayer conjugated polymer actuator with actuation voltage as the input and bending radius as the output.

3.2.4 Experimental Verification

The PPy layer is 30 μm thick, and the PVDF layer is 110 μm thick, which implies that the values of the parameters h_1 and h_2 are 55μm and 85μm, respectively. The electrolyte used is 0.05 M tetrabutylammonium hexafluorophosphate ($TBA^+PF_6^-$) in the solvent propylene carbonate (PC). Two actuators of different dimensions are cut from the fabricated sheet. The size of two samples are 12.8×5.0 mm^2 (Sample 1) and 31.2×6.0 mm^2 (Sample 2) respectively. Each actuator is stored in the electrolyte before experiments for five hours to ensure that the PVDF layer is sufficiently soaked with electrolyte.

The relationships between the input voltages and the transferred charges for the two different samples are shown in Fig. 3.11. The constant k_1 in (2.15) can be determined from the experimental data, which is found to be 0.0936 C/V and 0.1801 C/V, respectively, for Sample 1 and 2. The value of the swelling-to-charge ratio κ_2 obtained through fine tuning based on the reported value in [16], which results in $k_2 = 1.12 \times 10^{-10}$ m$^3 \cdot$C^{-1}. The small strain Young's moduli of PPy and PVDF are taken to be 60 MPa and 612 MPa [13],respectively.

The predictions of r_1 and α on the basis of (3.79) and (3.80) are shown in Fig. 3.12 − Fig. 3.15 for the two samples. The experimental data for the bending radii are also compared with the predictions of r_1 in Fig. 3.12 and Fig. 3.13 for the two samples. The

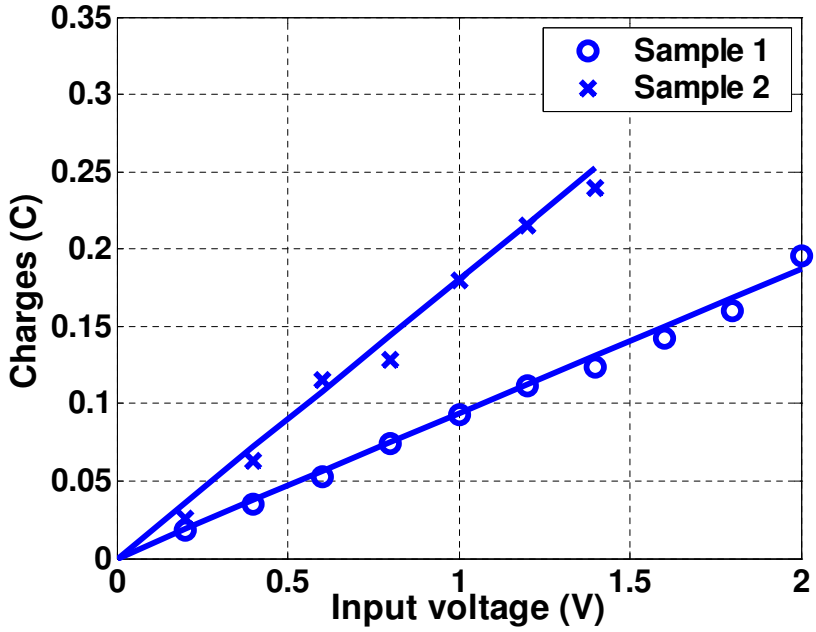

Figure 3.11: The relationships between the input voltages and the transferred charges for the two different samples.

predictions by the linear model (2.29) are also shown in the figures for comparison purposes. Note that the same parameters are used in the linear model. It can be seen that when the applied voltage is low, (i.e., the volume changes of the PPy layers are small), the predictions by the linear and nonlinear models can both fit the experimental data. But as the applied voltage increases, the prediction of the linear model deviates significantly from the experimental data. On the other hand, the nonlinear model still shows good fitting, thus demonstrating the effectiveness of the nonlinear model over a larger deformation range.

Based on the obtained values of r_1 and α, one can calculate r_2, r_3 and r_4 by using (3.51), (3.52) and (3.53). Furthermore the thickness of PPy layers can be obtained by calculating $r_2 - r_1$ and $r_4 - r_3$ at different actuation voltages. Similarly the thickness of PVDF layer is obtained through $r_3 - r_2$. The results for Sample 1 are shown in Fig. 3.16 and Fig. 3.17. When the voltage increases, the thickness of the reduced PPy layer will decrease and that of the oxidized PPy layer will increase for the oxidized PPy layer. The change percentage at 2 V is -0.83% for the reduced PPy layer and 0.67% for the oxidized PPy layer. The

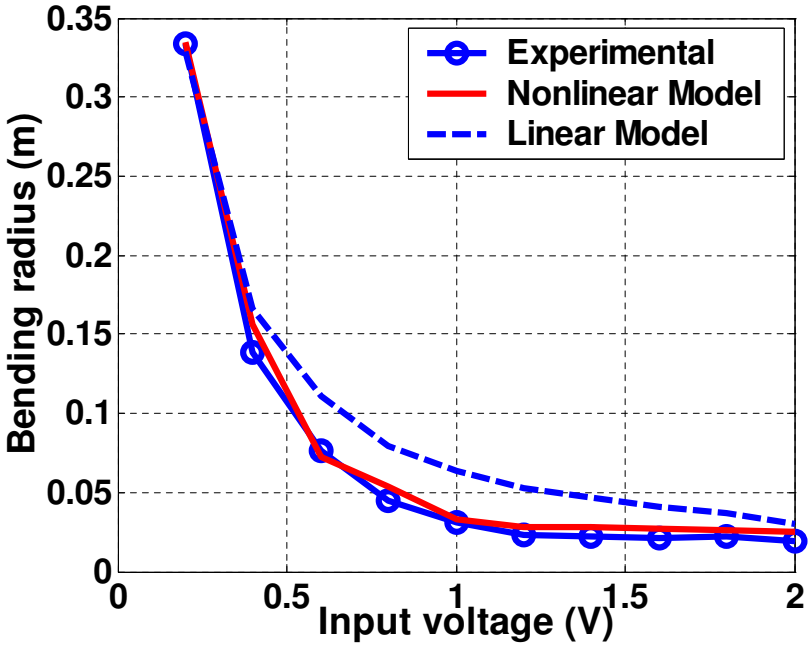

Figure 3.12: Quasi-static bending under different actuation voltages for Sample 1 (13×5 mm).

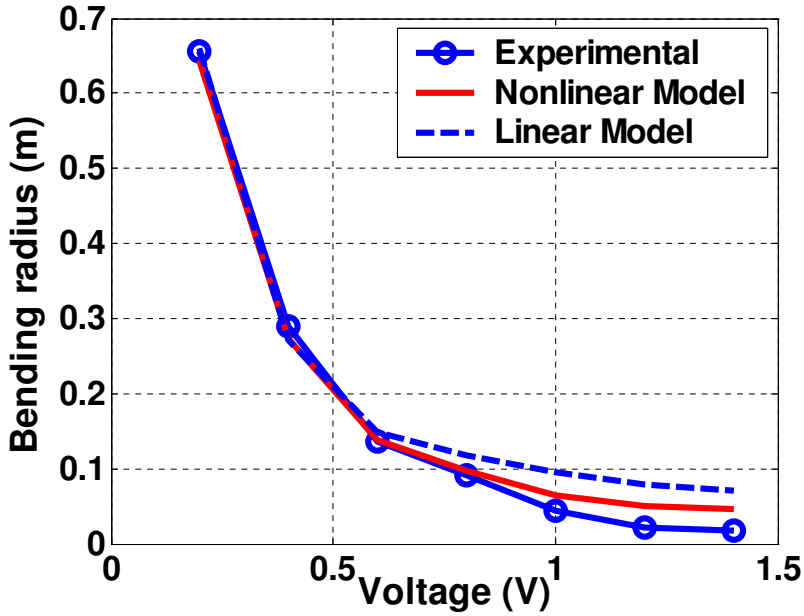

Figure 3.13: Quasi-static bending under different actuation voltages for Sample 2 (33×6 mm).

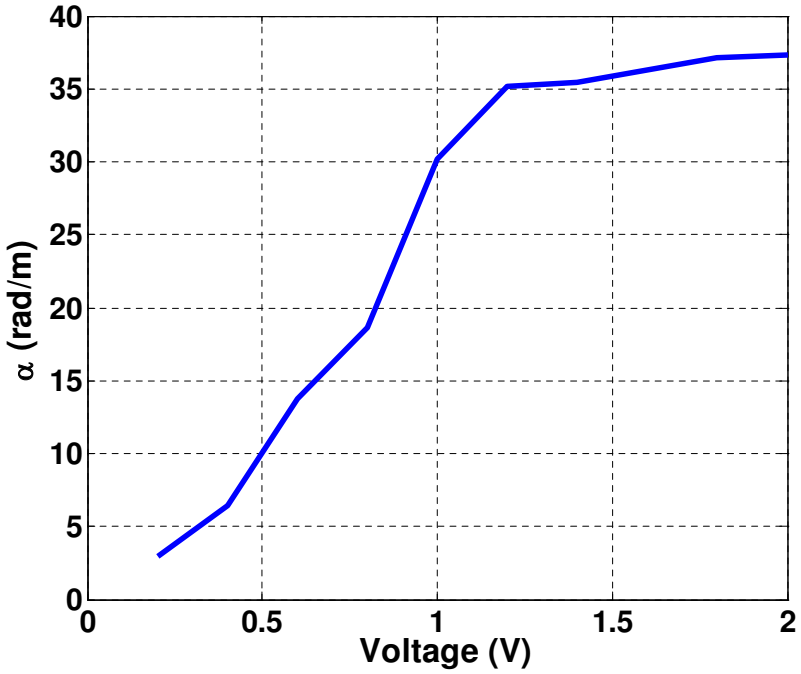

Figure 3.14: Computational results on the change of α versus the applied voltage for Sample 1 (13×5 mm).

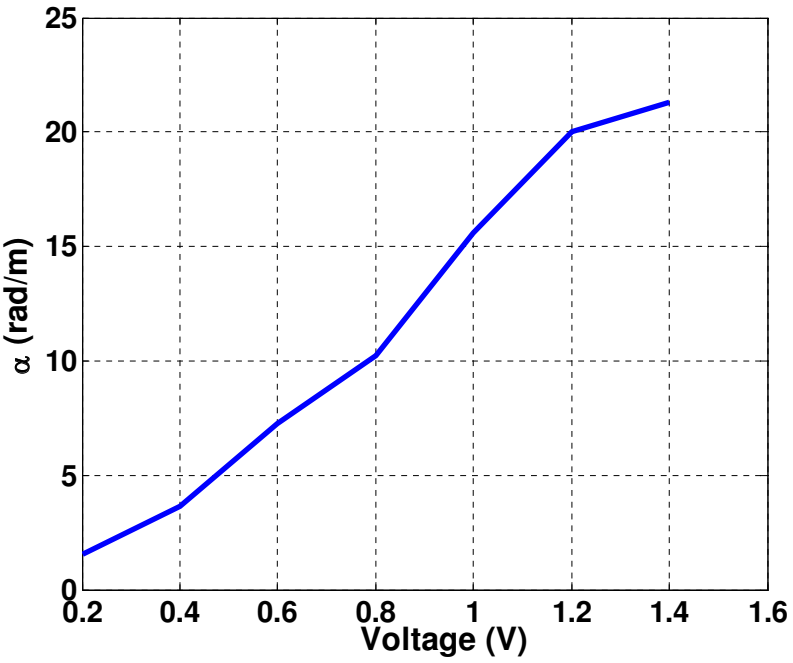

Figure 3.15: Computational results on the change of α versus the applied voltage for Sample 2 (33×6 mm).

thickness of the PVDF layer is decreasing but at a slower rate when the input voltage is increasing. The change percentage at 2 V is 0.21%. Note that these results provide interesting insight into the deformed configuration. Such information is not available from linear models, since the latter assume fixed thickness throughout the deformation.

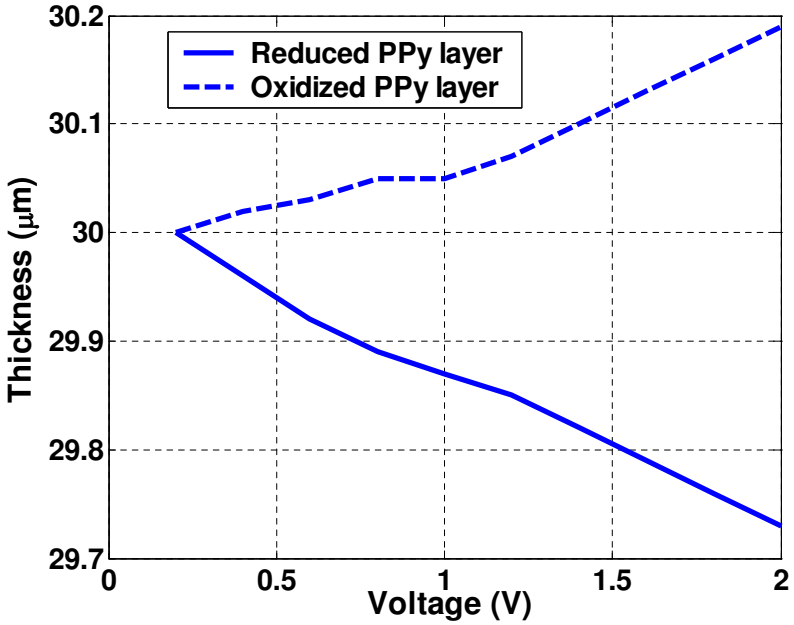

Figure 3.16: Computational results on the changes of thickness of the PPy layers with the applied voltage for Sample 1.

3.3 Fiber-directed Conjugated Polymer Torsional Actuator

Different configurations of conjugated polymer actuators have been exploited. Bilayer and trilayer benders are investigated in [8, 32], which utilize the strain difference in different layers of a beam to generate bending motion. Linear extenders are investigated in [7], where the conjugated polymer is immersed in electrolyte and the volume is changed as ion transfer between the polymer and electrolyte takes place under an applied potential.

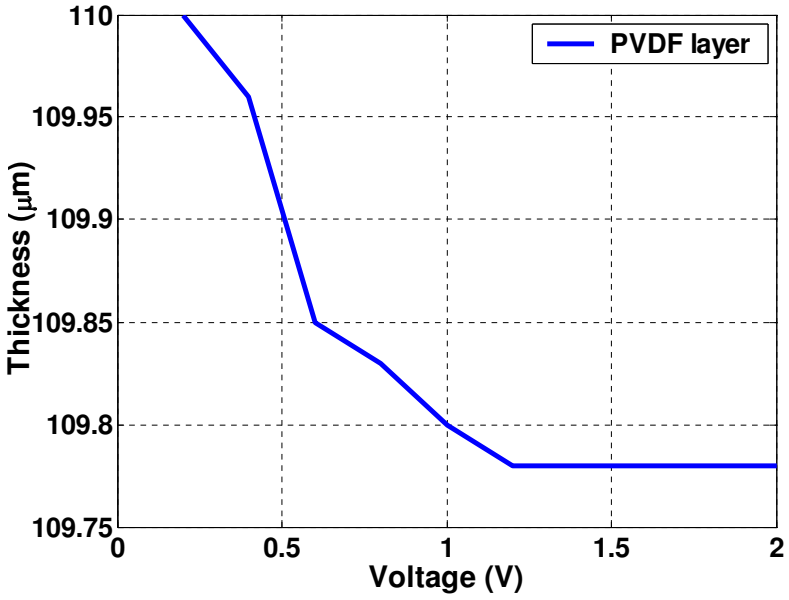

Figure 3.17: Computational results on the changes of thickness of the PVDF layer with the applied voltage for Sample 1.

However, more complicated actuator motions will be required. For example, torsional motion is highly desirable in microsurgery and other robotic applications. Fiber-reinforced elastic material can generate complicated deformation [70–72]. The anisotropy associated with the interaction between the fibers and the material matrix makes the material resist elongation in certain directions, which generates torsional motion when the volume of the material changes [33]. This principle provides a potentially useful approach to fabricating compact torsional actuators using conjugated polymer. Also conjugated polymer is an ideal material to realize the design of fiber reinforced elastic material actuator in practice, since the volume of the polymer can be changed easily with electrical actuation.

A conjugated polymer tube was fabricated by Ding *et al*. [73], where platinum wires were integrated into conjugated polymer during fabrication process. However, the purpose for the platinum wires in that paper was to increase the electrical conductivity along the tube, so the torsional motion introduced by the fiber-directed structure was not investigated. To the best of the author's knowledge, there has been no detailed investigation on torsional

motion in a fiber-reinforced conjugated polymer actuators.

In this dissertation, torsional motion of a fiber-directed conjugated polymer actuator is investigated from both theoretical and experimental perspectives. A nonlinear elasticity-based model is proposed to capture the relationship between the actuation voltage and the torsional motion of the conjugated polymer tube. Compared with a linear elasticity-based model, this model is able to capture the large deformations. The model is verified with experimental measurements made on a platinum fiber-directed conjugated polymer tube.

Fiber-reinforced elastic materials can generate complicated deformation when subject to swelling. When the fibers are aligned in special ways, the material matrix containing fibers will expand in the direction perpendicular to the fiber [33]. A specific case is studied where the fiber is helically wound about a elastic tube with a fixed pitch angle, which is illustrated in Fig. 3.18. The elastic material we consider here is PPy, the volume of which can be changed through electrical activation. Theoretical analysis shows that the tube will generate torsional motion when subject to swelling. Platinum wires are chosen to be integrated into PPy tube during the fabrication with some pitch angle β.

To fabricate the actuator, it is crucial to integrate the fibers into the material matrix of PPy. This would ensure that, when the PPy tube volume changes, the torsional motion will be generated when the motion in other directions are constrained. For this purpose, firstly a glass cylinder with a diameter of 2.5 mm is used as the substrate and coated uniformly with gold through sputtering. Then a platinum wire with diameter of 25 μm is wound uniformly along the glass cylinder. The pitch angle β is 80^{o}. This tube is soaked in the electrolyte (0.05M $Li^{+}TFSI^{-}$ in Propylene Carbonate) and connected to the working electrode of a potentiostat (OMNI101 from Cypress Systems). An electrochemical deposition process is conducted by following the method in [13]. To maintain a constant potential on PPy when PPy grows on the surface of glass tube, an Ag/AgCl reference electrode (Aldrich Chemical) is used. The auxiliary electrode is a stainless steel mesh. The electrolyte used in experiment is a mixed solution of 0.1M pyrrole, 0.1M LiTFSI in Propylene Carbonate

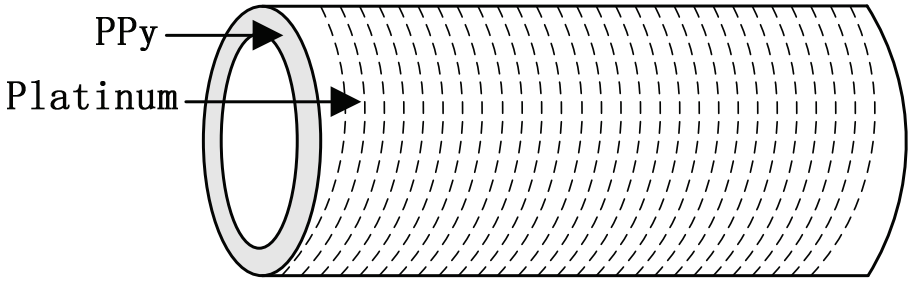

(a)

(b)

Figure 3.18: (a) Illustration of the conjugated polymer-based torsional actuator; (b) picture of the fabricated torsional actuator.

with 0.5w/w% water. The current density is maintained at 2 mA/cm^2 for good uniformity. Different PPy tube wall thickness can be achieved by controlling the deposition time. The PPy wall integrates the platinum wire during the deposition. Then because the sputtered gold layer has poor adhesion force with the PPy inner surface, the PPy tube can be easily taken off from the glass cylinder. The inner diameter of the tube can be controlled by choosing different glass cylinder diameters.

3.3.1 Nonlinear Mechanical Modeling Framework

The original and deformed configurations are shown in Fig. 3.20, where **F** represents the deformation gradient, which can map vectors (expressed in $\mathrm{Z}, \mathrm{R}, \Theta$ domain) in the original configuration to vectors (expressed in z, r, θ domain) in the deformed configuration. The pitch angle is defined as β ($0 < \beta < 90^o$) [33].

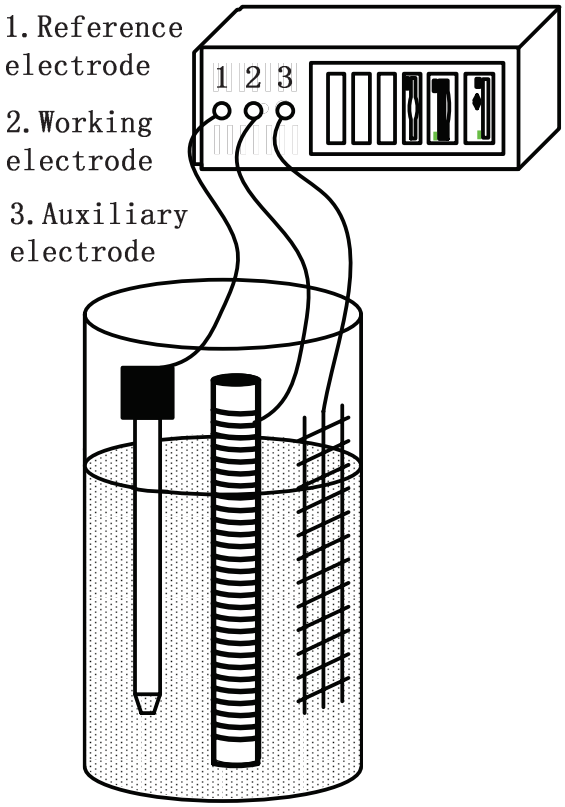

Figure 3.19: The experimental setup to fabricate the fiber-directed conjugated polymer actuator.

The deformation can be characterized by the following equation:

$$r = r(R), \;\; \theta = \Theta + \kappa Z, \;\; z = \lambda_z Z, \tag{3.81}$$

where κ is the twist per unit length, and λ_z is the elongation per unit length in the longitudinal direction. Suppose that the deformation takes a particle at location $\mathbf{X}$ in the reference configuration to the location $\mathbf{x}$ in the deformed configuration. The deformation gradient is defined as

$$\mathbf{F} = \frac{\partial \mathbf{x}}{\partial \mathbf{X}}, \tag{3.82}$$

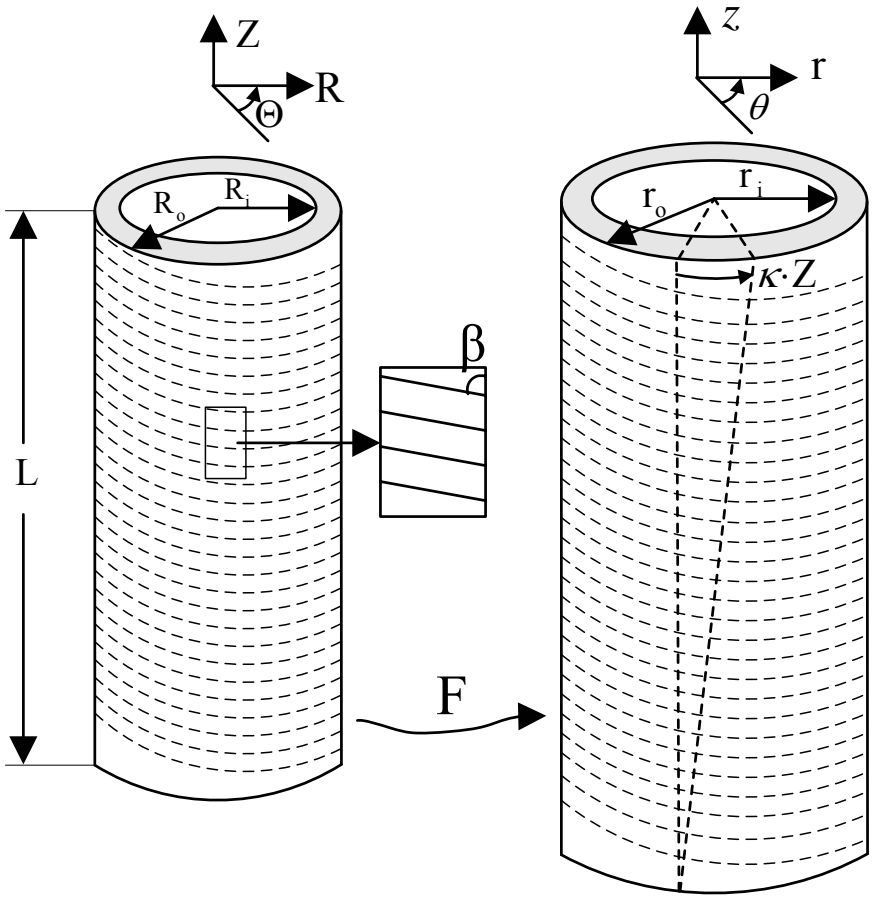

Figure 3.20: Illustration of the actuator configuration. Left: original configuration; right: deformed configuration.

where

$$\begin{aligned} \partial \mathbf{X} &= dR\,\mathbf{e}_R + Rd\Theta\,\mathbf{e}_\Theta + dZ\,\mathbf{e}_Z, \\ \partial \mathbf{x} &= dr\,\mathbf{e}_r + rd\theta\,\mathbf{e}_\theta + dz\,\mathbf{e}_z, \end{aligned}$$

$\mathbf{e}_R, \mathbf{e}_\Theta$, and $\mathbf{e}_Z$ are the orthonormal unit vectors in the original configuration, and $\mathbf{e}_r, \mathbf{e}_\theta$,and $\mathbf{e}_z$ are the orthonormal unit vectors in the deformed configuration. The deformation gradient tensor is

$$\mathbf{F} = \frac{dr}{dR}\mathbf{e}_r \otimes \mathbf{e}_R + \frac{r}{R}\mathbf{e}_\theta \otimes \mathbf{e}_\Theta + \kappa r \mathbf{e}_\theta \otimes \mathbf{e}_Z + \lambda_z \mathbf{e}_z \otimes \mathbf{e}_Z, \tag{3.83}$$

where $\otimes$ is the dyadic product. We assume that PPy is mechanically incompressible both before and after swelling. This assumption is based on relevant literature [74]. So the deformation satisfies the constraint that the volume is not changed by the deformation after swelling, which means

$$\det \mathbf{F} = \nu. \tag{3.84}$$

This, together with (3.83), implies

$$\frac{1}{R}\lambda_z r \frac{dr}{dR} = \nu. \tag{3.85}$$

Rewriting (3.85) as $rdr = \frac{\nu}{\lambda_z} RdR$ and integrating, we get

$$r^2 = r_i^2 + \frac{2}{\lambda_z}\int_{R_i}^{R} \nu R dR, \tag{3.86}$$

where r_i and R_i are the inner radii of the tube in the original configuration and the deformed configuration, respectively. The left Cauchy-Green deformation tensor is defined by

$$\mathbf{B} = \mathbf{F}\mathbf{F}^{\mathbf{T}}. \tag{3.87}$$

Following (3.83) and (3.85), $\mathbf{B}$ can be further expressed as

$$\begin{aligned} \mathbf{B} &= \frac{\nu^2 R^2}{\lambda_z^2 r^2}\mathbf{e}_r \otimes \mathbf{e}_r + (\kappa^2 + \frac{1}{R^2}) r^2 \mathbf{e}_\theta \otimes \mathbf{e}_\Theta \\ &\quad + \kappa\lambda_z r(\mathbf{e}_\theta \otimes \mathbf{e}_z + \mathbf{e}_z \otimes \mathbf{e}_\theta) + \lambda_z^2 \mathbf{e}_z \otimes \mathbf{e}_z. \end{aligned} \tag{3.88}$$

The principal invariants of $\mathbf{B}$ are defined as

$$I_1 = \mathrm{tr}(\mathbf{B}),\ \ I_2 = I_3 \mathrm{tr}(\mathbf{B}^{-1}),\ \ I_3 = \det(\mathbf{B}). \tag{3.89}$$

From (3.83), the invariant I_1 is obtained as

$$I_1 = \frac{v^2 R^2}{\lambda_z^2 r^2} + \frac{r^2}{R^2} + \kappa^2 r^2 + \lambda_z^2. \tag{3.90}$$

The elastic energy function of PPy can be denoted by Φ_m and modeled in the neo-Hookean form as

$$\Phi_m = \frac{1}{2}\mu(I_1 - 3v^{2/3}), \tag{3.91}$$

where μ is a material elastic constant that can be taken as $E_{PPy}/3$, where E_{PPy} is the Young's modulus [48].

Let $\mathbf{M}$ be the unit vector in the reference configuration that defines the fiber direction in the material matrix:

$$\mathbf{M} = \sin\beta \mathbf{e}_\Theta + \cos\beta \mathbf{e}_Z, \tag{3.92}$$

where β is the pitch angle defined in Fig. 3.20. Given the deformation gradient $\mathbf{F}$, the unit vector $\mathbf{M}$ is mapped into

$$\mathbf{m} = \mathbf{F}\mathbf{M} = (\kappa\cos\beta + \frac{1}{R}\sin\beta)\gamma\mathbf{e}_\theta + \lambda_z \cos\beta \mathbf{e}_z. \tag{3.93}$$

The square of the stretch of the fiber under actuation is

$$I_4 = \mathrm{tr}(\mathbf{m}\otimes\mathbf{m}) = (\kappa\cos\beta + \frac{1}{R}\sin\beta)^2\gamma^2 + \lambda_z^2\cos^2\beta. \tag{3.94}$$

The strain energy function of the fiber can be modeled as

$$\Phi_f = \frac{1}{2}\gamma(I_4 - 1)^2, \tag{3.95}$$

where γ is another material constant that may be taken as proportional to $E_{platinum}$. The proportionality constant will depend on the volume fraction of fibers in the overall composite.

Using the connection between the nonlinear theory and the linear theory of anisotropic elasticity [75], we may take $\gamma = \frac{1}{5}E_{platinum}$ in this investigation. Therefore, the total energy of the fiber-reinforced PPy actuator is

$$W = \Phi_m + \Phi_f. \tag{3.96}$$

The Cauchy stress tensor is [33]

$$\sigma = \frac{1}{\nu}\frac{\partial W}{\partial \mathbf{F}}\mathbf{F}^T - p\mathbf{I}. \tag{3.97}$$

Considering the expression of total energy in (3.96), the Cauchy stress can be written as [33]

$$\sigma = \frac{2}{\nu}\frac{\partial \Phi_m}{\partial I_1}\mathbf{B} + \frac{2}{\nu}\frac{\partial \Phi_f}{\partial I_4}\mathbf{m}\otimes\mathbf{m} - p\mathbf{I}. \tag{3.98}$$

Considering (3.88) and (3.93), we can express (3.98) as

$$\begin{aligned}\sigma &= \sigma_{rr}\mathbf{e}_r\otimes\mathbf{e}_r + \sigma_{\theta\theta}\mathbf{e}_\theta\otimes\mathbf{e}_\theta + \sigma_{\theta z}(\mathbf{e}_\theta\otimes\mathbf{e}_z + \mathbf{e}_z\otimes\mathbf{e}_\theta)\\ &\quad + \sigma_{zz}\mathbf{e}_z\otimes\mathbf{e}_z,\end{aligned} \tag{3.99}$$

where

$$\sigma_{rr} = -p + \frac{\mu\nu R^2}{\lambda_z^2 r^2}, \tag{3.100}$$

$$\begin{aligned}\sigma_{\theta\theta} &= -p + \frac{\mu r^2}{\nu}(\kappa^2 + \frac{1}{R^2})\\ &\quad + \frac{2\gamma r^2}{\nu}(\kappa\cos\beta + \frac{1}{R}\sin\beta)^2(I_4 - 1),\end{aligned} \tag{3.101}$$

$$\sigma_{zz} = -p + \frac{\mu}{\nu}\lambda_z^2 + \frac{2\gamma}{\nu}\lambda_z^2(I_4 - 1)\cos^2\beta, \tag{3.102}$$

$$\begin{aligned}\sigma_{\theta z} &= \frac{\mu}{\nu}\kappa\lambda_z r + \frac{2\gamma}{\nu}\lambda_z r\cos\beta(\kappa\cos\beta\\ &\quad + \frac{1}{R}\sin\beta)(I_4 - 1).\end{aligned} \tag{3.103}$$

This framework is built on strain energy functions and general deformation gradients, and it is thus valid for both small and large deformations.

3.3.2 Boundary Conditions

The boundary conditions on the conjugated polymer actuator are specified as follows:

$$\sigma_{rr}|_{R=R_i} = 0, \;\; \sigma_{rr}|_{R=R_0} = 0, \tag{3.104}$$

which represent that there is no direct loading applied to the inner and outer lateral surfaces. Notice that R is used in (3.104) since r is also a function of R. The equilibrium equation $\mathrm{div}\sigma = 0$ in the directions of r, z, and θ can be written as follows:

$$\frac{\partial \sigma_{rr}}{\partial r} + \frac{1}{r}\frac{\partial \sigma_{r\theta}}{\partial \theta} + \frac{\partial \sigma_{rz}}{\partial z} + \frac{1}{r}(\sigma_{rr} - \sigma_{\theta\theta}) = 0, \tag{3.105}$$

$$\frac{\partial \sigma_{rz}}{\partial r} + \frac{1}{r}\frac{\partial \sigma_{\theta z}}{\partial \theta} + \frac{\partial \sigma_{zz}}{\partial z} + \frac{\sigma_{rz}}{r} = 0, \tag{3.106}$$

$$\frac{\partial \sigma_{r\theta}}{\partial r} + \frac{1}{r}\frac{\partial \sigma_{\theta\theta}}{\partial \theta} + \frac{\partial \sigma_{z\theta}}{\partial z} + \frac{2\sigma_{r\theta}}{r} = 0, \tag{3.107}$$

where $\sigma_{r\theta} = 0$, $\sigma_{rz} = 0$ in this case. Considering (3.101), (3.102), and (3.103), one can show that (3.106) and (3.107) reduce to $\frac{\partial p}{\partial z} = 0$ and $\frac{\partial p}{\partial \theta} = 0$, which means that p is a function of r only. Given $\sigma_{r\theta} = 0$ and $\sigma_{rz} = 0$, one can write (3.105) as follows by using (3.85):

$$\frac{d\sigma_{rr}}{dR} = -\frac{\nu R}{\lambda_z r^2}(\sigma_{rr} - \sigma_{\theta\theta}), \tag{3.108}$$

which can be furthermore expanded by considering (3.100)

$$\frac{dp}{dR} = \frac{\nu R}{\lambda_z r^2}(\sigma_{rr} - \sigma_{\theta\theta}) + \frac{\mu\nu}{\lambda_z^2}\frac{d}{dR}(\frac{R^2}{r^2}). \tag{3.109}$$

Integrating (3.109) after substituting the expression of (3.100) minus (3.101), one can obtain the expression of p by using the boundary condition $\sigma_{rr}|_{R=R_0} = 0$:

$$p = \frac{\nu R^2 \mu}{\lambda_z^2 r^2} - \int_R^{R_0} (\mu(\frac{\nu^2 R^3}{\lambda_z^3 r^4} - \frac{R(R^2\kappa^2+1)}{\lambda_z R^2}) - \frac{2R\gamma}{\lambda_z}(\kappa cos\beta + \frac{1}{R} sin\beta)^2 (I_4 - 1))dR. \tag{3.110}$$

Applying the other boundary condition $\sigma_{rr}|_{R=R_i} = 0$ in (3.110) gives the following constraint equation:

$$\Delta = 0, \tag{3.111}$$

where

$$\Delta = \int_{R_i}^{R_o} (\frac{\mu}{2}(-\frac{\nu^2 R^2}{\lambda_z^2 r^4} + \kappa^2 + \frac{1}{R^2}) + (\kappa \cos\beta + \frac{1}{R} sin\beta)^2 \gamma (I_4 - 1))RdR. \tag{3.112}$$

3.3.3 Nonlinear Mechanical Model

One can see from Fig. 3.20 that three variables quantify the deformed configuration: r, λ_z, and κ. Because the profile of r can be calculated based on (3.86), variable r can be replaced by r_i to characterize the deformation together with the other two variables. Eq. (3.112) has provided one constraint equation. The other two require knowledge of the moment T and axial load P, which are given by the following expressions:

$$T = 2\pi \int_{r_i}^{r_o} \sigma_{\theta z} r^2 dr, \tag{3.113}$$

$$P = 2\pi \int_{r_i}^{r_o} \sigma_{zz} r dr. \tag{3.114}$$

When the end of the tube is not constrained, it follows that $T = 0$ and $P = 0$. These two equations, along with (3.111), provide three nonlinear equations for r_i, κ, and λ_z. One

finds that: the expression (3.112) is strongly dependent on r_i, the expression (3.113) for T is strongly dependent on κ, and the expression (3.114) for P is strongly dependent on λ_z. In general, the numerical analysis to obtain these variables by solving three nonlinear equations is difficult. Therefore in this thesis, λ_z, representing the length change ratio in the axial direction, will be measured and used as a given parameter. Since Δ and T give the strongest dependence on r_i and κ, the equations $\Delta = 0$ and $T = 0$ are retained in the analysis and numerically solved to obtain r_i and κ. By substituting from (3.103), one can integrate (3.113) and obtain the following expression:

$$T = \mu a\kappa + \gamma(b_0 + b_1\kappa + b_2\kappa^2 + b_3\kappa^3) = 0, \tag{3.115}$$

where a, b_0, b_1, b_2 and b_3 are terms involving material constants. Similarly one can integrate (3.112) and obtain the expression for Δ as follows:

$$\Delta = \mu\Omega + \gamma\Gamma, \tag{3.116}$$

where Ω and Γ are also terms involving material properties and λ_z, κ, and r_i, which will not be listed in this thesis due to the page limitation. The two unknown variables r_i and κ can be obtained by numerically solving the coupled equations $\Delta = 0$ and $T = 0$ using (3.115) and (3.116).

3.3.4 Sample Preparation and Experimental Setup

Three factors are changed during fabrication to study their influence on the performance of the actuators, which are the PPy thickness, the pitch angle, and the inner radius. Two PPy thicknesses, 0.381 mm and 0.686 mm, are obtained using different deposition duration. Two different pitch angles are obtained during the winding process, which are 60 ^{o} and 80 ^{o}. Two glass tubes with different radii are used to change the inner radii of the tube, which

are 2.2 and 1.3 mm. Four samples are fabricated that are named Sample 1, 2, 3, and 4. Their parameters are listed in Table 3.3. The length is kept as 33.5 mm for all four samples.

Table 3.3: Geometric parameters of the samples.

	thickness (mm)	pitch angles (degree)	radius (mm)
Sample 1	0.381	80	1.3
Sample 2	0.381	80	2.2
Sample 3	0.686	80	2.2
Sample 4	0.686	60	2.2

A computer equipped with a DS1104 R&D Controller Board (dSPACE Inc) is used for data acquisition and processing. A voltage is applied across the PPy tube and the counter electrode, which is a stainless steel mesh in the experiments. The PPy tube is soaked in 0.1M Li^+TFSI^- in Propylene Carbonate (PC). Sticky copper film is attached to different positions of the PPy tube for measurement purposes. Three motion signals are captured to characterize the tube deformation, which are the inner radius r_i, torsional displacement y at the end of the tube as shown in Fig. 3.21, and the length change at the end of the tube that equals to $\lambda_z \cdot L$ based on (3.81), where L is the length of the PPy tube. The model-predicted variables r_i and λ_z can be correlated directly to the measured variables, while κ is obtained based on the geometric relationship in Fig. 3.21:

$$y = R_m \tan(\kappa \cdot L), \tag{3.117}$$

where y is the measured displacement, and R_m is 4 mm in this thesis.

3.3.5 Experimental Results and Discussions

The quasi-static response is studied by applying a low frequency sinusoidal voltage on the actuator. The frequency is chosen to be 0.005 Hz to allow the actuator to reach the quasi-static condition. The sinusoidal voltage amplitude is 3.6 V. Because only one laser sensor is

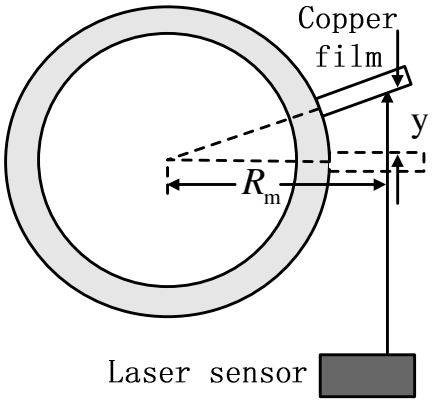

Figure 3.21: Experimental setup to measure κ. The copper film is attached perpendicular to the outer surface at the tube bottom.

available, measurements of inner radius, torsional displacement, and length change are performed separately and then synchronized through the voltage signal. The Young's moduli of platinum and PPy are chosen to be 168 GPa and 80 MPa in model prediction [48, 76].

The experimental results for Sample 1, 2, 3, and 4 are listed as follows. It is observed in experiments that the inner radius and torsional displacement signals have reversed phases. In particular, when the inner radius decreases, the torsional displacement increases. As discussed in Sec. 5.2, the length change will be used to obtain λ_z and taken as a given parameter to reduce the difficulties in numerical analysis. Therefore the model-predicted inner radius and torsional displacement are compared with the experimental data for different samples. In general, the model can predict the reversed phase of these two signals. The model can also predict the response change from different samples. The comparison between Fig. 3.22 and Fig. 3.25 shows the trend that a larger tube radius leads to a larger torsional displacement, when other parameters are kept the same. The comparison between Fig. 3.25 and Fig. 3.28 shows the trend that a thinner tube generates a larger torsional displacement. The comparison between Fig. 3.28 and Fig. 3.30 shows the trend that a smaller winding angle results in a larger torsional displacement. Therefore the experiments and model prediction suggest that a configuration with larger radius, thinner tube thickness,

and smaller winding angle tend to generate large torsional motion.

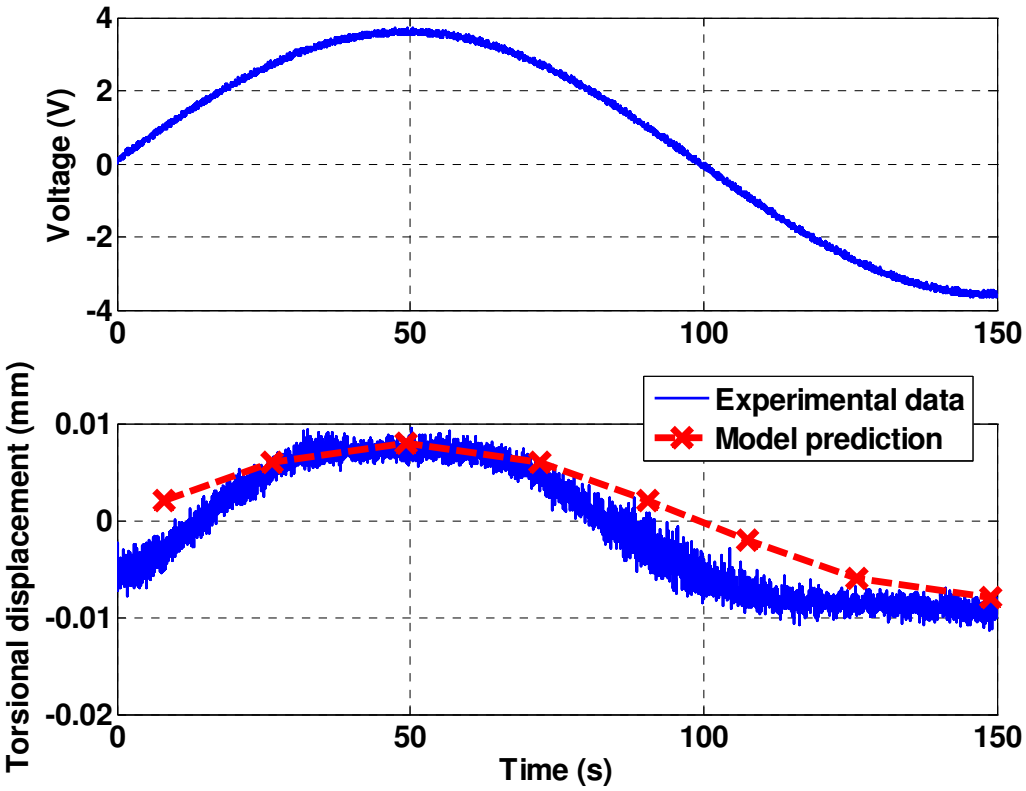

Figure 3.22: The torsional displacement of Sample 1 with 0.005 Hz sinusoidal voltage input.

3.4 Chapter Summary

In the electromechanical domain, a redox level-dependent impedance model was proposed for conjugated polymer actuators. The model was derived based on a nonlinear partial differential equation that incorporates the dynamics of ion diffusion, ion migration, and polymer oxidation, which was linearized using perturbation techniques. The linearized PDE was solved analytically in the Laplace domain, with proper boundary conditions enforced. Comparison with experimental results supported that the proposed model is able to capture the influence of redox level on the impedance spectrum. The model provides an effective way to integrate the diffusion and migration effects of ion flux in conjugated

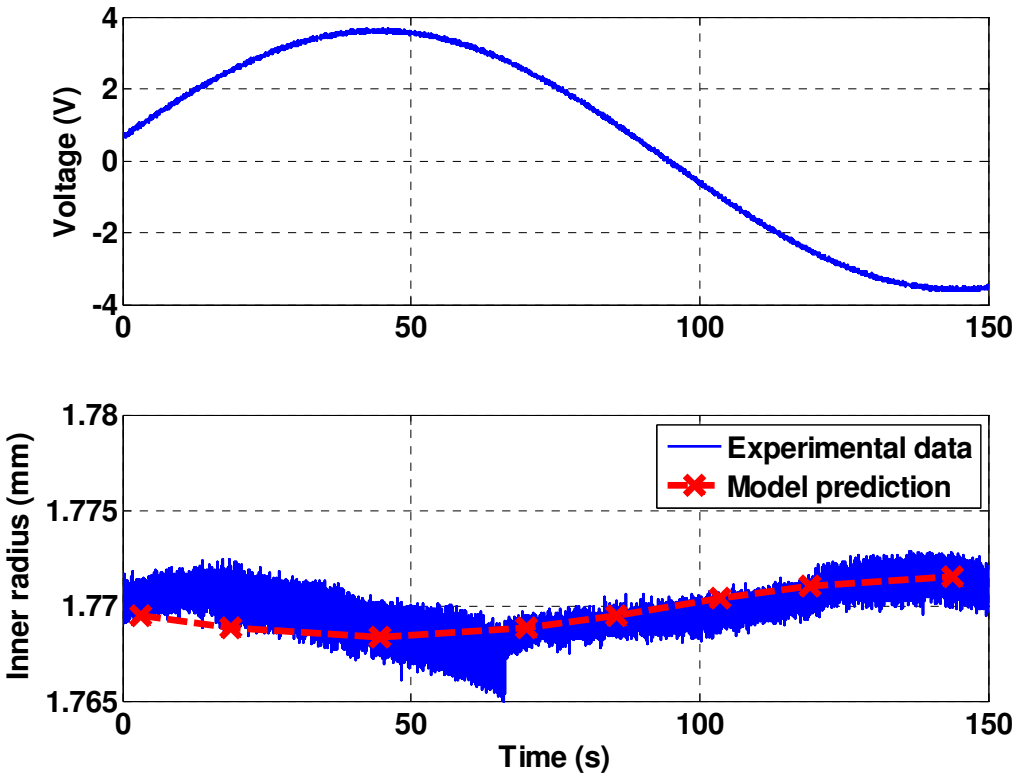

Figure 3.23: The change of inner radius of Sample 1 with 0.005 Hz sinusoidal voltage input.

polymers, which used to be treated separately with different models [57, 77]. The proposed model not only contributes to fundamental understanding of the complicated, redox level-dependent electrochemical behavior, but also holds potential for nonlinear control of conjugated polymer actuators.

In the mechanical domain, a nonlinear elasticity theory-based framework is proposed to analyze the bending configuration of a trilayer conjugated polymer beam under different actuation voltages. Neo-Hookean type strain energy functions are used for the PPy and PVDF layers of the trilayer beam to capture the nonlinearity under large deformations. For a constant actuation voltage, the swelling of each PPy layer is determined by the amount of transferred ions. The bending configuration at the equilibrium is obtained by solving the force and moment balance equations simultaneously. Experimental results have validated the effectiveness of the proposed nonlinear model. The method further provides insight into

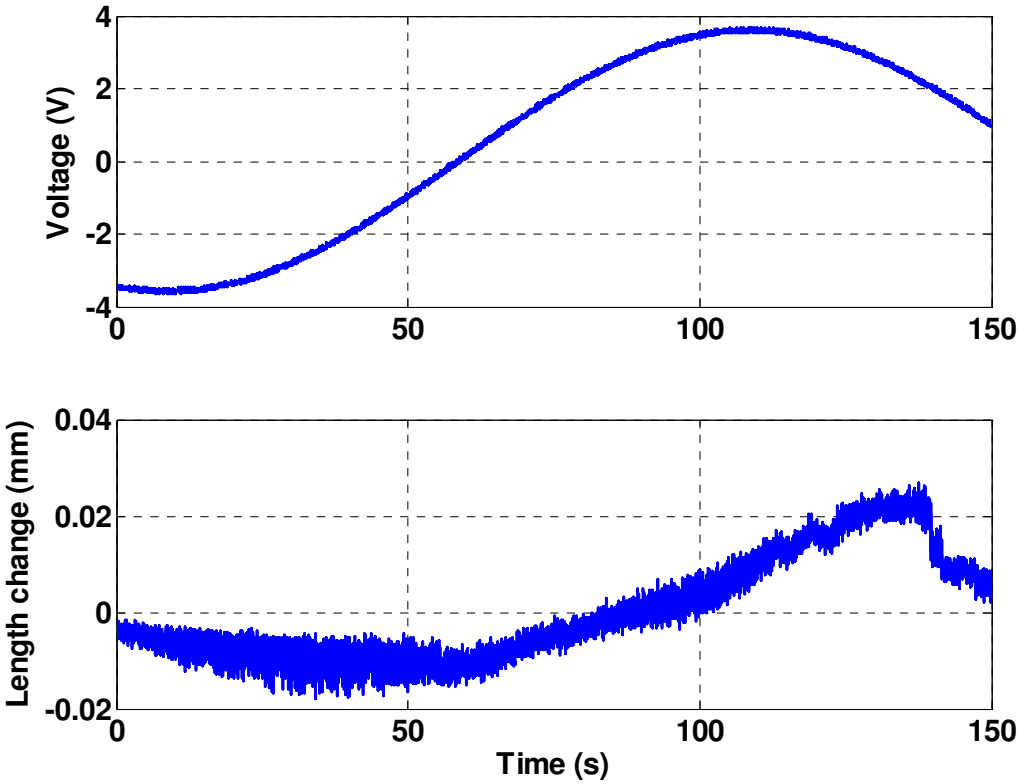

Figure 3.24: The change of tube length of Sample 1 with 0.005 Hz sinusoidal voltage input.

the deformation details, such as the change of layer thickness. Similar analysis can be used for some other EAPs that involve the local volume change (swelling). This is important for many applications involving large deformations, when the elastic modulus of the material already becomes nonlinear and linear elasticity analysis does not hold.

A fiber-directed conjugated polymer actuator is fabricated by integrating platinum wires into conjugated polymer during fabrication. Experiments have demonstrated that the tube-shaped conjugated polymer actuator can generate torsional deformation, when its volume is changed by applying an actuation voltage across itself and the electrolyte. Three important factors are changed during the fabrication process to make conjugated polymer tubes with different configurations, including the tube thickness, the tube radius, and the pitch angle of the platinum wires on the tube. A nonlinear elasticity-based model is utilized to capture the actuator performance, which holds for both small and large deformations. The

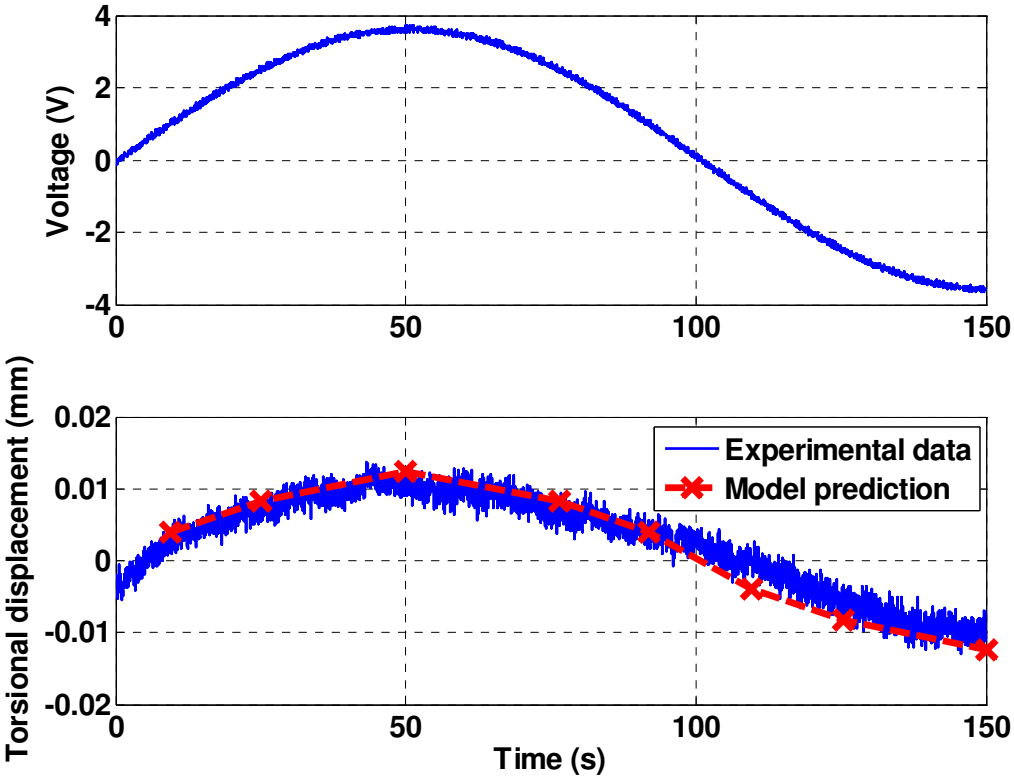

Figure 3.25: The torsional displacement of Sample 2 with 0.005 Hz sinusoidal voltage input.

model prediction is compared with the experimental data, which has verified the effectiveness of the nonlinear elasticity-based model. The performance of actuators with different configurations is compared, which suggests that a configuration with larger radius, thinner tube thickness, and smaller wounding angles will generate larger torsional motion.

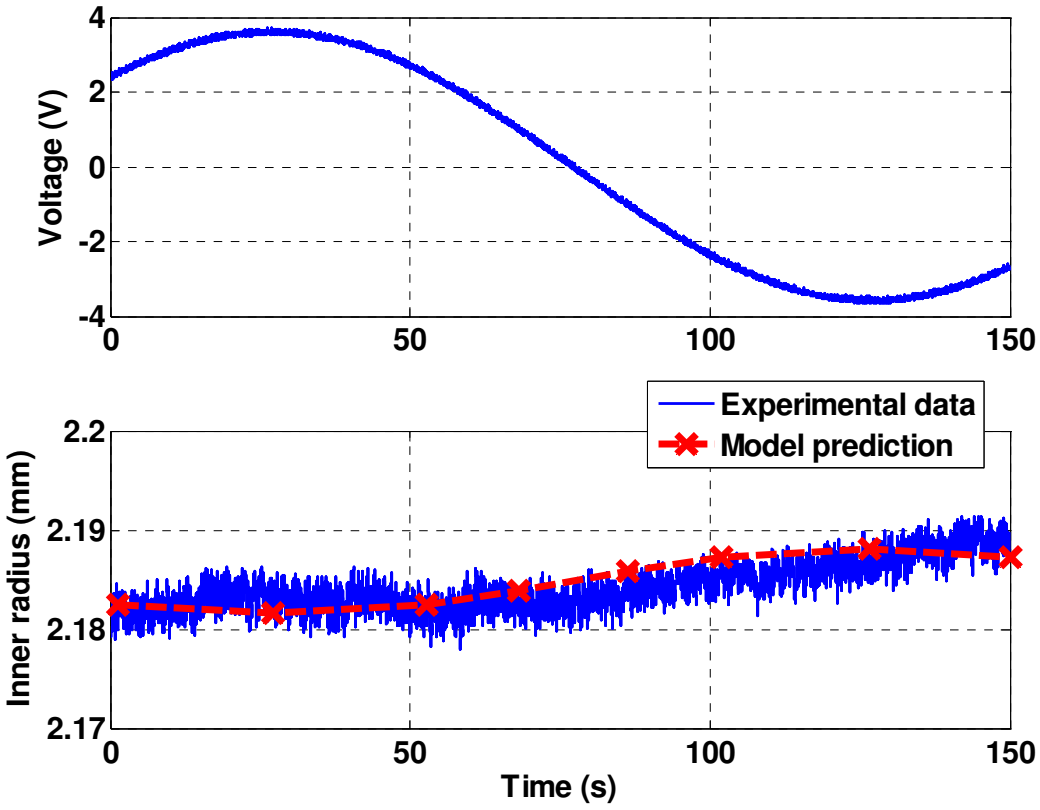

Figure 3.26: The change of inner radius of Sample 2 with 0.005 Hz sinusoidal voltage input.

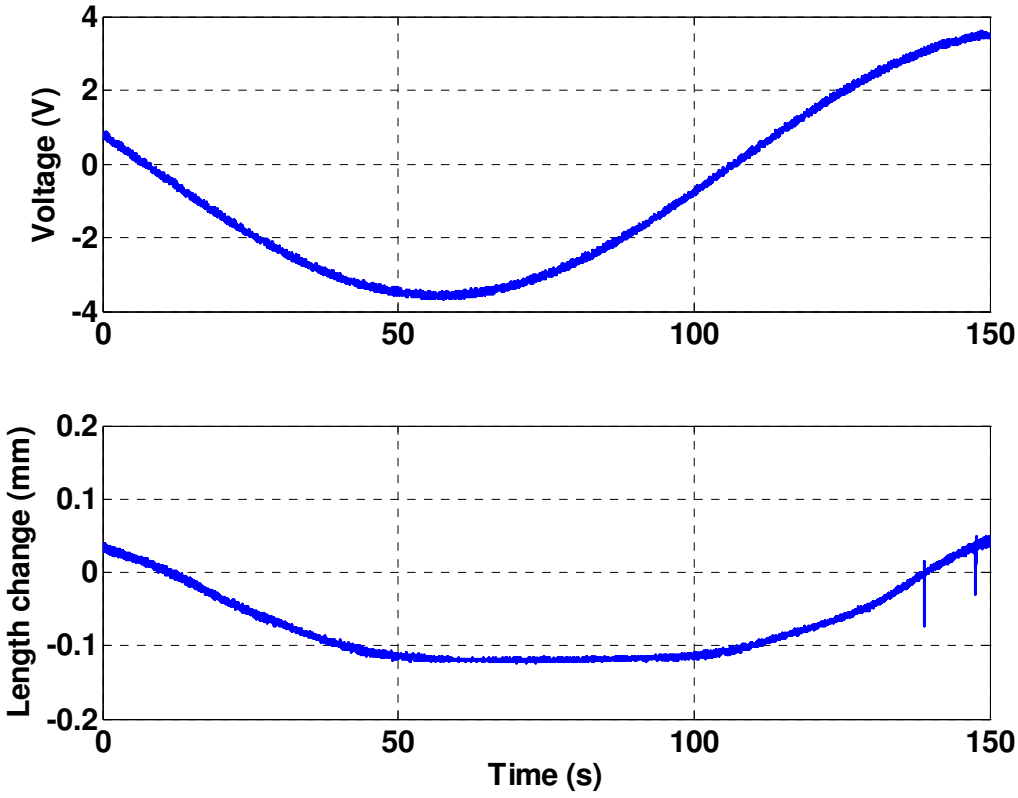

Figure 3.27: The change of tube length of Sample 2 with 0.005 Hz sinusoidal voltage input.

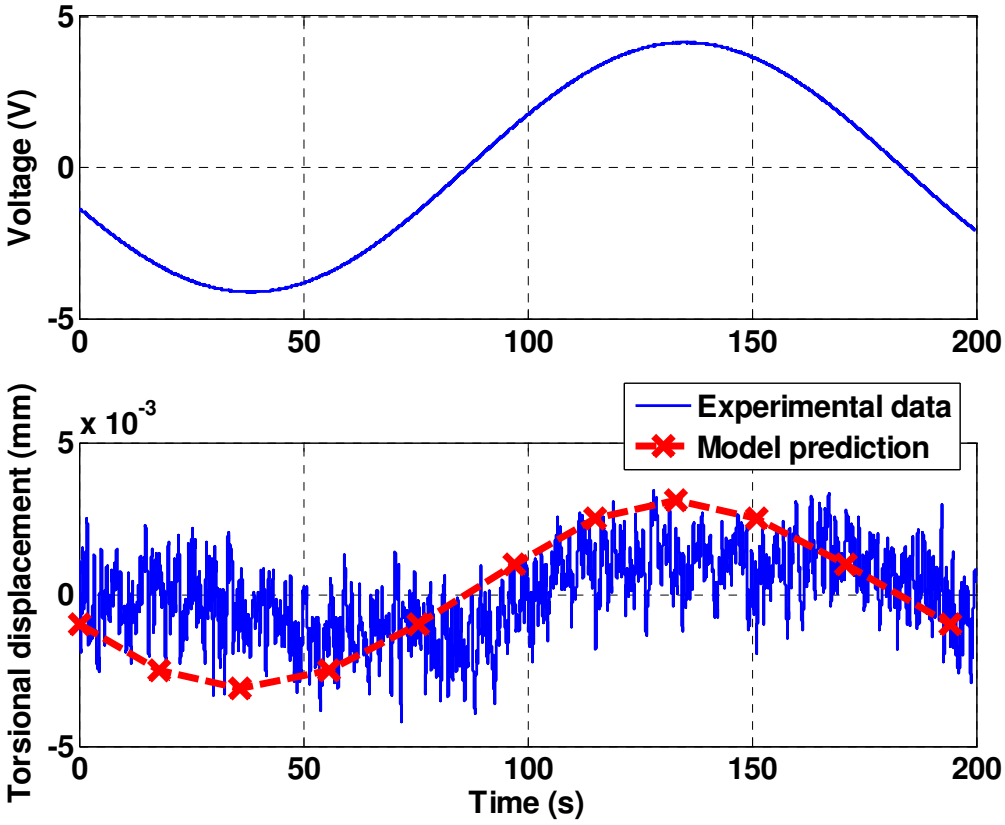

Figure 3.28: The torsional displacement of Sample 3 with 0.005 Hz sinusoidal voltage input.

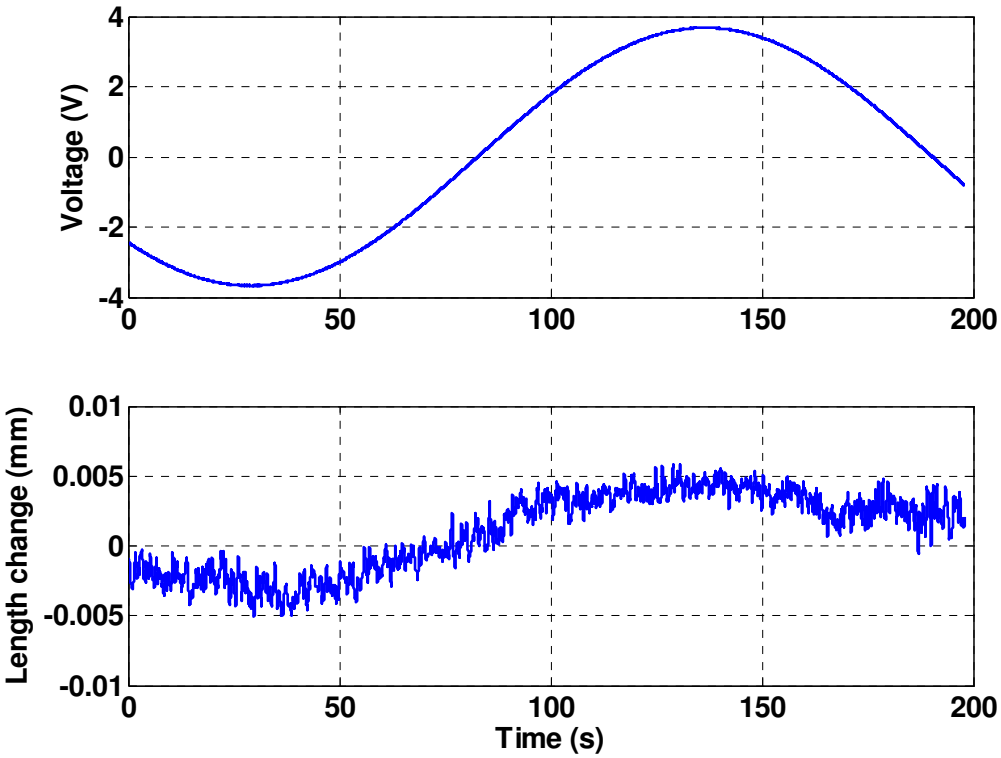

Figure 3.29: The change of tube length of Sample 3 with 0.005 Hz sinusoidal voltage input.

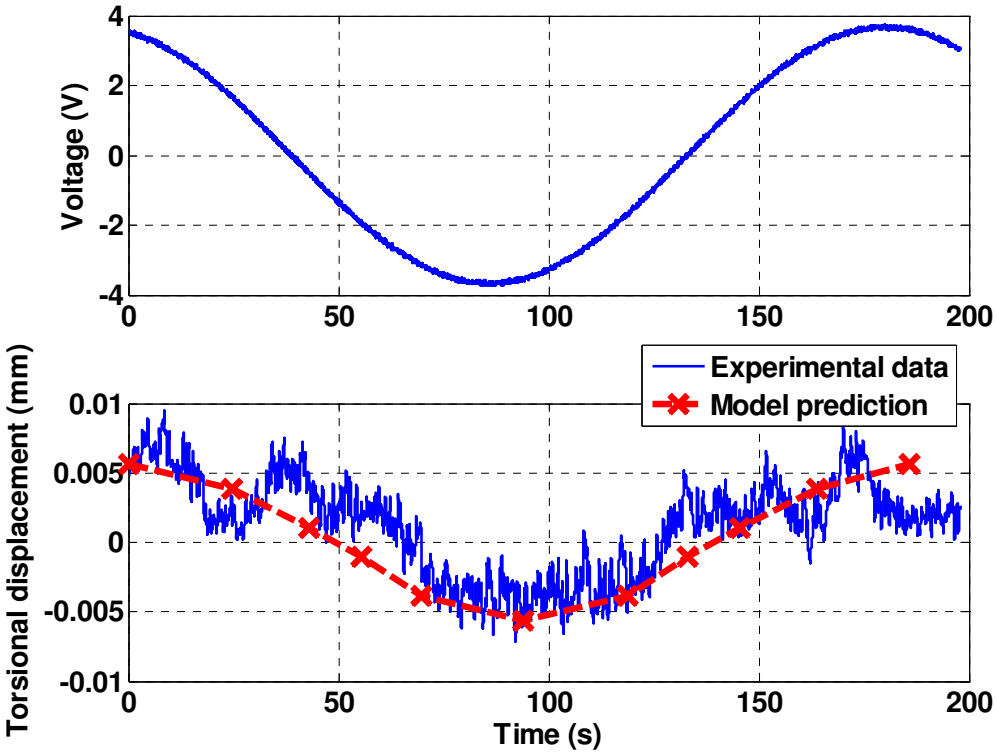

Figure 3.30: The torsional displacement of Sample 4 with 0.005 Hz sinusoidal voltage input.

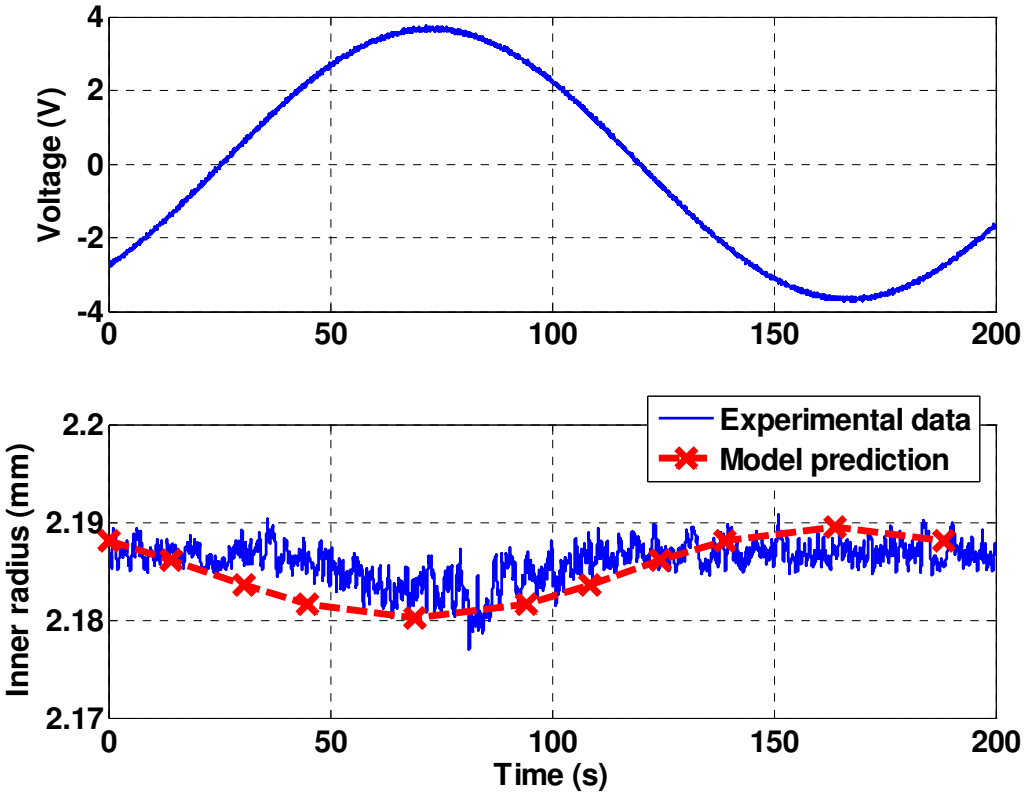

Figure 3.31: The change of inner radius of Sample 4 with 0.005 Hz sinusoidal voltage input.

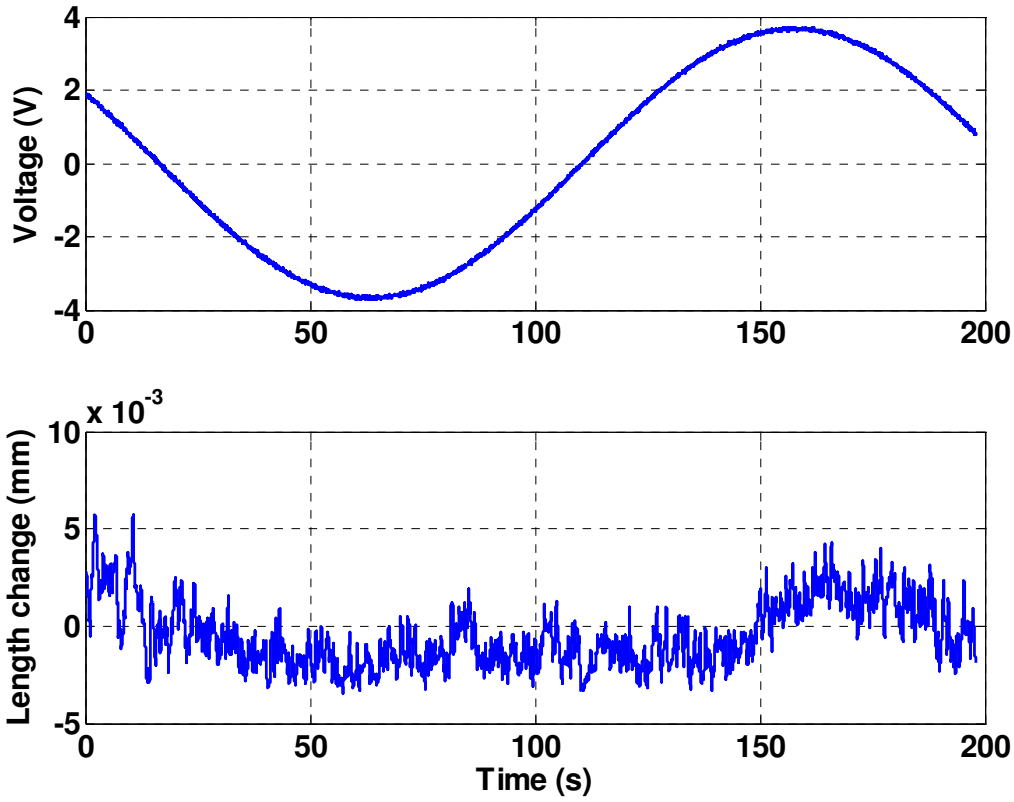

Figure 3.32: The change of tube length of Sample 4 with 0.005 Hz sinusoidal voltage input.

Chapter 4

Control of Conjugated Polymer Actuators

4.1 Model Reduction

The full actuation model (2.30) can be rewritten as

$$\frac{y(s)}{V(s)} = \frac{C_m}{sR + \dfrac{1}{C(1+\dfrac{\sqrt{d}}{\delta\sqrt{s}}\tanh((h_2-h_1)\sqrt{\dfrac{s}{d}}))}}, \tag{4.1}$$

with the constant

$$C_m \triangleq \frac{3\vartheta L[(\frac{h_2}{h_1})^2 - 1]}{8h_1(h_2-h_1)W[(\frac{h_2}{h_1})^3 + \frac{E_{pvdf}}{E_{ppy}} - 1]}.$$

Note that the material dynamics (2.26)is ignored because it is only significant when conjugated polymer is operated at high frequencies. High frequency response becomes too weak to be useful in applications [78]. This can be observed from Fig. 2.17 and 2.18, where the displacement magnitude drops over 20 dB as frequency increases from 0.3 to 30 rad/sec.

Eq. (4.1) is an infinite-dimensional system due to the term $\tanh((h_2-h_1)\sqrt{\frac{s}{d}})$, and

thus is not suitable for real-time control purposes. Utilizing the equality [16]

$$\frac{\tanh(\frac{1}{2}\sqrt{\frac{s}{z}})}{4\sqrt{sz}} = \sum_{n=0}^{\infty} \frac{1}{s+\pi^2(2n+1)^2 z}$$

and letting $z = \dfrac{d}{4(h_2-h_1)^2}$, one converts (4.1) into

$$\frac{y(s)}{V(s)} = \frac{C_m}{sR + \dfrac{1}{C(1+\dfrac{2d}{\delta(h_2-h_1)}\sum_{n=0}^{\infty}\dfrac{1}{s+\pi^2(2n+1)^2 d(2(h_2-h_1))^{-2}})}}. \tag{4.2}$$

To understand the rationale behind model reduction, take typical parameters $d = 2\times 10^{-10}$ m^2/s and $h_2 - h_1 = 30$ μm. The pole of $\dfrac{1}{s+\pi^2(2n+1)^2 d(2(h_2-h_1))^{-2}}$ is at -13.7 for $n = 2$, at -26.9 for $n = 3$, and at -44.4 for $n = 4$, etc. This indicates that one can obtain a low-order approximation to (4.2) by ignoring terms associated with large n. In particular, for a low-frequency input, the approximation will preserve well the behavior of (4.2).

We thus discard terms with $n \geq 2$. This results in the following third-order system for the actuator:

$$\frac{y(s)}{V(s)} = \frac{b_1' s^2 + b_2' s + b_3'}{s^3 + a_1' s^2 + a_2' s + a_3'}, \tag{4.3}$$

where the parameters all have explicit physical meanings:

$$\begin{aligned}
a_1' &= \frac{4D}{(h_2-h_1)\delta}+\frac{5\pi^2 D}{2(h_2-h_1)^2}+\frac{1}{RC},\\
a_2' &= \frac{5\pi^2 D^2}{(h_2-h_1)^3\delta}+\frac{9\pi^4 D^2}{16(h_2-h_1)^4}+\frac{5\pi^2 D}{2(h_2-h_1)^2 RC},\\
a_3' &= \frac{9\pi^4 D^2}{16(h_2-h_1)^4 RC},\\
b_1' &= \frac{C_m}{R},\\
b_2' &= \frac{4DC_m}{(h_2-h_1)\delta R}+\frac{5\pi^2 DC_m}{2(h_2-h_1)^2 R},\\
b_3' &= \frac{5\pi^2 D^2 C_m}{(h_2-h_1)^3\delta R}+\frac{9\pi^4 D^2 C_m}{16(h_2-h_1)^4 R}.
\end{aligned}$$

For typical parameters, (4.3) has one pole and one zero which are located far to the left of the imaginary axis comparing to other poles and zeros, and therefore the model can be further reduced to second order with one zero. This is shown next.

The system (4.3) has three poles with explicit expressions [79]:

$$p_1 = 2\sqrt{-Q}\cos(\frac{\theta}{3})-\frac{1}{3}a_1' \tag{4.4}$$

$$p_2 = 2\sqrt{-Q}\cos(\frac{\theta+2\pi}{3})-\frac{1}{3}a_1', \tag{4.5}$$

$$p_3 = 2\sqrt{-Q}\cos(\frac{\theta+4\pi}{3})-\frac{1}{3}a_1', \tag{4.6}$$

where

$$\begin{aligned}
\theta &= \cos^{-1}(\frac{P}{\sqrt{-Q^3}}),\\
Q &= \frac{3a_2'-a_1'^2}{9},\\
P &= \frac{9a_1'a_2'-27a_3'-2a_1'^3}{54}.
\end{aligned}$$

With typical physical parameters [16], a_1', a_2', and a_3' are all relatively large numbers

($>> 1$). This implies $a_1'^2 >> 3a_2'$ in Q, and $2a_1'^3 >> 9a_1'a_2'$ and $2a_1'^3 >> 27a_3'$ in P, which leads to

$$\begin{aligned} Q &\approx -\frac{a_1'^2}{9},\ P \approx -\frac{a_1'^3}{27}, \\ \sqrt{-Q} &\approx \frac{a_1'}{3}, \\ \theta &\approx \cos^{-1}(-\frac{a_1'^3/27}{\sqrt{a_1'^6/9^3}}) = \cos^{-1}(-1) = \pi. \end{aligned}$$

The poles (4.4) through (4.6) are thus approximately

$$\begin{aligned} p_1 &\approx 2\cdot\frac{a_1'}{3}\cdot\cos(\frac{\pi}{3}) - \frac{a_1'}{3} = 0, \\ p_2 &\approx 2\cdot\frac{a_1'}{3}\cdot\cos(\frac{3\pi}{3}) - \frac{a_1'}{3} = -a_1', \\ p_3 &\approx 2\cdot\frac{a_1'}{3}\cdot\cos(\frac{5\pi}{3}) - \frac{a_1'}{3} = 0. \end{aligned}$$

Clearly $|p_2|$ is very large while $|p_1|$ and $|p_3|$ are relatively small.

The analysis on the zeros is simpler. The zeros of (4.3) are

$$z_1 = \frac{-b_2' - \sqrt{b_2'^2 - 4\cdot b_1'\cdot b_3'}}{2b_1'}, \tag{4.7}$$

$$z_2 = \frac{-b_2' + \sqrt{b_2'^2 - 4\cdot b_1'\cdot b_3'}}{2b_1'}. \tag{4.8}$$

With typical parameters, the following holds:

$$4\cdot b_1'\cdot b_3' \ll b_2'^2,\ b_2 >> b_1,$$

which implies

$$\begin{aligned} z_1 &\approx -\frac{b_2'}{b_1'}, \\ z_2 &\approx 0. \end{aligned}$$

Therefore, $|z_1|$ is very large while $|z_2|$ is relatively small.

A numerical example is provided to illustrate the analysis. Table 4.1 lists the typical values for the relevant physical parameters. The corresponding system parameters for (4.3) are:

$$\begin{aligned} a_1' &= 2.32 \times 10^3, a_2' = 9.79 \times 10^3, a_3' = 3.38 \times 10^3, \\ b_1' &= 0.0667 C_m, b_2' = 71.48 C_m, b_3' = 195.1 C_m, \end{aligned}$$

the three poles are -0.38, -2319, -3.84, and the two zeros are -1069, -2.74.

Table 4.1: Typical values of parameters in the actuation model.

Parameter	Value
D	2×10^{-10} m^2/s
$h_2 - h_1$	30 μm
R	15 Ω
δ	25 nm
C	5.33×10^{-5} F

When operating in air, the trilayer actuator will dry up due to solvent evaporation. This implies that the diffusion coefficient D will decay over time. It is thus of interest to see whether the above analysis on pole/zero locations still holds when D is very small. Fig. 4.1 shows the ratio

$$\frac{\min(|p_2|, |z_1|)}{\max(|p_1|, |p_3|, |z_2|)}$$

as a function of D, while other parameters are chosen as in Table 4.1. It is clear that even when D is close to 0, one can safely ignore one pole and one zero of (4.3) [50]. The final

reduced model for the trilayer actuator thus has the following structure:

$$\frac{y(s)}{V(s)} = \frac{B(s)}{A(s)} = \frac{b_1 s + b_2}{s^2 + a_1 s + a_2}. \tag{4.9}$$

It is expected that despite its simple looking, (4.9) captures the dominant physics of the actuator within the actuation bandwidth. In particular, all parameters of (4.9) can be related to fundamental physical parameters for the full model (2.29).

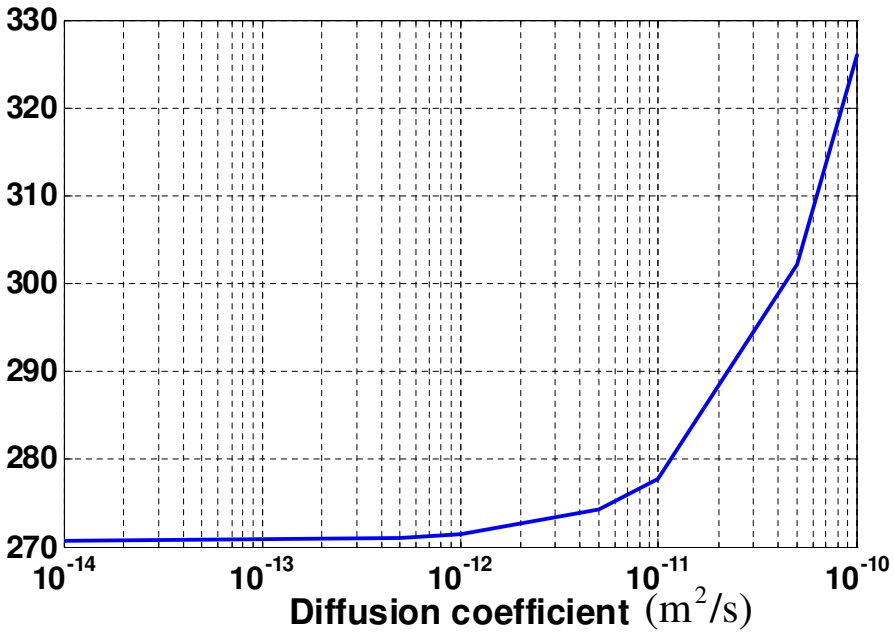

Figure 4.1: Ratio $\dfrac{\min(|p_2|,|z_1|)}{\max(|p_1|,|p_3|,|z_2|)}$ as a function of D.

Fig. 4.2 compares the Bode plot of (4.1) and (4.9) using parameters in Table 4.1. The unmodeled dynamics is bounded in general, and the maximum discrepancy is reached around 10^3 rad/sec. However, considering that the actuator is usually operated in the low frequency range up to a few Hz, the reduced model is a good approximation for control implementation while capturing the main dynamics.

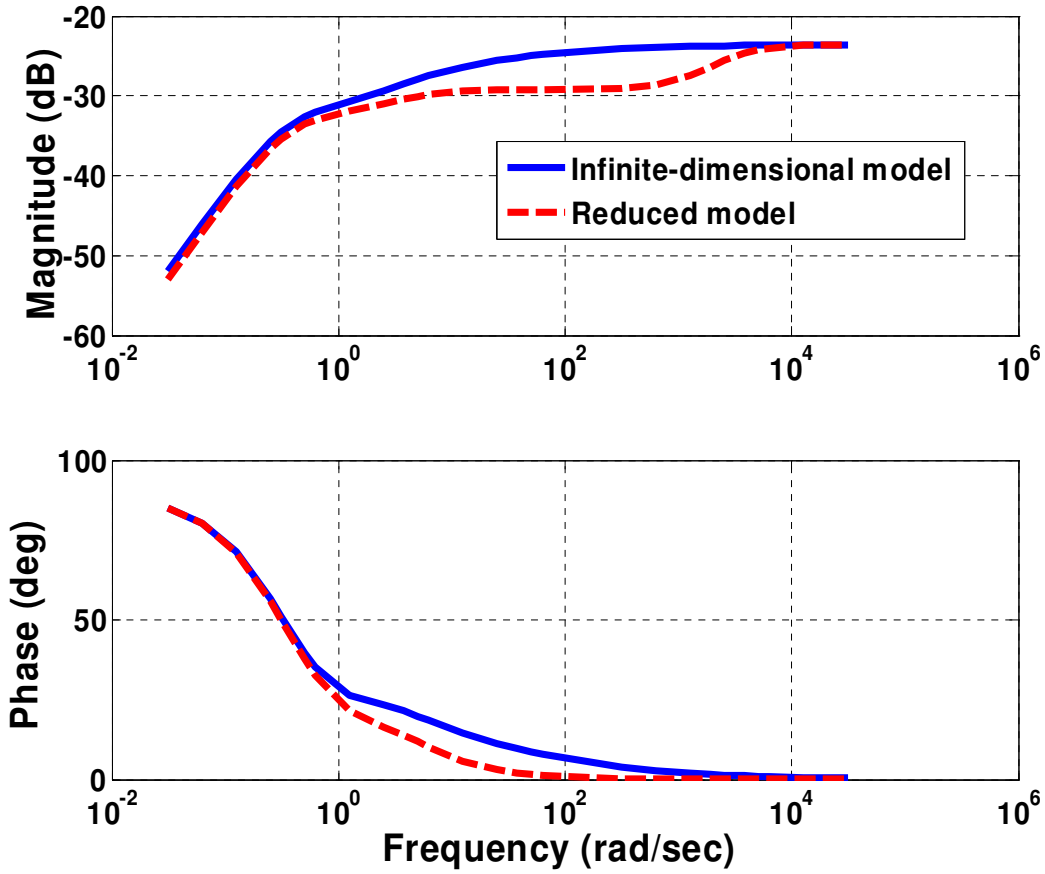

Figure 4.2: Comparisons between the infinite-dimensional and reduced model.

4.2 Design of Robust Adaptive Controller

4.2.1 Self-Tuning Regulator

Controller adaptation is desirable for conjugated polymers since their actuation behaviors can vary significantly over time. Given the model structure (4.9), a self-tuning regulator is adopted due to its simplicity. The idea is to estimate systems parameters online, and then construct a controller based on these estimates so that the closed-loop system would behave like a model system $G_m(s)$ (*model-following*). Fig. 4.3 illustrates the major components of a self-tuning regulator. Note that a low-pass filter is used to filter the noises in the output signal before the output is sent to the self-tuning regulator. The bandwidth is chosen to be 30 Hz to cover the actuation frequency range in experiments.

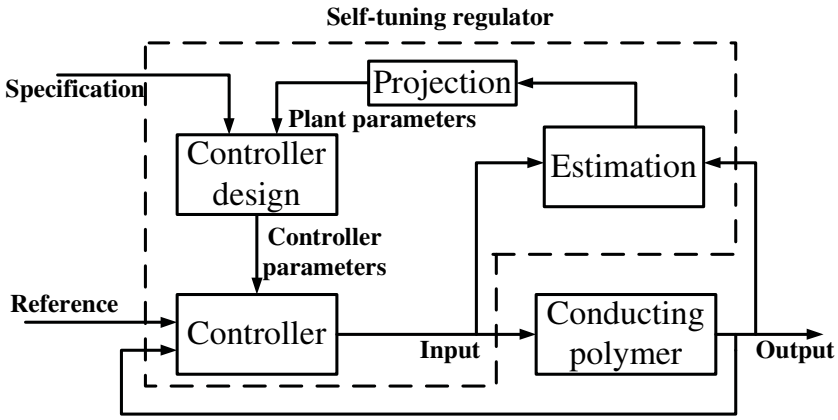

Figure 4.3: Illustration of the robust self-tuning regulator.

In the estimation step, the recursive least-squares algorithm is chosen to identify parameters in (4.9) based on the input into and output from the conducting polymer shown as follows

$$\frac{d\widehat{\theta}}{dt} = P(t)\varphi(t)e(t) \tag{4.10}$$

$$e(t) = y(t) - \varphi^T(t)\widehat{\theta}(t) \tag{4.11}$$

$$\frac{dP(t)}{dt} = \alpha P(t) - P(t)\varphi(t)\varphi^T(t)P(t) \tag{4.12}$$

where

$$\widehat{\theta} = [\hat{a_1} \quad \hat{a_2} \quad \hat{b_1} \quad \hat{b_2}]^T$$

$$\varphi^T(t) = [-\frac{d}{dt}L^{-1}[H_f y(s)] \quad -L^{-1}(H_f y(s)) \quad \frac{d}{dt}L^{-1}[H_f v(s)] \quad L^{-1}(H_f v(s))].$$

A stable transfer function H_f is introduced to avoid direct differentiation of the output signal in estimation

$$H_f = \frac{1}{s^2+2s+1}. \tag{4.13}$$

Note that $L^{-1}[*]$ means inverse Laplace transform.

The desired transfer function is chosen as

$$G(s) = \frac{B_m}{A_m} = \frac{b_{1m}s+b_{2m}}{s^2+a_{1m}s+a_{2m}}. \tag{4.14}$$

A general linear controller is chosen as

$$RV(s) = Tr(s) - Sy(s), \tag{4.15}$$

where *r(s)* is the reference input. R and S are determined by the Diophantine equation

$$AR + BS = A_m \tag{4.16}$$

to track the desired denominator A_m, and B_m is tracked by choosing T. Finally the controller is obtained as

$$V(s) = \frac{b_{1m}s+b_{2m}}{\hat{b}_1 s+\hat{b}_2} r(s) - \frac{(a_{1m}-\hat{a}_1)s+(a_{2m}-\hat{a}_2)}{\hat{b}_1 s+\hat{b}_2} y(s). \tag{4.17}$$

In experiments, the desired transfer function parameters are chosen as

$$a_{1m} = 4, a_{2m} = 4, b_{1m} = 1, b_{2m} = 1.5.$$

4.2.2 Parameter Projection

If the model (4.9) were exact, the controller (4.17) in combination with the online parameter identifier would lead to asymptotic model-following [37]. However, higher-frequency dynamics and nonlinearities are not included in (4.9). Measurement noises are not reflected in the model either. These undesirable factors might lead to instability of the closed-loop system if no proper steps are taken.

In this thesis parameter projection is adopted as a robustification mechanism for the self-tuning regulator. From the expressions of the parameters in (4.3), one knows that the two poles and the zero of (4.9) are all negative, thus the parameters a_1, a_2, b_1, and b_2 should all be positive, which are bounded by a small constant $m > 0$. Furthermore, based on the given polymer parameters and the knowledge of physical parameters, an upper bound $M > 0$ of these parameters can be determined. The update rule (4.10) is thus modified to incorporate parameter projection:

$$\frac{d\hat{\theta}_i(t)}{dt} = \begin{cases} 0 & \text{if } \hat{\theta}_i(t) = M \text{ and } [P(t)\varphi(t)e(t)]_i > 0 \\ 0 & \text{if } \hat{\theta}_i(t) = m \text{ and } [P(t)\varphi(t)e(t)]_i < 0 \\ [P(t)\varphi(t)e(t)]_i & \text{otherwise} \end{cases}, \tag{4.18}$$

where $\hat{\theta}_i(t)$ and $[P(t)\varphi(t)e(t)]_i$ denote the i-th components of $\hat{\theta}$ and $P(t)\varphi(t)e(t)$, respectively. Clearly, if $\hat{\theta}_i(0) \in [m,M]$, $\hat{\theta}_i(t) \in [m,M]$, $\forall t > 0$. In the experiments the values of M and m are chosen to be $M = 1 \times 10^4$, $m = 0.001$.

One can represent the true output $y(s)$ of the actuator under the input $V(s)$ as

$$y(s) = \frac{b_1 s + b_2}{s^2 + a_1 s + a_2} V(s) + \Delta(s)V(s) + \mathscr{N}[V(s)] + w(s). \tag{4.19}$$

Here $\Delta(s)$ represents the unmodeled higher-frequency dynamics, i.e., the difference between (4.1) and (4.9). Since both (4.1) and (4.9) are stable and have bounded frequency responses, $\Delta(s)$ will be stable and bounded. $\mathscr{N}[V(s)]$ denotes the influence of unmodeled

nonlinearity (e.g., hysteresis). The nonlinearities will be bounded due to the dissipative nature of the materials. In (4.19), $w(s)$ denotes the measurement noise, which is also bounded.

It can be shown [80, 81] that the proposed adaptive control scheme in Section 4.2.1 with parameter projection (4.18) is robust in the presence of bounded unmodeled dynamics and nonlinearities, measurement noise, and slow and bounded parameter variations; in particular, all signals in the closed-loop system will be bounded.

4.3 Experimental Results

4.3.1 Measurement Setup

Tracking experiments are conducted to examine the effectiveness of the proposed robust adaptive control scheme. A trilayer polypyrrole actuator ($20 \times 5 \times 0.17$ mm) is clamped at one end, where the actuation voltage is applied. The tip displacement is measured by an OADM 20I6441/S14F laser sensor from Baumer Electric Inc. with resolution of 5 μm. The controller is implemented in a PC equipped with dSPACE DS1104. The experimental setup is shown in Fig. 4.4. Before each experiment, an actuator cut with the specified size is soaked in the electrolyte ($TBA^+PF_6^-$ in propylene carbonate). The inner porous PVDF layer thus stores electrolyte, which enables the actuator to operate in air for some time. The time of continuous in-air operation depends on how fast the stored solvent evaporates, and without further packaging, it is about 4-5 hours. The experimental temperature and humidity are maintained as 25°C and 27% respectively. For practical applications, the packaging issue will have to be solved so that the actuator can work in air for much longer time. On the other hand, the current actuator demonstrates significant time-varying behavior, which provides a good testbed for verifying the proposed adaptive scheme.

For comparison purposes, a PID controller and a fixed model-following controller are also implemented. Actuators with same dimensions and same conditions are used for all

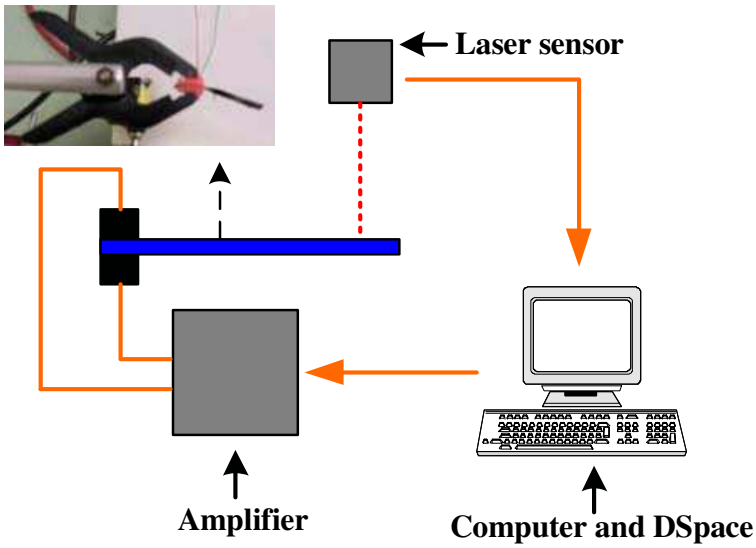

Figure 4.4: Schematic of the experimental setup.

three controllers. The design of the PID controller and that of the model-following controller are also based on the model structure (4.9), while the model parameters are identified in separate experiments shortly before the tracking experiment starts. The model-following controller is constructed as in (4.17), except that the controller parameters will not be updated. The PID gains are carefully tuned and verified in Matlab simulation before the experiments to ensure that the initial tracking errors are within the similar range as those under other controllers, and the PID controller is

$$\frac{U}{E} = 6 + \frac{6}{s} + 0.02s. \tag{4.20}$$

For each continuous tracking experiment (3-4 hours long), the parameters of the PID controller and the model-following controller remain constant (i.e., non-adapting). Throughout the experiments, the reference model $G_m(s)$ is chosen to be

$$G_m(s) = \frac{s+1.5}{s^2+4s+4}.$$

4.3.2 Results and Discussions

In the first batch of experiments (Batch One), the reference input $r(t) = 0.5\sin(\pi t) + 0.5\sin(0.2\pi t)$V, and the actuator output $y(t)$ is required to track the desired trajectory $y_m(t) = G_m(s)[r(\cdot)](t)$. The latter contains two frequency components (0.1 Hz and 0.5 Hz) with peak-to-peak variation of 0.62 mm. Each experiment runs continuously for four hours. Fig. 4.5 shows the tracking results at the beginning of the experiment ($t = 0$ h), while Fig. 4.6 shows the results when approaching the end of the experiment ($t = 4$ h).

To better compare the control schemes, two metrics are defined for the tracking error. Given a starting time t_0 and a constant $T > 0$, we define the *normalized average error* e_a

$$e_a \triangleq \frac{\int_{t_0}^{t_0+T} |y(t) - y_m(t)|dt}{\int_{t_0}^{t_0+T} |y_m(t)|dt}, \tag{4.21}$$

and the *normalized maximum error* e_m

$$e_m \triangleq \frac{\max_{t\in[t_0,t_0+T]} |y(t) - y_m(t)|}{\max_{t\in[t_0,t_0+T]} |y_m(t)|}. \tag{4.22}$$

Throughout this thesis, T is chosen to be 100 s. Under the robust adaptive scheme, e_a drops from 11% at $t_0 = 0$ h to 7% at $t = 4$ h, and e_m drops from 15% to 9% for the same period. In comparison, e_a increases from 7% to 28% under the PID controller, from 7% to 50% under the fixed model-following controller, and e_m increases from 8% to 25% under the PID scheme, and from 10% to 48% under the model-following scheme. Fig. 4.7 shows the evolution of e_a and e_m, measured and calculated every half a hour, under the three schemes. It is clear that the robust adaptive control scheme delivers consistent tracking performance during the four-hour continuous operation, while the tracking performance under the PID scheme or the fixed model-following scheme deteriorates over time.

A second batch of experiments (Batch Two) is conducted to examine the effectiveness of the three schemes in tracking trajectories of much larger magnitude. With the reference

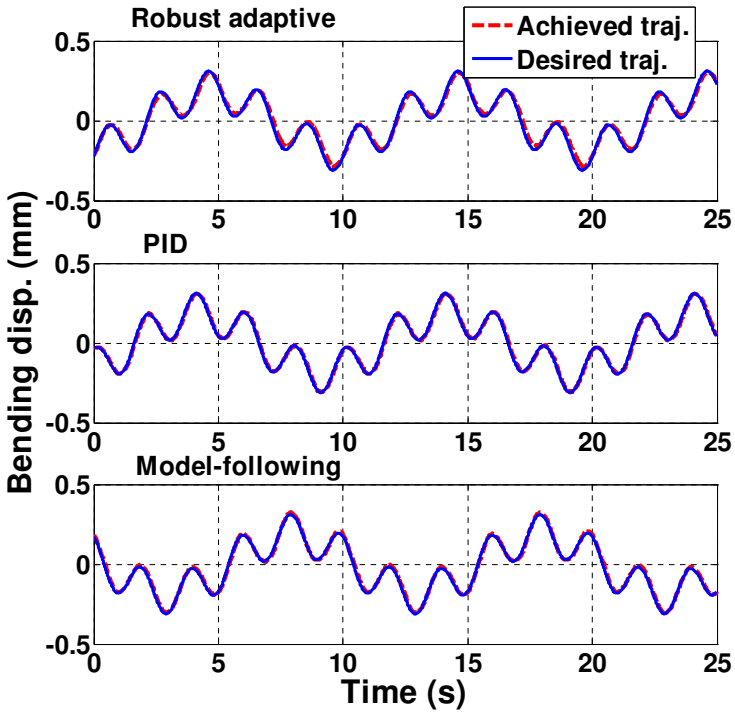

(a)

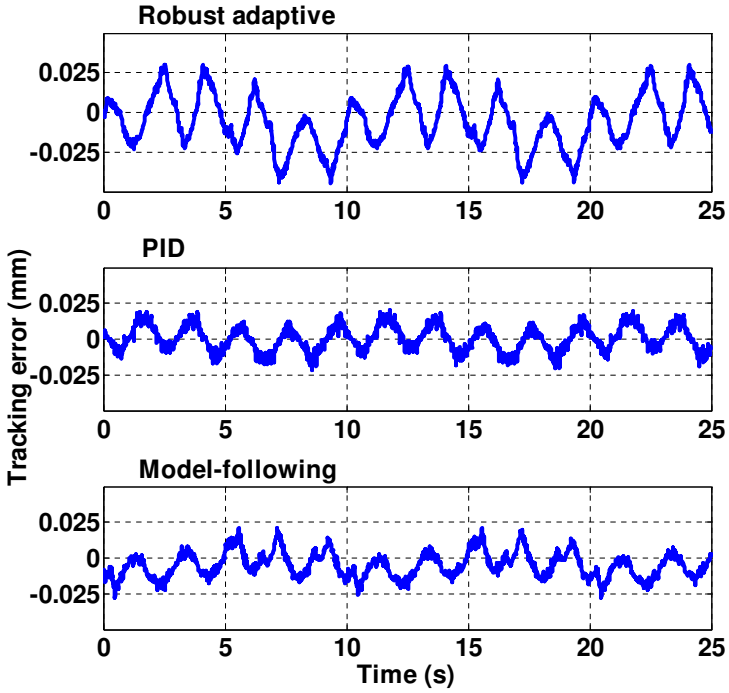

(b)

Figure 4.5: Experimental results on trajectory tracking (Batch One), $t = 0$ h. (a) Achieved trajectories versus desired one under the three controllers; (b) instantaneous tracking errors under the three schemes.

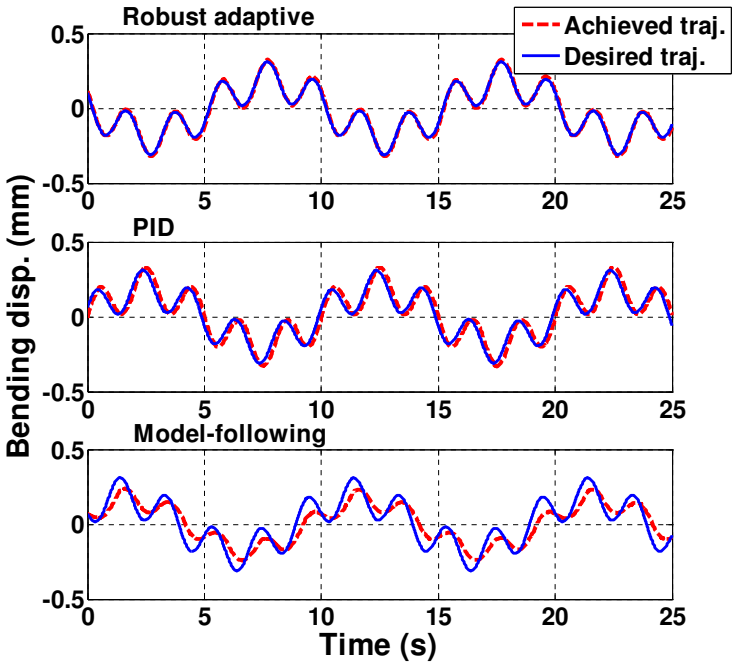

(a)

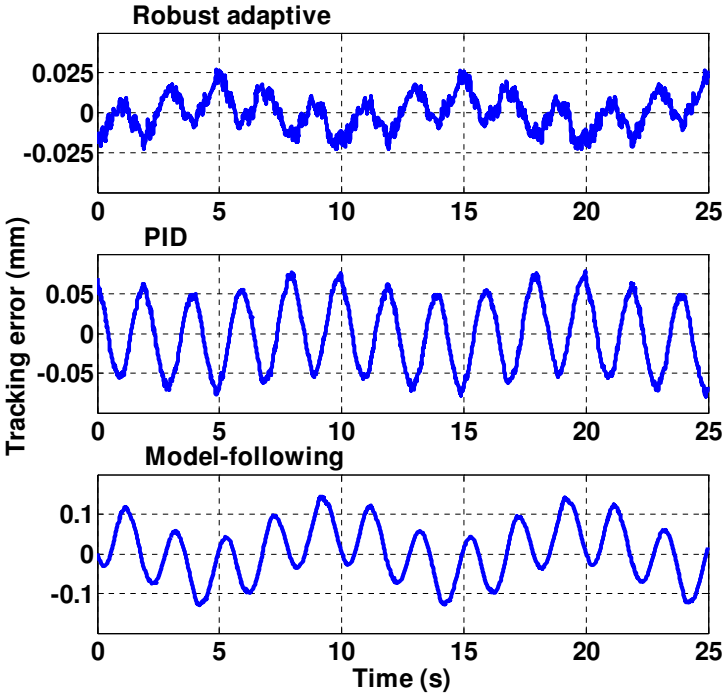

(b)

Figure 4.6: Experimental results on trajectory tracking (Batch One), $t = 4$ h. (a) Achieved trajectories versus desired one under the three controllers; (b) instantaneous tracking errors under the three schemes (note the different vertical-axis scales).

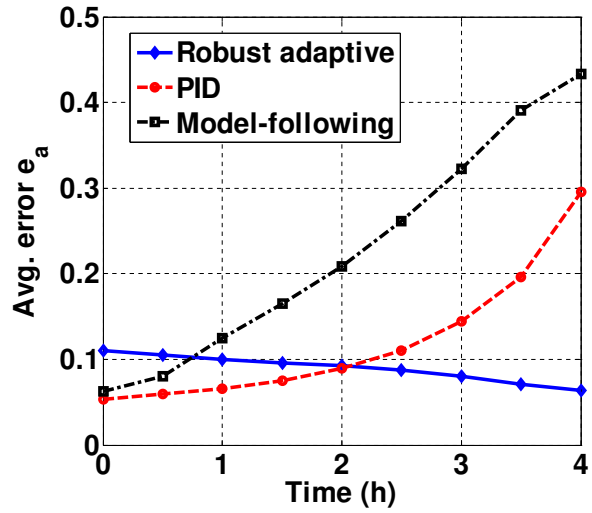

(a)

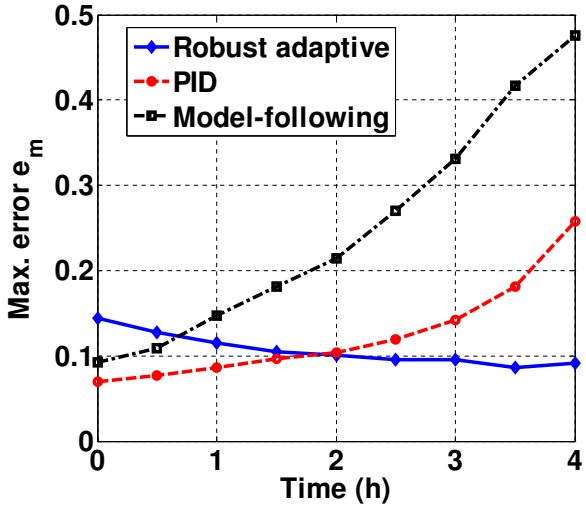

(b)

Figure 4.7: Normalized average error e_a and maximum error e_m under the three control schemes (Batch One experiments). (a) Evolution of e_a; (b) evolution of e_m.

input $r(t) = 2.1\sin(0.4\pi t) + 2.2\sin(0.1\pi t)$V, the desired trajectory $y_m(t)$ has peak-to-peak variation of 3 mm. All three schemes show good tracking performance at the beginning. The experiment under PID control has to be stopped after 3 hours since at that time the voltage input exceeds the limit (1.6 V). Fig. 4.8 shows the tracking results when $t = 3$ h. Fig. 4.9 shows the evolution of e_a and e_m. The trend is consistent with that in Batch One experiments. It can be seen that the robust adaptive controller keeps e_a under 3.5% and e_m under 4% throughout the four-hour experiment. In the mean time e_a rises from 5.5% to 8.4%, e_m from 5.7% to 10%, under the PID controller (in three hours), and e_a rises from 5% to 80%, e_m from 5.5% to 81%, under the fixed model-following controller (in four hours).

It is also important to compare the control efforts required under the different control schemes. Low control effort is highly desirable since that leads to long working life for the conjugated polymer actuator. Fig. 4.10 shows the evolution of the magnitude of voltage input under each scheme, for both Batch One and Batch Two experiments. The required voltage increases over time under every scheme, which is due to the deteriorating actuation capability of the actuator as the solvent evaporates. However, it can be clearly seen that the voltage input under the adaptive scheme is much lower than that under the PID scheme, and also lower than that under the model-following scheme most of the time. In the Batch Two/PID experiment, the polymer actuator was actually damaged and stopped functioning after 3 hours due to continuous high-voltage (> 1.5 V) actuation.

There is another interesting observation during the experiments that supports the validity of the reduced model. The effect of solvent evaporation can be incorporated by taking the diffusion coefficient $D \to 0$. This leads to $p_1 \to 0$, $p_3 \to 0$, and $z_2 \to 0$, where p_1, p_3, and z_2 are the poles and the zero of the reduced model (5.2), as defined by (4.4), (4.6), and (4.8). Fig. 4.11 (a) shows the evolution of the poles and the zero during the Batch One experiment every half an hour when the adaptive control scheme is adopted. Fig. 4.11 (b) shows this evolution during 100 seconds after the experiment started for half an hour. It can be seen that the poles and zero all tend to 0, as predicted by the model.

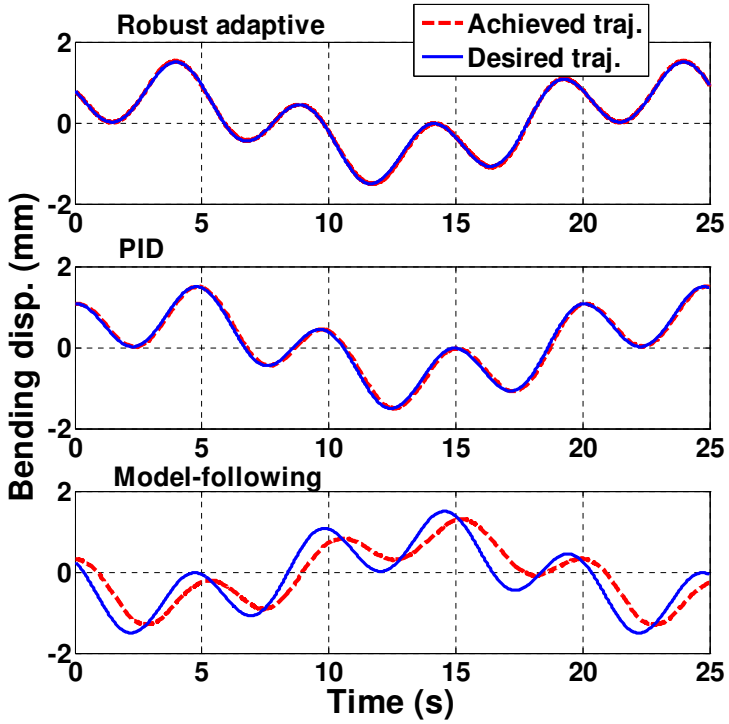

(a)

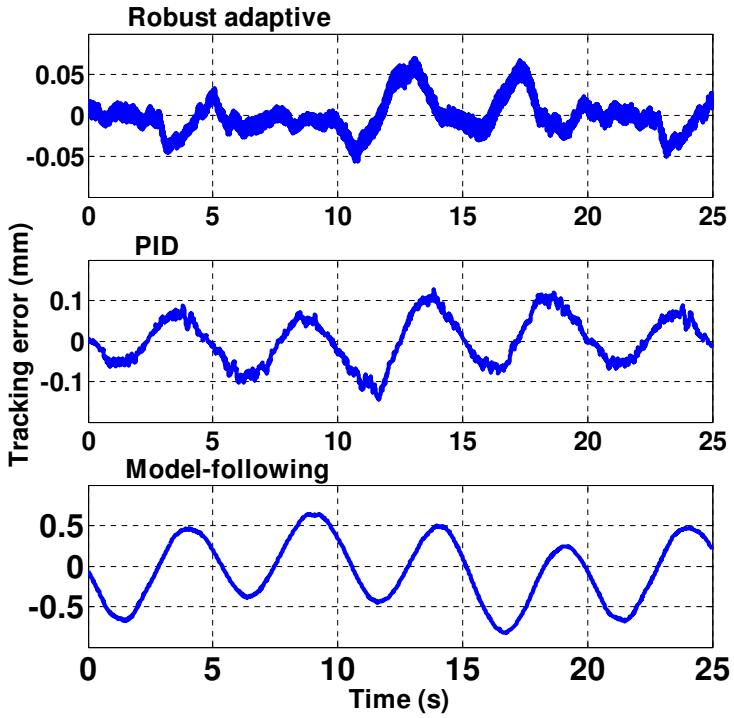

(b)

Figure 4.8: Experimental results on trajectory tracking (Batch Two), $t = 3$ h. (a) Achieved trajectories versus desired one under the three controllers; (b) instantaneous tracking errors under the three schemes.

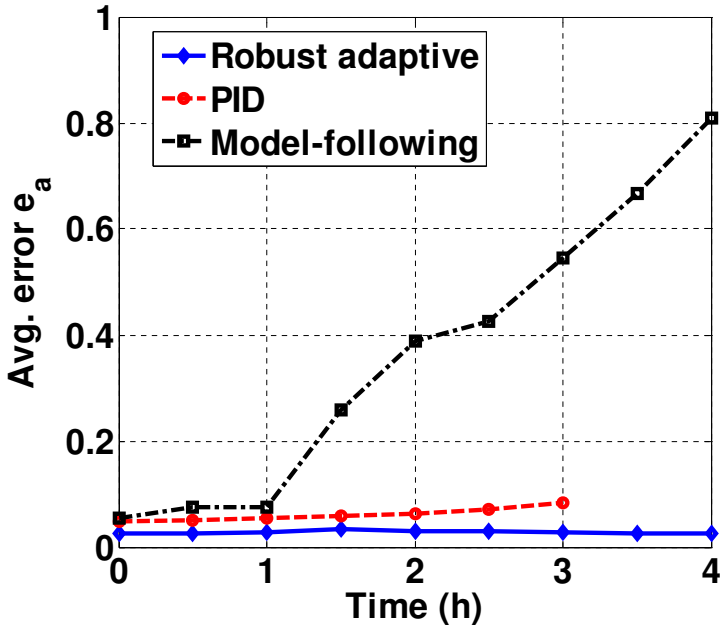

(a)

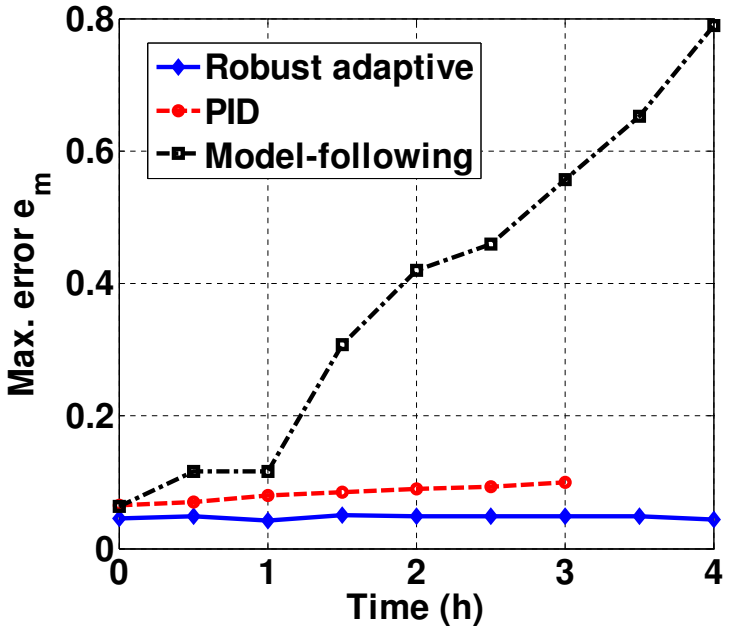

(b)

Figure 4.9: Normalized average error e_a and maximum error e_m under the three control schemes (Batch Two experiments). (a) Evolution of e_a; (b) evolution of e_m.

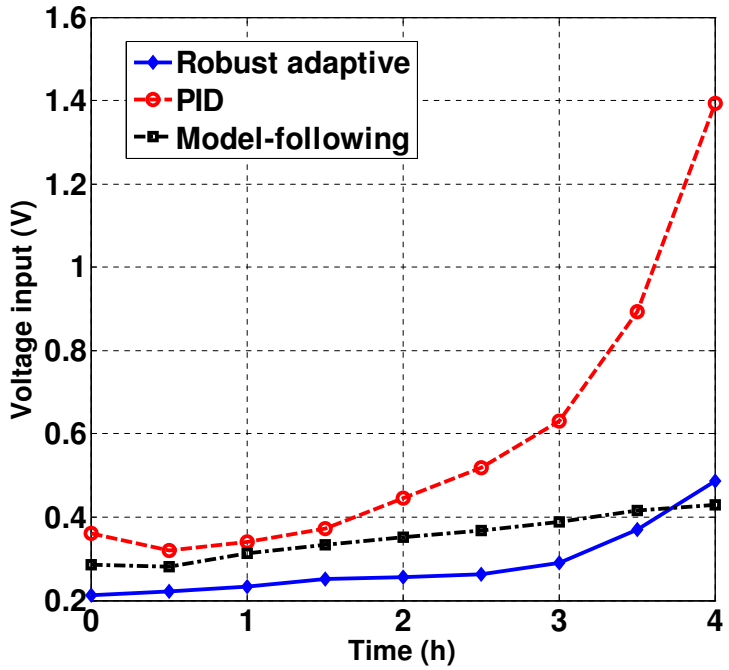

(a)

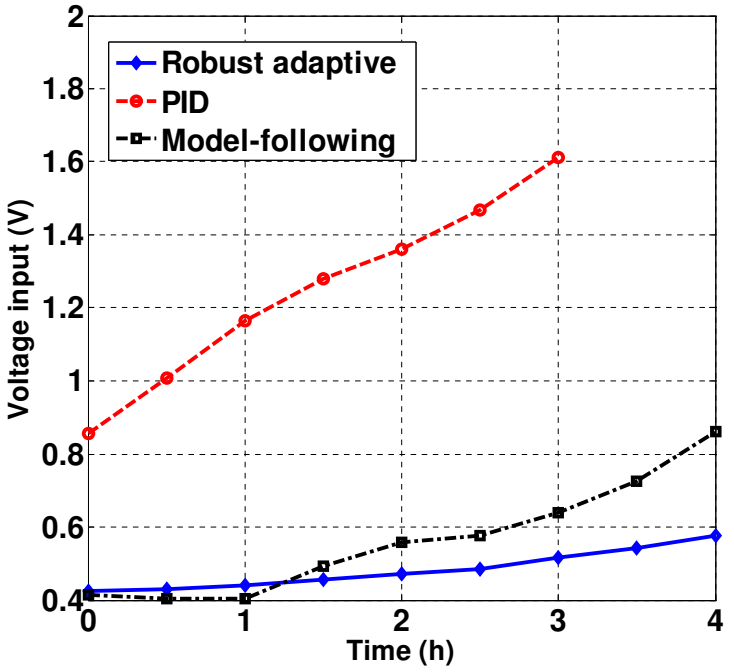

(b)

Figure 4.10: Evolution of voltage input magnitude under the three schemes. (a) Batch One experiments; (b) Batch Two experiments.

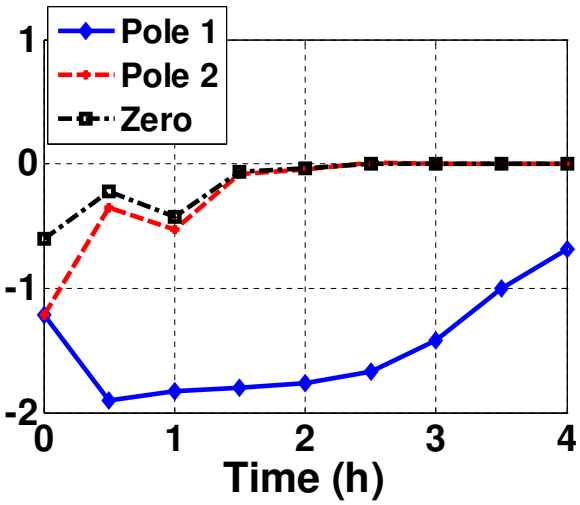

(a)

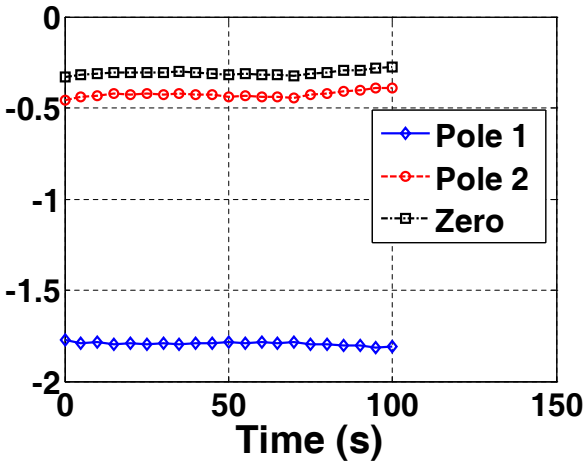

(b)

Figure 4.11: Identified poles and zero under the robust adaptive control scheme in Batch One experiment. (a) Evolution over four hours; (b) Evolution over 100 seconds.

In both Batch One and Batch Two experiments, the reference inputs used contain two frequency components and are thus persistently exciting of order 4 [37]. This is a necessary and sufficient condition for correctly identifying the four parameters in (4.9). In practice, however, the persistent excitation condition may not always hold, and it is of interest to know whether the robust adaptive scheme still works well in that case. An experiment is conducted for this purpose, where the reference input $r(t) = 2\sin(\pi t)$ is persistently exciting of order 2. Fig. 4.12 shows the tracking results under the robust adaptive controller, at the beginning and the end of four-hour continuous operation, which demonstrates the capability of the proposed scheme in tracking a non-persistently exciting signal.

4.4 Chapter Summary

A robust adaptive control scheme has been presented for conjugated polymer actuators. The key to the success of this method is a simple actuator model that is reduced from the full, infinite-dimensional physical model. Model reduction is based on the knowledge of the actuation bandwidth as well as typical values of the physical parameters. The reduced model captures relevant actuation physics and it makes the control design and implementation easy. Note that the physical-based model provides justification of the specific controller structure. This is in contrast to pure empirical models obtained through system identification, which requires re-identification for different samples. The parameter projection step in the self-tuning regulator ensures the stability of the closed-loop system in the presence of noises and unmodeled dynamics. Experimental results have shown that the proposed scheme is superior to the commonly used PID scheme and to the fixed model-following scheme in terms of both tracking accuracy and required control effort.

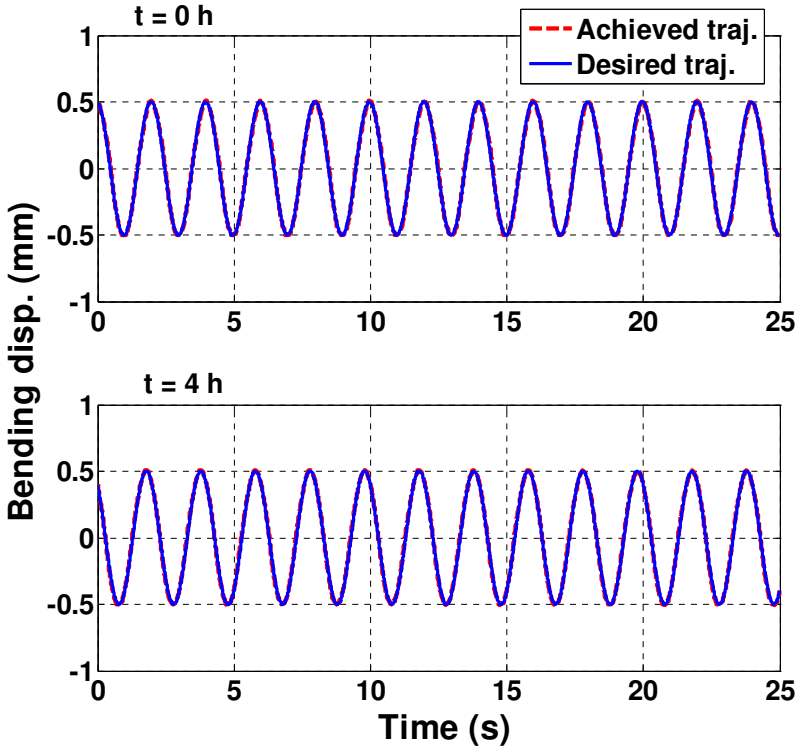

(a)

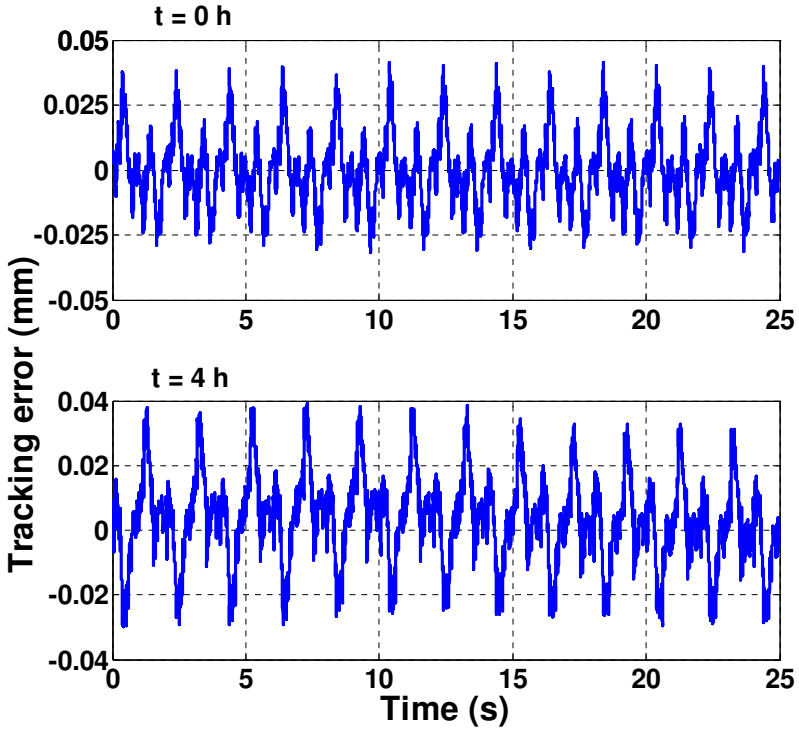

(b)

Figure 4.12: Experimental results of tracking a non-persistently exciting signal under the robust adaptive controller. (a) Trajectory tracking at $t = 0$ h and $t = 4$ h; (b) Tracking errors at $t = 0$ h and $t = 4$ h.

Chapter 5

Application: Conjugated Polymer Micropump

5.1 Design and Fabrication of the Micropump

5.1.1 Diaphragm Design

In a typical design of EAP-based pumping diaphragm, one uses a single EAP plate as the diaphragm to seal the pump chamber directly. The edge of the plate is mechanically fixed with electrodes on both sides. However, the strain of the middle-plane will be nonzero due to the restriction at the edge, which implies that a significant portion of energy will be required to stretch the middle-plane. The latter constrains the displacement of the diaphragm in the vertical direction. Detailed analysis will be shown in Section 5.2.

A new design is thus proposed here for the generation of large out-of-plane deformation, as illustrated in Fig. 5.1. A passive membrane with low stiffness is used to seal the chamber. Then a conjugated polymer plate is cut into the shape of petals and bonded to this passive layer. When the voltage is applied, the conjugated polymer petals will bend together to move the elastic diaphragm and generate pressure changes inside the chamber.

Therefore, it is the passive layer instead of the conjugated polymer that is being stretched, and one can choose a passive layer material with low Young's modulus to significantly reduce the energy required to stretch the middle-plane.

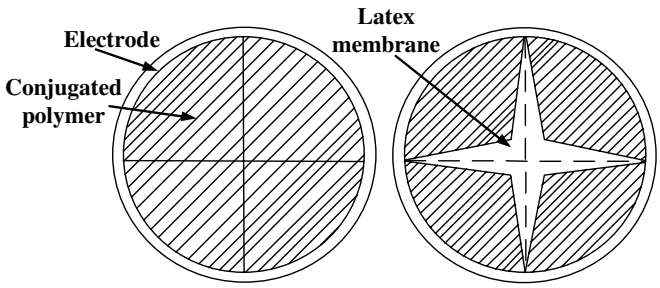

Figure 5.1: Schematic of a petal-shape pumping diaphragm (top view). Left: before actuation; right: upon actuation.

5.1.2 Fabrication and Assembly of the Micropump

Fabrication of the trilayer conjugated polymer is achieved by electrochemically oxidizing pyrrole monomer from a solution to grow PPy layers on either side of a gold-coated porous PVDF film, by following the similar recipe in [82]. Polydimethylsiloxane (PDMS) is chosen as the material for fabricating the micropump. It is an elastomeric polymer that is much more compliant than silicon or glass, and it is becoming popular for microfluidic devices. The Young's modulus of PDMS varies between 360-870 KPa [83]. Other attractive features of PDMS include biocompatibility, low cost, and transparent view (which makes it easy to monitor the fluid flow). The PDMS material is composed of two parts, a curing agent and the polymer. They are mixed by a certain volume ratio and allowed to cure under a certain temperature. Therefore, once the micro patterns are fabricated, the inverse patterns of PDMS can be obtained by applying PDMS on the substrate and peeling it off after it is cured. SU-8 2150 photoresist is exposed with conventional UV (350-400 nm) radiation to make micro patterns on a silicon substrate.

By utilizing the microfabrication method involving PDMS and SU-8, different functional layers of the pump can be fabricated and eventually assembled together. The assembly schematic is shown in Fig. 5.2. Notice that there are four alignment holes at the corners of PDMS layers for the ease of final assembly. The conjugated polymer actuator will be positioned at the top of the pump chamber and attached to the PDMS membrane by applying uncured PDMS as glue.

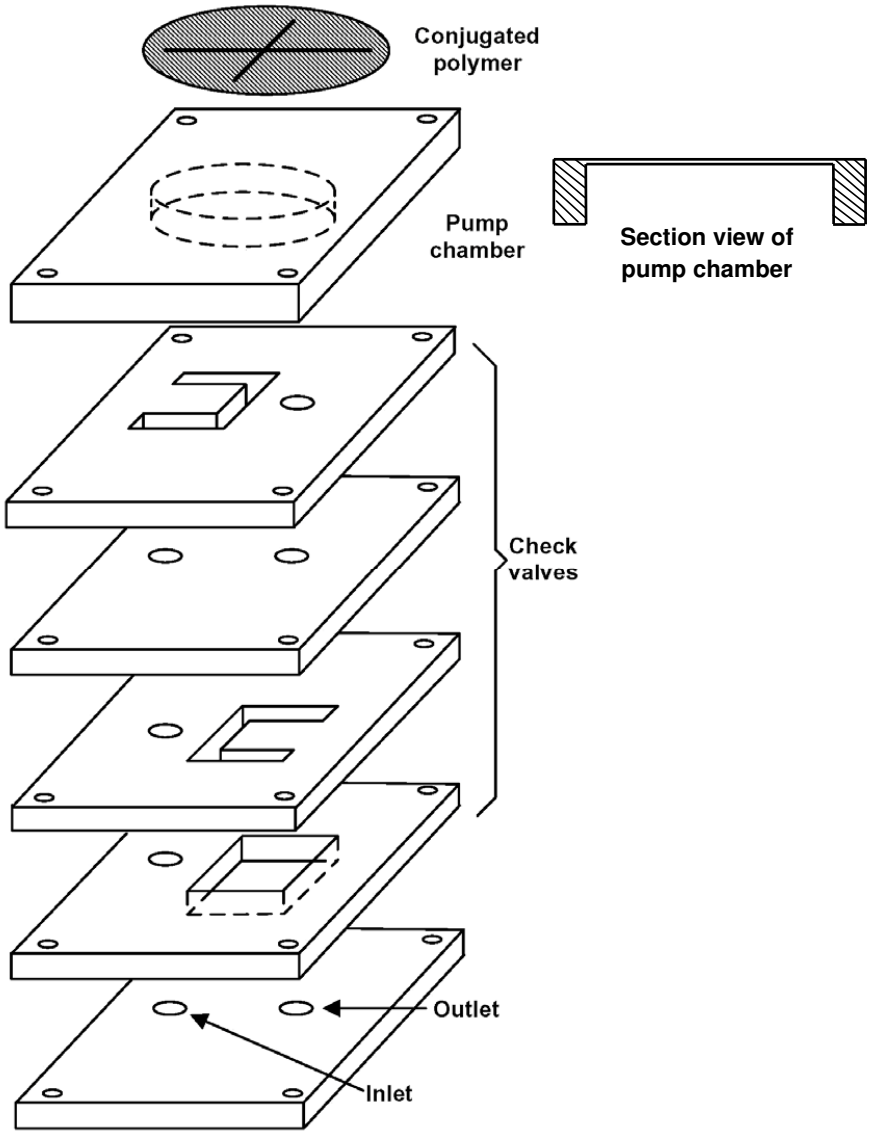

Figure 5.2: The assembly schematic of micropump.

Flap valves are chosen to keep the directional flow because of their ease of fabrication and high efficiency to regulate the fluid flow. The mechanism of a flap valve is illustrated in Fig. 5.3. The end of each flap is attached to the middle layer, which has two channels covered by the flaps. When a pressure is applied from the top, the flap on the right will be pushed down and allow the fluid to flow downwards. When a pressure is applied from the bottom, the flap on the left will be lifted up, and the fluid will flow upwards.

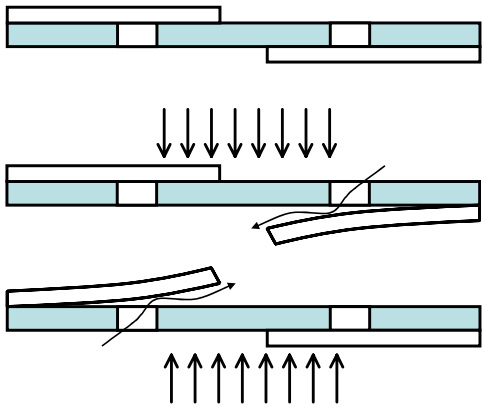

Figure 5.3: The mechanism of flap check valves.

The microfabrication process to make the flap valve layer is shown in Fig. 5.4. Firstly an SU-8 layer is spun on the silicon substrate. Then a photo mask is used to pattern the SU-8 through photolithography. After SU-8 is developed and forms the desired pattern, PDMS is spun on the SU-8 pattern and baked in oven to cure. Finally the PDMS layer is peeled off from the substrate for assembly. Other functional layers can be fabricated in the same way.

The assembled micropump is shown in Fig. 5.6. The structure of the micropump can be observed in the magnified view shown in Fig. 5.6. The size of the pump is 25×25 mm (top view) and 10 mm (height). The diameter of the diaphragm is 19 mm. The depth of the pump chamber is 9.8 mm. The micro channels have the diameter of 1 mm. The check valve flapper is 1 mm thick, 3 mm wide, and 5 mm long.

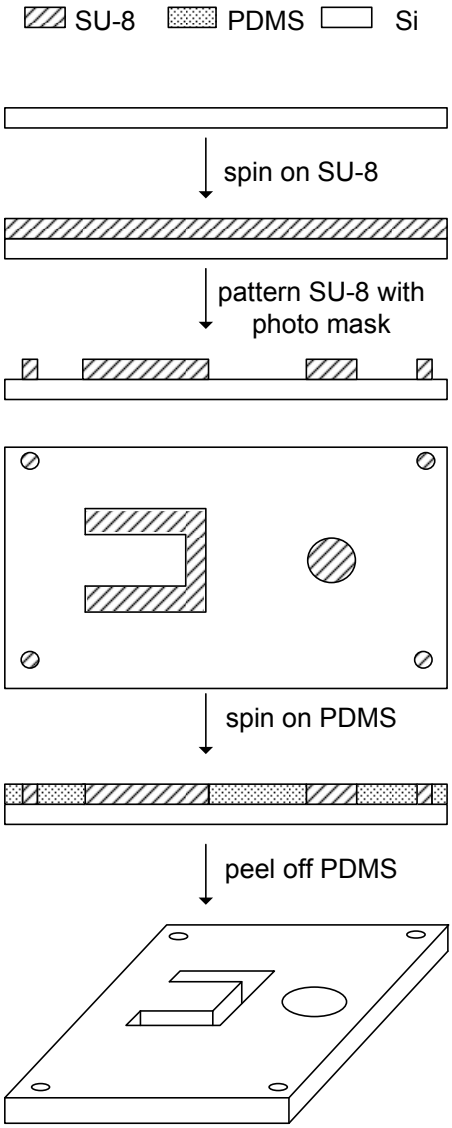

Figure 5.4: The microfabrication process to make a flap valve.

5.2 Physics-based, Control-oriented Model for the Pump

Because PPy has sophisticated electrochemomechanical dynamics that can vary significantly over time [6], a model that captures the complicated dynamics yet amenable to control design is important for applying advanced control algorithms to deliver accurate and consistent flow rates for different applications. As shown in Fig. 5.7, the developed model in this thesis consists of three cascaded modules: 1) the electrical admittance module of

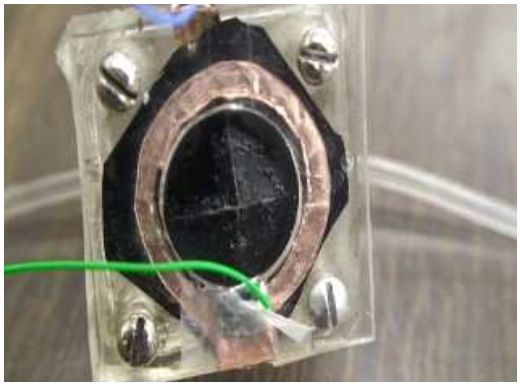

(a)

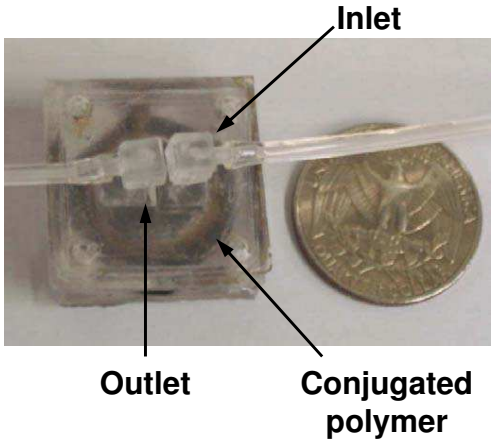

(b)

Figure 5.5: (a) The assembled micropump (top view); (b) The assembled micropump (bottom view).

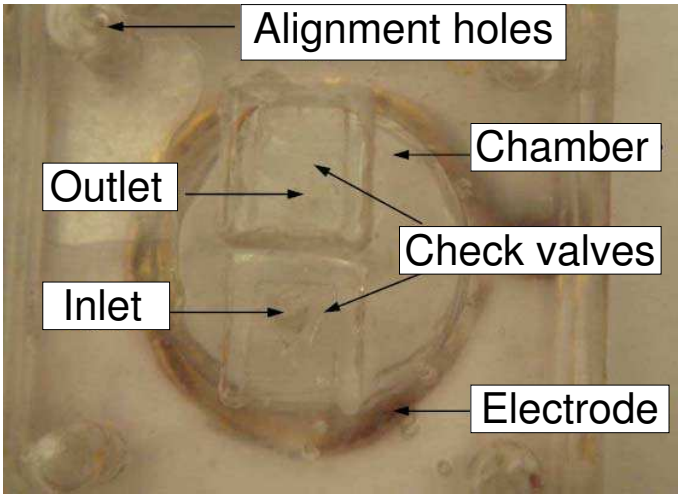

Figure 5.6: A magnified view of the micropump to show the structure.

PPy relating the current I (and thus the charge transferred) to the voltage input U; 2) the electromechanical coupling module of PPy expressing the generated strain ε_m in terms of the transferred charge; and 3) the mechanical module connecting the generated strain to the diaphragm curvature κ or flow rate Φ of the pump, which captures the dynamics of both the PPy membranes and the flap valves. In this thesis, the modules 1) and 2) follows those in Section 2 and therefore will only be briefly reviewed. Module 3) is derived based on an energy-based method, which will be elaborated in detail.

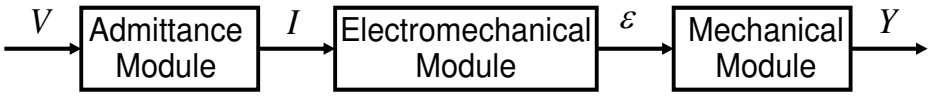

Figure 5.7: The complete model structure for conjugated polymer actuators.

5.2.1 Electrical Admittance Module of PPy

A diffusive-elastic-metal model was proposed for PPy, where it was assumed that the polymer matrix is perfectly conducting and the ion transport within the polymer is solely determined by diffusion [16]. It was adapted to model the ions dynamics in the trilayer beam [6]. The admittance model of a trilayer conjugated polymer was derived as [6]

$$\frac{I(s)}{U(s)} = \frac{s[\frac{\sqrt{D}}{\delta}\tanh(h\sqrt{s/D}) + \sqrt{s}\,]}{\frac{\sqrt{s}}{C} + Rs^{3/2} + R\frac{\sqrt{D}}{\delta}s\tanh(h\sqrt{s/D})}, \tag{5.1}$$

where $U(s)$ and $I(s)$ are the applied voltage and the resulting current in the Laplace domain, respectively, s is the Laplace variable, δ is the double layer thickness, D is the diffusion coefficient, R is the resistance across the trilayer polymer, C is the double-layer capacitance, and h is the thickness of the PPy layer. This infinite-dimensional system can be reduced to the following second-order transfer function

$$\frac{I(s)}{U(s)} \approx \frac{K \cdot s(s+z_1)}{(s+p_1)(s+p_2)}, \tag{5.2}$$

where the parameters are functions of physical parameters [6], which are either known or measurable.

5.2.2 Electromechanical Coupling of PPy

The anions transferred to the polymer cause expansion of the polymer. It can be shown that the strain ε_m introduced by the volumetric change is proportional to the density ρ of the transferred charges [16]:

$$\varepsilon_m = \alpha\rho, \tag{5.3}$$

where α is the strain-to-charge ratio, which varies for different anions. PPy doped with $TFSI^-$ is used in this thesis, and the strain-to-charge ratio is estimated to be 7×10^{-10} $m^3 \cdot C^{-1}$.

Because the double-layer capacitance is much smaller than the bulk capacitance of the PPy polymer, the charges stored in the double layer at the steady state is negligible comparing with those in the bulk. Therefore one can obtain the density $\rho(s)$

$$\rho(s) = \frac{I(s)}{s \cdot A \cdot h}, \tag{5.4}$$

where A is the area of PPy.

5.2.3 Mechanical Module of the Micropump

Given the actuation strain ε_m in the PPy layers, an energy-based method is used to model the deformation of the pump diaphragm and consequently the flow rate. In this method the equilibrium of a mechanical structure is obtained by minimizing a properly defined total energy, and such as approach has been taken to predict the curvature of a composite plate generated by the strain mismatch in different layers [47, 84, 85].

In the following, we first discuss the common framework that applies to both a clamped

whole diaphragm and a petal-shape PPy actuated diaphragm (simply called petal-shaped diaphragm hereafter), and then specialize the discussion to individual cases. There are two relevant energy terms: the elastic energy stored and the work done to the fluid.

The elastic energy of actuation diaphragm will be calculated based on mechanics of constitutive modeling. The analysis holds for both the whole diaphragm and the petal-shaped diaphragm cases, because the infinitesimal elements in both cases experience radial and transverse strains as defined in Fig. 5.8. The diaphragm bends as a result of the deformation of all these elements. The difference between the two cases is that the midplane strain ε_0 depends on the diaphragm curvature κ in the whole diaphragm case because of the edge constrains of the edges, while in the petal-shaped diaphragm case the curvature is not related to the middle plane strain. The latter releases the constrains on the curvature κ from the clamped edge.

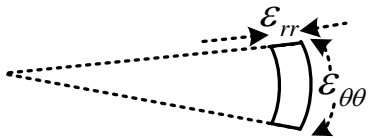

Figure 5.8: Definition of the principal strains.

For small deflection, the principal strains defined in Fig. 5.8 can be expressed as follows [47]:

$$\varepsilon_{rr} = \frac{du}{dr} - z\frac{d^2w}{dr^2} + \varepsilon_s, \tag{5.5}$$

$$\varepsilon_{\theta\theta} = \frac{u}{r} - \frac{z}{r}\frac{dw}{dr} + \varepsilon_s, \tag{5.6}$$

where z is the axis in the thickness direction, ε_s is the swelling strain in different layers (ε_m in the oxidized PPy layer, $-\varepsilon_m$ in the reduced PPy layer, and 0 in the PVDF layer), $u(r)$ and $w(r)$ are the radial and transverse displacements of points in the midplane. Notice that for the case of a petal-shaped diaphragm, there is a very thin PDMS layer underneath the conjugated polymer to seal the chamber, but the Young's modulus of PDMS used in this

thesis is 0.5 MPa, which is much smaller than the Young's modulus of PPy (60 MPa) and PVDF as (612 MPa) [11]. Therefore, the influence of the PDMS layer on the conjugated polymer deformation is ignored, and the midplane is taken to be the middle plane of the PVDF layer.

The displacements $u(r)$ and $w(r)$ in the midplane can be expressed as

$$u = \varepsilon_0 r, \tag{5.7}$$

$$w = \frac{\kappa r^2}{2}, \tag{5.8}$$

where ε_0 represents the strain of the midplane, and κ is the curvature of the plane as shown in Fig. 5.9.

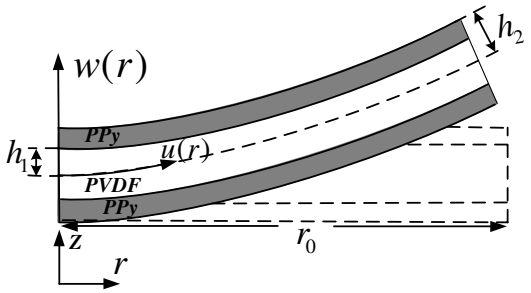

Figure 5.9: The coordinates and geometry definition.

Substituting (5.7) and (5.8) into (5.5) and (5.6), one obtains the following expression

$$\varepsilon_{rr} = \varepsilon_{\theta\theta} = \varepsilon_0 - z \cdot \kappa + \varepsilon_s. \tag{5.9}$$

The corresponding strain energy density is:

$$\begin{aligned} \Psi(r,z) &= \frac{E_i}{2(1-\nu_i^2)}(\varepsilon_{rr}^2 + \varepsilon_{\theta\theta}^2 + 2\nu_i \varepsilon_{rr}\varepsilon_{\theta\theta}) \\ &= \frac{(1+\nu_i)E_i}{1-\nu_i^2}(\varepsilon_0 + \varepsilon_s - z \cdot \kappa)^2, \end{aligned} \tag{5.10}$$

where E_i and ν_i are Young's modulus and Poisson ratio of the material in the i-th layer, which are notated as E_{PPy} and ν_{PPy} for the PPy layers, E_{PVDF} and ν_{PVDF} for the PVDF layer. Finally the total strain energy of the trilayer conjugated polymer is obtained by superimposing three energy densities and integrating over the volume

$$\begin{aligned} W_{elastic} &= \int_{-\pi}^{\pi}\int_{0}^{r_0}[\int_{-h_2}^{-h_1}\frac{(1+\nu_{PPy})E_{PPy}}{1-\nu_{PPy}^2}(\varepsilon_0-\varepsilon_m-z\cdot\kappa)^2dz \\ &+\int_{-h_1}^{h_1}\frac{(1+\nu_{PVDF})E_{PVDF}}{1-\nu_{PVDF}^2}(\varepsilon_0-z\cdot\kappa)^2dz \\ &+\int_{h_1}^{h_2}\frac{(1+\nu_{PPy})E_{PPy}}{1-\nu_{PPy}^2}(\varepsilon_0+\varepsilon_m-z\cdot\kappa)^2dz]rdrd\tau, \end{aligned} \tag{5.11}$$

where r_0 is the undeformed diaphragm radius. Since the whole diaphragm and the petal-shaped diaphragm have the same radius under undeformed configuration, r_0 is used in both cases.

In the whole diaphragm case, the curvature denoted as κ is assumed to be uniform when the diaphragm displacement is small. The geometrical relationship is illustrated in Fig.5.10, where the solid curve represents the sectional view of the middle plane of the deformed diaphragm. The angle θ is obtained as

$$\theta = \arcsin(\kappa r_0). \tag{5.12}$$

One can obtain the strain in the middle plane as

$$\varepsilon_0 = \frac{\frac{\theta}{\kappa}-r_0}{r_0} = \frac{\theta}{\kappa r_0}-1, \tag{5.13}$$

which relates ε_0 and κ.

Since the deformation of the diaphragm will generate the chamber pressure, the work done by the chamber pressure needs to be considered in the energy based method. Considering an incompressible fluid, we have the following equation from the mass conservation

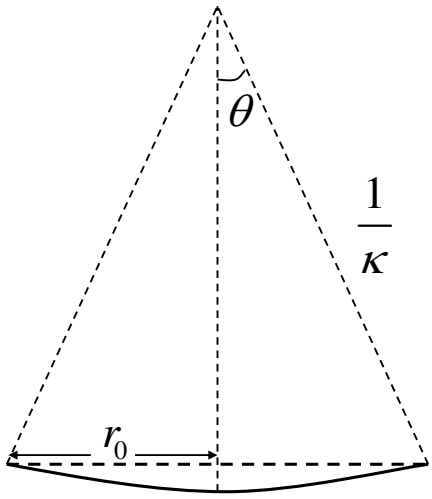

Figure 5.10: Illustration of the geometrical relationship in (5.12) and (5.13), $R = \frac{1}{\kappa}$.

principle,

$$\rho V = \rho \int_0^t (\Phi_{in}(\tau) - \Phi_{out}(\tau)) d\tau, \tag{5.14}$$

where ρ is the density of the fluid, Φ_{in} and Φ_{out} are the flow rates at the inlet and outlet, respectively, with the unit of m^3/s. The relationship between the chamber pressure p and the flow rates is modeled as follows:

$$\frac{dp}{dt} = \frac{1}{C_c}(\Phi_{in} - \Phi_{out}), \tag{5.15}$$

where C_c is the chamber capacitance that can be determined experimentally with the unit of m^3/Pa [86]. Combining (5.14) and (5.15), one can obtain

$$p = \frac{V}{C_c}, \tag{5.16}$$

where $p|_{t=0}$ is considered as 0, since there is no initial net pressure in the chamber. There-

fore, one can express the work done by the diaphragm as

$$\begin{aligned} W_p &= 2\pi \int_0^{r_0} \int_0^{w} p(\tau) d\tau r dr \\ &= \frac{2\pi}{C_c} \int_0^{r_0} \int_0^{w} V d\tau r dr. \end{aligned} \tag{5.17}$$

The total energy is $W = W_{elastic} + W_p$. The equilibrium is reached when $\frac{dW}{d\kappa} = 0$ in the whole diaphragm case, since κ is the only independent variable. In the petal-shaped diaphragm case, the equilibrium is reached when $\frac{\partial W}{\partial \varepsilon_0} = 0$ and $\frac{\partial W}{\partial \kappa} = 0$.

In order to obtain the explicit expressions for both cases, firstly the volume change in the chamber is calculated for the whole diaphragm and petal-shaped diaphragm respectively. In the case of the whole diaphragm, the volume change can be characterized as a dome's volume

$$V = \frac{\pi}{6} h_0 (3r_0^2 + h_0^2), \tag{5.18}$$

where h_0 is the height of the dome that equals $R - \sqrt{R^2 - r_0^2}$ based on the geometry. Substituting this expression into Eq. (5.18), one has

$$\begin{aligned} V &= \frac{\pi}{3}(R - \sqrt{R^2 - r_0^2})(R^2 + r_0^2 - R\sqrt{R^2 - r_0^2}) \\ &\approx \frac{\pi r_0^4}{6} \kappa, \end{aligned} \tag{5.19}$$

where the approximation is based on the Taylor series expansion at $\frac{r_0^2}{R^2} = 0$ for $\sqrt{1 - \frac{r_0^2}{R^2}}$, since the small deflection of the diaphragm implies that $R \gg r_0$.

Substituting (5.19) into (5.17), one can obtain the expression of W_p and consequently W. The equilibrium is reached when $\frac{dW}{d\kappa} = 0$ in the whole diaphragm case, since κ is the

only variable. The equation of $\frac{dW}{d\kappa} = 0$ can be rearranged as follows:

$$\begin{aligned} &-36C_1^2 r_0^2 h_2^2 + (1-\kappa^2 r_0^2)[\frac{\pi r_0^7}{32C_c}\kappa^2 + (C_2 - C_1) r_0 h_1^3 \kappa^2 \\ &+C_1 r_0 h_2^2 (h_2\kappa - 3\varepsilon_m)\kappa + 3C_1 r_0 h_1^2 \varepsilon_m \kappa - 6C_1 r_0 h_2]^2 = 0, \end{aligned} \tag{5.20}$$

where

$$C_1 = \frac{(1+\nu_{PPy})E_{PPy}}{1-\nu_{PPy}^2}, C_2 = \frac{(1+\nu_{PVDF})E_{PVDF}}{1-\nu_{PVDF}^2},$$

The curvature κ can be obtained by numerically solving this polynomial and appropriately choosing the root.

In the petal-shaped diaphragm case, the expressions of volume change V and work W_p are different. As illustrated in Fig. 5.10, the following geometric relationship holds for the petal-shaped diaphragm when the deflection is small,

$$2\theta \cdot \frac{1}{\kappa} = r_0, \tag{5.21}$$

which implies

$$\sin\theta \approx \theta = \frac{r_0\kappa}{2}. \tag{5.22}$$

The volume change in the petal-shaped diaphragm case can be approximated by the shadowed volume (a top-off cone) in Fig. 5.12 under the assumption of (5.22)

$$\begin{aligned} V &= \frac{\pi}{2}(r_0^2 + (r_0 - \sin 2\theta \cdot r_0)^2) \cdot 2\sin^2\theta \cdot r_0 \\ &\approx \frac{\pi r_0^4 \kappa}{4}. \end{aligned} \tag{5.23}$$

The displacement ξ defined in Fig. 5.11 is expressed as

$$\xi = \sin\theta \cdot r_0 \approx \frac{r_0^2\kappa}{2}. \tag{5.24}$$

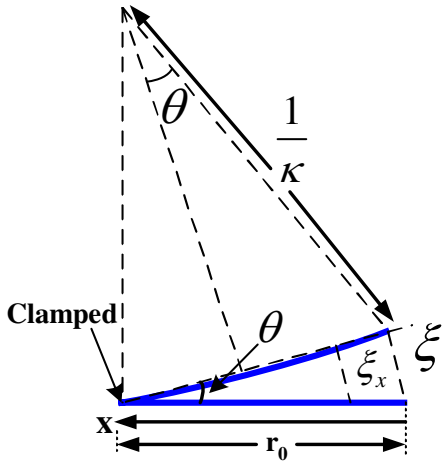

Figure 5.11: Geometric relationship in the calculation of the volume V and the work done by the diaphragm.

The displacement at each point of the diaphragm is defined as ξ_x in Fig. 5.11, which can be expressed in terms of x and ξ as

$$\xi_x = \frac{x}{r_0}\xi = \frac{xr_0\kappa}{2}. \tag{5.25}$$

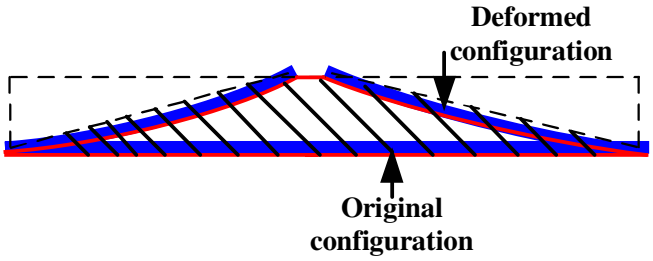

Figure 5.12: Illustration of the volume change under the actuation voltage for the petal-shaped diaphragm.

By substituting (5.23) into (5.17), one can express the work done by the diaphragm as

$$\begin{aligned} W_p &= 2\pi \int_0^{r_0} \int_0^{\xi_x} p(\tau) d\tau r dr \\ &= \frac{\pi^2 r_0^8 \kappa^2}{12 C_c}. \end{aligned} \tag{5.26}$$

The equilibrium is reached when $\frac{\partial W}{\partial \varepsilon_0} = 0$ and $\frac{\partial W}{\partial \kappa} = 0$. Since

$$\begin{aligned}
\frac{\partial W}{\partial \varepsilon_0} &= 4\pi r_0^2 \varepsilon_0 [C_1(h_2 - h_1) + C_2 h_1], && (5.27)\\
\frac{\partial W}{\partial \kappa} &= -4\pi r_0^2 [C_1 \varepsilon_m (h_2^2 - h_1^2) - \frac{C_1 \kappa (h_2^3 - h_1^3)}{3} - \frac{C_2 \kappa h_1^3}{3}] \\
&\quad + \frac{\pi^2 r_0^8 \kappa}{6 C_c}, && (5.28)
\end{aligned}$$

the equilibrium is:

$$\begin{aligned}
\varepsilon_0 &= 0, && (5.29)\\
\kappa &= \frac{3 C_1 \varepsilon_m (h_2^2 - h_1^2)}{C_1 h_2^3 - C_1 h_1^3 + C_2 h_1^3 + \frac{\pi r_0^6}{8 C_c}}. && (5.30)
\end{aligned}$$

Eq. (5.30) captures the static deformation of the diaphragm in terms of ε_m. The material damping effect is introduced as (2.26) to incorporate the dynamics during the deformation process. The values of parameters in (2.26) are kept the same for both PPy and PVDF. Other damping effects in the pump, such as the flap valve damping, are captured by using the equivalent chamber capacitance that includes a damping term

$$C_c'(s) = \frac{C_c}{1 + C_c R_c s}, \tag{5.31}$$

where R_c represents the equivalent damping resistance with the unit of $\mathrm{Pa} \cdot \mathrm{s}/\mathrm{m}^3$.

Thus one can write (5.30) in the Laplace domain as

$$\kappa = H(s) \cdot \varepsilon_m, \tag{5.32}$$

where

$$H(s) = \frac{3 C_1 (h_2^2 - h_1^2)}{C_1 h_2^3 - C_1 h_1^3 + C_2 h_1^3 + \frac{3\pi r_0^5}{8 C_c'}},$$

and C_1, C_2, and $C_c\prime$ are the frequency-dependent terms, because the Young's moduli in (5.30) are replaced by the ones in (2.26).

5.2.4 Complete Model

One can obtain the complete model for the petal-shaped diaphragm in an analytical form by combining (5.2), (5.3) and (5.32), which is shown as follows:

$$\frac{\kappa(s)}{U(s)} = \frac{\alpha K \cdot (s+z_1)H(s)}{A(h_2-h_1)\cdot s(s+p_1)(s+p_2)}. \tag{5.33}$$

Note that $h = h_2 - h_1$ in (5.2). However,the complete analytical model for the whole diaphragm is not easy to obtain due to the complexity of (5.20). Therefore, the model prediction in that case is obtained by numerically solving (5.20).

Considering (5.14) and (5.23), one gets

$$\Phi_{in} - \Phi_{out} = \frac{\pi r_0^4}{4} \cdot s \cdot \kappa. \tag{5.34}$$

Combining (5.33) and (5.34), one can furthermore obtain the transfer function model from the voltage input to the flow rate:

$$\frac{\Phi_{in}(s) - \Phi_{out}(s)}{U(s)} = \frac{\pi r_0^4 \alpha K \cdot (s+z_1)H(s)}{4A(h_2-h_1)\cdot (s+p_1)(s+p_2)}. \tag{5.35}$$

5.3 Experimental Results

A trilayer PPy circular actuator is used in the experiments, with the radius r_0 of 10 mm. The curvature is measured by a laser sensor (OADM 20I6441/S14F, Baumer Electric Inc) with a resolution of 5 μm. The model parameter R is identified by applying a high-frequency (100 Hz) sinusoidal input $U\sin(\omega t)$. From (2.12), the impedance approaches R as $\omega \to \infty$. To measure the parameter C, a step voltage is applied and the transferred charge into the

PPy layer is computed by integrating the charging current. The calculation details can be found in [6]. Finally, the resistance and capacitance are identified to be: $R = 27\ \Omega$, $C = 8.69 \times 10^{-5}$ F. The diffusion coefficient D is chosen to be 2×10^{-10} m^2/s based on [16]. The double-layer thickness δ is estimated to be 25 nm based on [18].

5.3.1 Admittance

Since cutting does not influence the electrical property of conjugated polymer, (2.12) is used to predict the admittance of both the whole diaphragm and the petal-shape diaphragm. The comparison is shown in Fig. 5.13, where a good match of admittance is seen between the model and the experimental results.

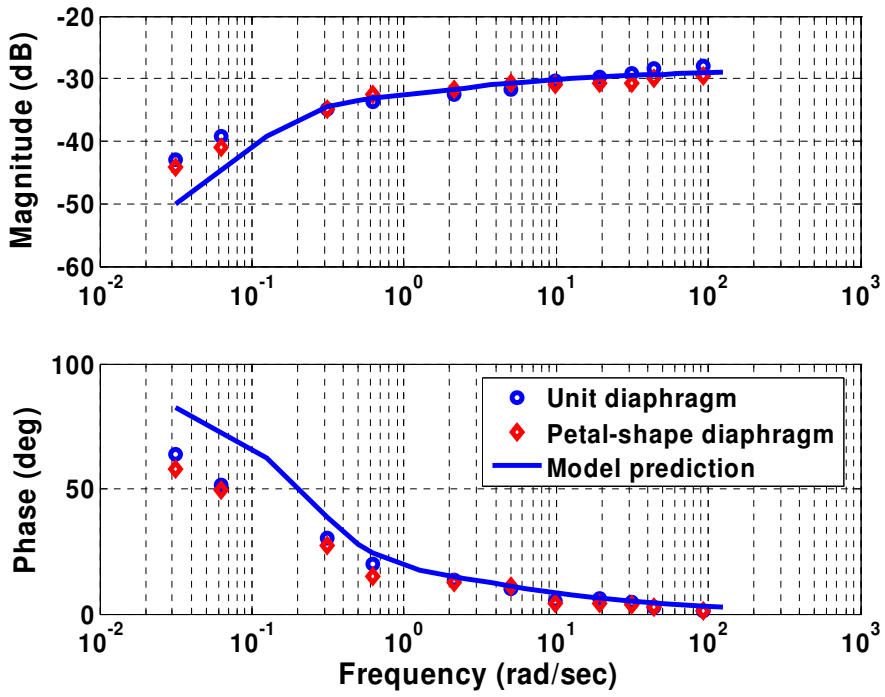

Figure 5.13: Comparison of model prediction from (2.12) with the experimental results for the whole diaphragm and the petal-shaped diaphragm.

5.3.2 Displacement

In experiments the displacement at the center of the diaphragm is measured by a laser distance sensor. The predicted curvature of the petal-shape diaphragm from (5.33) is used to calculate the displacement based on the following equation [6]:

$$y = \frac{\kappa l^2}{2}, \tag{5.36}$$

where l is the distance between the clamped end and the laser incident point when the beam is at rest, which is r_0 minus 1 mm in the setup.

The predicted displacements for the petal-shape diaphragm are compared with the experimental results when there is no water in the pump (Fig. 5.14) and when pumping water (Fig. 5.15). There the actuation voltage applied is sinusoidal with an amplitude of 4 V and with different frequencies. All the other parameters in (5.33) are given or identified in the previous admittance model experiments. C_c and R_c can be determined by fitting the experimental data for petal-shaped diaphragm. They are identified as $C_c = 1.02 \times 10^{-8}$ m^3/Pa and $R_c = 3 \times 10^8$ $\mathrm{Pa} \cdot \mathrm{s}/\mathrm{m}^3$. To predict the results when there is no water in pump, the parameters C_c and R_c are set to be ∞ and 0 respectively, which sets the fluid energy to be zero to eliminate the fluid energy term. Thus the curvature is merely determined by the equilibrium of elastic energy. The experimental results for the whole diaphragm case are also compared with the numerical solution of (5.2), (5.3), and (5.20). The result when there is no water is shown in Fig. 5.16, while the result when pumping water is shown in Fig. 5.17. The actuation voltage is 4 V. It can be seen that the petal-shaped diaphragm can generate almost 10 times larger displacment than the whole diaphragm when there is no water in the chamber. When pumping water, the displacement of the petal-shaped diaphragm is almost 3 times larger than the whole diaphragm. These experimental results here proved the effectiveness of the petal-shaped diaphragm design in alleviating the constrains from the clamped edge.

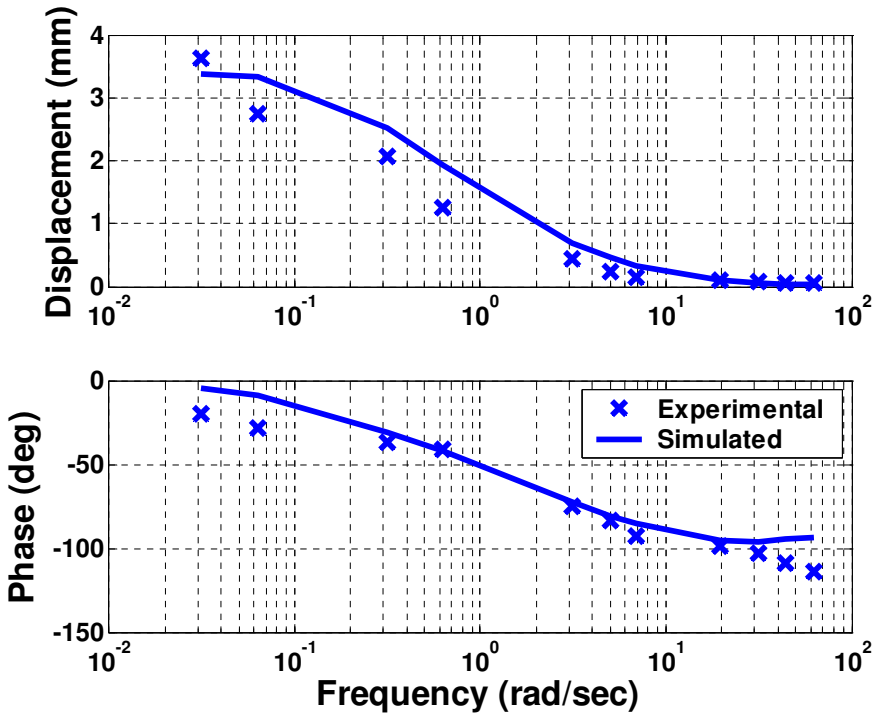

Figure 5.14: Comparison of model prediction from (5.33) with the experimental results for the petal-shaped diaphragm when there is no water (actuation voltage amplitude 4 V).

5.3.3 Flow Rate

The flow rates of the petal-shaped diaphragm pump are measured and compared with the model prediction (5.35) for an actuation voltages of 3 V (Fig. 5.18) and 4 V (Fig. 5.19). It can be seen that the model can predict the experimental results well under different input voltages. The frequency to achieve highest flow rate is 0.5 Hz, which is also predicted well by the model. When the frequency of the input voltage is low, the flow rate is small due to the slow movement of the pump. The flow rate will increase as operating frequency increases. However, the flow rate will decrease as frequency becomes higher, because of the damping effect of the flap valves and the declining response of conjugated polymer actuator at high frequencies. Thus the model (5.35) can facilitate the design optimization and the feedback control of the flow rate.

we have also tested the pumping performance of the whole diaphragm. However, the

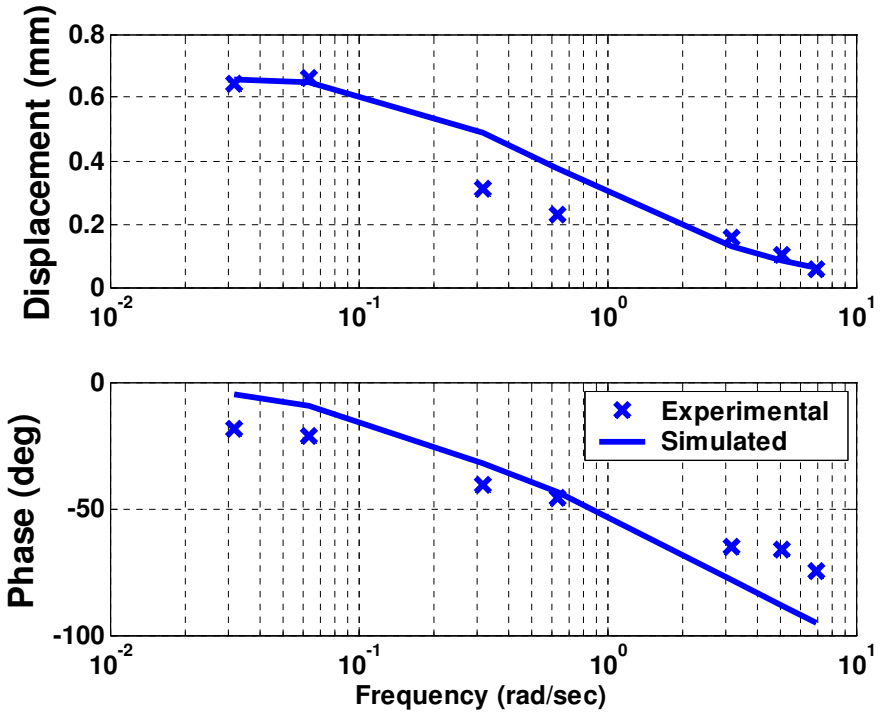

Figure 5.15: Comparison of model prediction from (5.33) with the experimental results for the petal-shaped diaphragm when pumping water (actuation voltage amplitude 4 V).

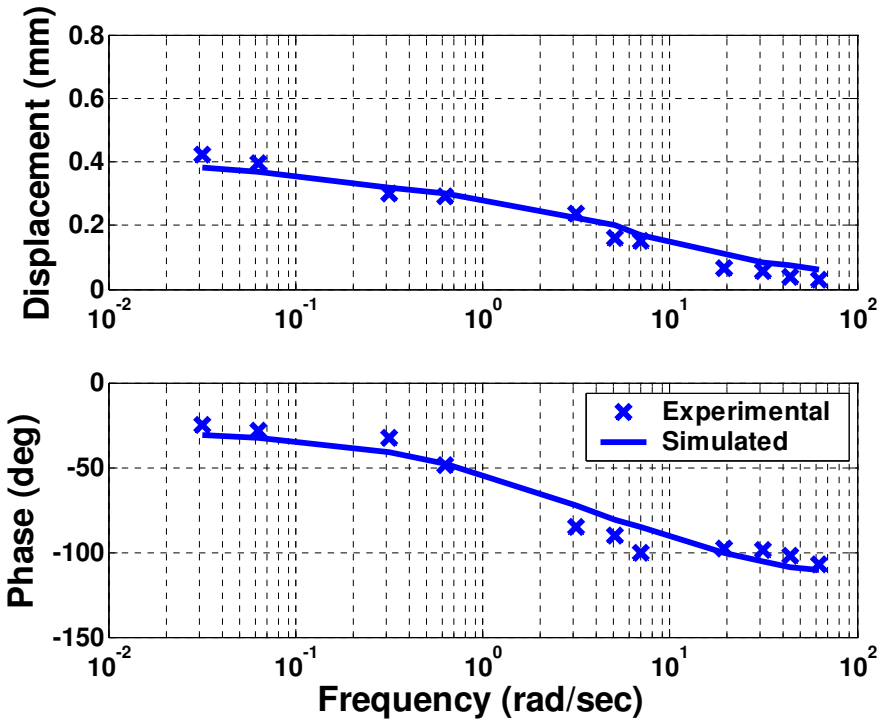

Figure 5.16: Comparison of model prediction with the experimental results for the whole diaphragm when there is no water by numerically solving (5.20) (actuation voltage amplitude 4 V).

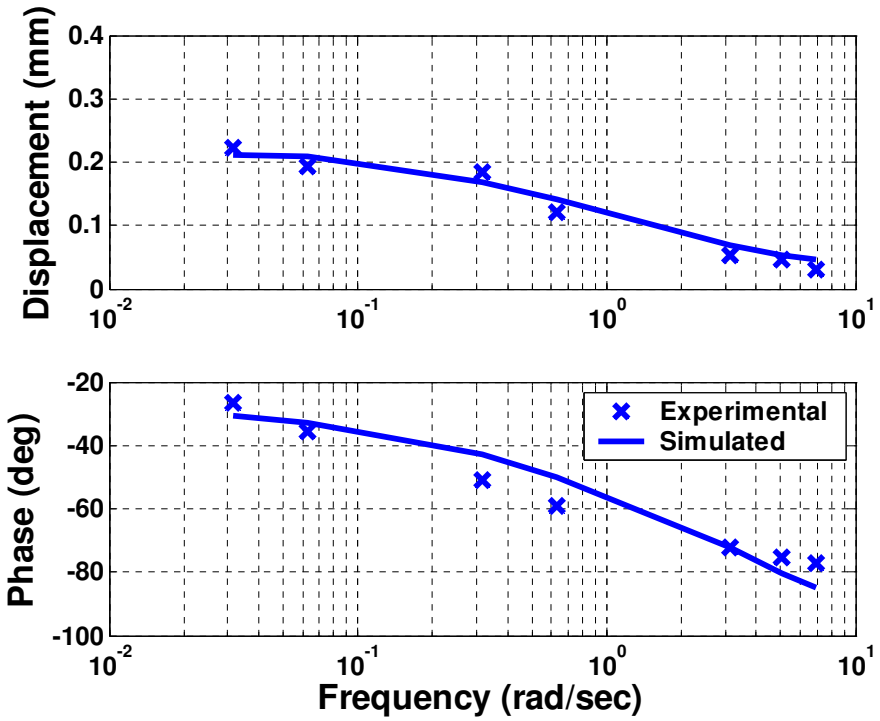

Figure 5.17: Comparison of model prediction with the experimental results for the whole diaphragm when pumping water by numerically solving (5.20) (actuation voltage amplitude 4 V).

flow rate is barely observable in that case.

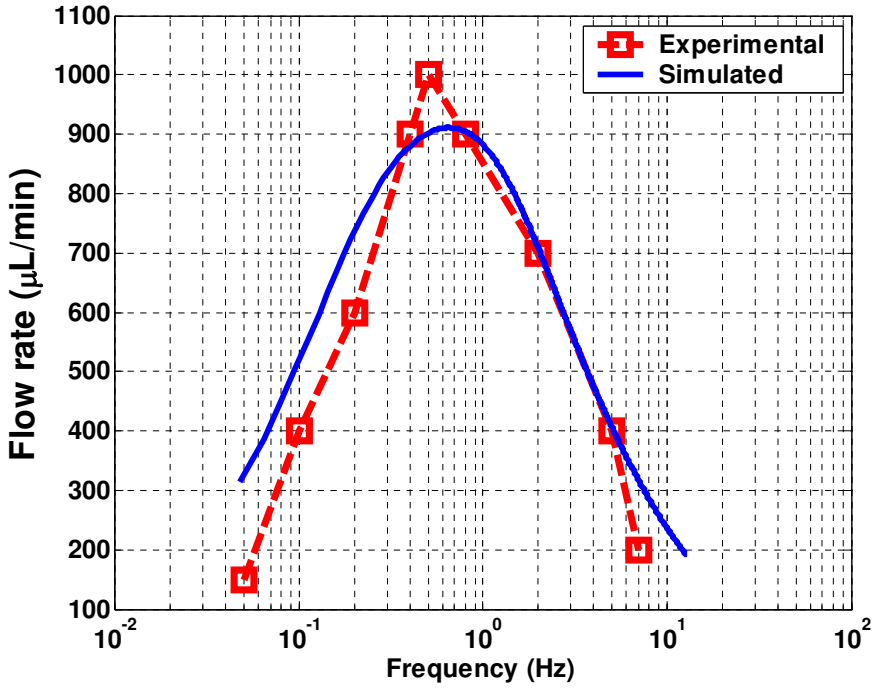

Figure 5.18: Flow rate of the micropump at different frequencies when input voltage magnitude is 3 V.

5.4 Chapter Summary

In this thesis, circular conjugated polymer actuators are investigated for potential micropump applications. A petal-shaped diaphragm design is proposed to alleviate the constrains from the clamped edge. An analytical model is proposed that captures the relationship between the actuation voltage and the diaphragm deformation/flow rate. Experiments are conducted to verify the model and identify the parameters. The largest flow rate achieved in the current experimental setup is 1260 μL/min, when the operating frequency is 0.53 Hz. For comparison, modeling analysis and experiments are also conducted on the whole diaphragm case. The model predicted much smaller diaphragm deformation compared with the petal-shaped diaphragm, which is also verified in experiments.

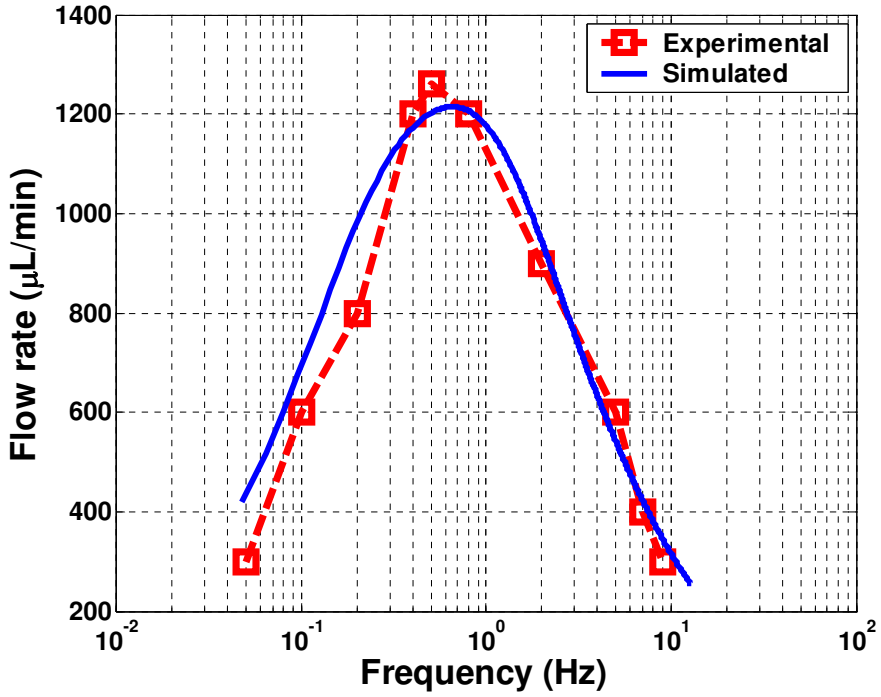

Figure 5.19: Flow rate of the micropump at different frequencies when input voltage magnitude is 4 V.

Chapter 6

Conclusion

In this dissertation, we have focused on modeling, control, and application of conjugated polymer actuators and sensors. Experiments have been conducted to validate the modeling approach. Model-based control strategies are then proposed to control conjugated polymer actuators. The application of conjugated polymer in micropump is investigated from both modeling and experiment perspectives.

The contributions of this dissertation on the modeling aspect include two main parts. The first part is the development of a scalable, low-order transfer function model for conjugated polymer actuators that captures the major sophisticated electrochemomechanical dynamics, but is still control-oriented and therefore suitable for real-time control. This model is obtained by ignoring high-frequency dynamics in an infinite-dimensional model. The proposed model provides the theoretical basis for the adaptive control scheme.

The second part is modeling of the nonlinearities existing in electrical and mechanical domains. The coupling of redox level change with ions migration in conjugated polymer is considered as the main source of nonlinearity in electrical dynamics. A partial differential equation (PDE) that governs its electrochemical dynamics is proposed and solved to address the nonlinear electrical property of conjugated polymer. The mechanical nonlinearity of conjugated polymer actuator is also investigated. Instead of using the elastic modulus

as in the linear elasticity theory, we use a nonlinear strain energy function to capture the stored elastic energy under actuation-induced swelling, which further allows us to compute the induced stress even under large actuation voltage. The proposed framework can also be applied to the analysis of large deformations in some other electroactive polymers.

We have presented a fiber-directed conjugated polymer actuator that can generate torsional motion, which is due to the anisotropy associated with the interaction between the fiber and the material matrix. The nonlinear elasticity-based model is utilized to capture the actuator performance. The effectiveness of the model is verified through comparison with experimental results.

Besides modeling on actuation performance of conjugated polymer, the electromechanical sensing behavior of conjugated polymer is experimentally characterized and mathematically modeled as well. A theory for the sensing mechanism is proposed by postulating that, through its influence on the pore structure, mechanical deformation correlates directly to the concentration of ions at the PPy/PVDF interface. This provides a key boundary condition for the partial differential equation (PDE) governing the ion diffusion and migration dynamics. An analytical model is then obtained in the form of a transfer function that relates the open-circuit sensing voltage to the mechanical input.

We have proposed an effective adaptive control strategy for conjugated polymer actuators based on our control-oriented model. A recursive least-squares algorithm is used to identify online the parameters of the transfer function model, which captures the essential actuation dynamics that varies significantly with time. A self-tuning regulator is designed based on the identified parameters to form the closed-loop control system. A parameter projection step ensures that the parameter estimates stay within the physically-meaningful region, and thus makes the system robust against noises and unmodeled dynamics.

The application of conjugated polymer as a micropump is investigated. We have proposed a diaphragm micropump actuated by conjugated polymer in a petal-shape design to alleviate the edge constrains. Transfer function models from the actuation voltage to the

diaphragm deflection and flow rate are obtained. The pump body is fabricated through MEMS fabrication process to miniaturize the pump size. Experiments are conducted to evaluate the micropump performance. The effectiveness of the transfer function models are also verified by the experiments, which will facilitate design optimization and the use of feedback control tools in dealing with the complicated behavior of conjugated polymer actuators.

There are several interesting directions to expand the work in this dissertation.

Firstly, although adaptive control scheme we proposed has shown its superiority in overcoming the time-varying effects, its application is constrained in the linear range. The actuation voltage magnitude has been tuned small so that the change of redox level with actuation voltage can be ignored. The nonlinearity will impair the performance of the control system based on the linear model. We have proposed nonlinear models to capture the significant nonlinearities in conjugated polymers in both electrical and mechanical domains. An interesting research direction is to apply nonlinear control schemes based on the nonlinear models of conjugated polymer actuator to achieve better performance, when the nonlinearities become significant, i.e., large deformation under large actuation voltage.

Another direction is to further pursue the application of conjugated polymer in microfluid medical devices that are experiencing significant development recently. A micropump based on conjugated polymer actuator has been investigated in this dissertation. We have built and tested the prototype of micropump. The model relating the flow rate to the actuation voltage is also proposed. It is meaningful to design feedback control system based on the proposed model to overcome the performance decaying of conjugated polymer, which would allow the conjugated polymer micropump to deliver desired and accurate fluid for a long period of time.

BIBLIOGRAPHY

[1] E. Smela, O. Inganas, and I. Lundstrom, "Controlled folding of micro-size structures," *Science*, vol. 268, pp. 1735–1738, 1995.

[2] E. W. H. Jager, O. Inganas, and I. Lunstrom, "Microrobots for micrometer-size objects in aqueous media: Potential tools for single cell manipulation," *Science*, vol. 288, pp. 2335–2338, 2000.

[3] J. Zhou, H. Chan, T. To, K. Lai, and W. J. Li, "Polymer MEMS actuators for underwater micromanipulation," *IEEE/ASME Transactions on Mechatronics*, vol. 9, no. 2, pp. 334–342, 2004.

[4] A. Mazzoldi and D. De Rossi, "Conductive-polymer-based structures for a steerable catheter," in *Smart Structures and Materials 2000: Electroactive Polymer Actuators and Devices*, Y. Bar-Cohen, Ed. Bellingham, WA: SPIE - The International Society for Optical Engineering, 2000, pp. 273–280.

[5] Z. Chen and X. Tan, "A dynamic model for ionic polymer-metal composite sensors," *Smart Materials and Structures*, vol. 16, pp. 1477–1488, 2007.

[6] Y. Fang, X. Tan, and G. Alici, "Robust adaptive control of conjugated polymer actuators," *IEEE Transactions on Control Systems Technology*, vol. 16, pp. 600–612, 2008.

[7] R. Baughman, "Conducting polymer artificial muscles," *Synthetic Metals*, vol. 78, pp. 339–353, 1996.

[8] E. Smela, "Conjugated polymer actuators for biomedical applications," *Journal of Advanced Materials*, vol. 15, no. 6, pp. 481–494, 2003.

[9] G. G. Wallace, G. M. Spinks, L. Kane-Maguire, and P. R. Teasdale, *Conductive Electroactive Polymers: Intelligent Materials Systems (2nd Edition)*. Boca Raton, FL: CRC Press LLC, 2003.

[10] A. Della Santa, D. De Rossi, and A. Mazzoldi, "Characterization and modelling of a conducting polymer muscle-like linear actuator," *Smart Materials and Structures*, vol. 6, pp. 23–34, 1997.

[11] G. Alici, B. Mui, and C. Cook, "Bending modeling and its experimental verification for conducting polymer actuators dedicated to manipulation applications," *Sensors and Actuators A*, vol. 126, pp. 396–404, 2006.

[12] J. Janata and M. Josowicz, "Conducting polymers in electronic chemical sensors," *NATURE MATERIALS*, vol. 2, pp. 19–24, 2003.

[13] G. Alici, P. Metz, and G. M. Spinks, "A methodology towards geometry optimization of high performance polypyrrole (PPy) actuators," *Smart Materials and Structures*, vol. 15, pp. 243–252, 2006.

[14] G. Alici and N. N. Huynh, "Predicting force output of trilayer polymer actuators," *Sensors and Actuators A*, vol. 132, no. 2, pp. 616–625, 2006.

[15] M. Christophersen, B. Shapiro, and E. Smela, "Characterization and modeling of PPy bilayer microactuators. Part 1. curvature," *Sensors and Actuators B*, vol. 115, pp. 596–609, 2006.

[16] J. D. W. Madden, "Conducting polymer actuators," PhD thesis, MIT, 2000.

[17] P. G. A. Madden, "Development and modeling of conducting polymer actuators and the fabrication of a conducting polymer based feedback loop," PhD thesis, MIT, 2003.

[18] Y. Fang, X. Tan, Y. Shen, N. Xi, and G. Alici, "A scalable model for trilayer conjugated polymer actuators and its experimental validation," *Materials Science and Engineering C: Biomimetic and Supramolecular Systems*, vol. 28, pp. 421–428, 2008.

[19] G. Alici, B. Mui, and C. Cook, "Characterisation and bending modeling of conducting polymer actuators for use in micro/nano manipulation," in *Proceedings of the IEEE International Conference on Robotics and Biomimetics*, 2005, pp. 560–565.

[20] Y. Wu, G. Alici, J. D. Madden, G. M. Spinks, and G. G. Wallace, "Soft mechanical sensors through reverse actuation in polypyrrole," *Advanced Functional Materialss*, vol. 17, pp. 3216–3222, 2007.

[21] W. Takashima, K.Hayasi, and K. Kaneto, "Force detection with Donnan equilibrium in polypyrrole film," *Electrochemistry Communications*, vol. 9, pp. 2056–2061, 2007.

[22] T. Skotheim and J. Reynolds, *Conjugated Polymers: Processing and Applications*, 3rd ed. CRC Press, 2006.

[23] D. L. Boxall and R. A. Osteryoung, "Switching potentials and conductivity of polypyrrole films prepared in the ionic liquid 1-butyl-3-methylimidazolium hexafluorophosphate," *Journal of The Electrochemical Society*, vol. 151, no. 2, pp. E41–E45, 2004.

[24] H. Mao and P. Pickup, "In situ measurement of the conductivity of polypyrrole and poly[1-methyl-3-(pyrrol-1-ylmethyl)pyridinium]$^+$ as a function of potential by mediated voltammetry. redox conduction or electronic conduction?" *Journal of American Chemical Society*, vol. 112, pp. 1776–1782, 1990.

[25] G. Spinks, L. Liu, G. Wallace, and D. Zhou, "Strain response from polypyrrole actuators under load," *Advanced Functional Materials*, vol. 12, pp. 437 – 440, 2002.

[26] D. D. Rossia, A. D. Santaa, and A. Mazzoldia, "Performance and work capacity of a polppyrrole conducting polymer linear actuator," *Synthetic Metals*, vol. 90, pp. 93–100, 1997.

[27] Q. Pei and O. Inganäs, "Electrochemlcal appllcatlons of the bending beam method. 1. mass transport and volume changes in polypyrrole during redox," *Journal of Physical Chemistry*, vol. 96, pp. 10 507–10 514, 1992.

[28] P. Metza, G. Alici, and G. Spinks, "A finite element model for bending behaviour of conducting polymer electromechanical actuators," *Sensors and Actuators A*, vol. 130-131, pp. 1–11, 2006.

[29] J. D. Madden, D. Rinderknecht, P. A. Anquetil, and I. W. Hunter, "Creep and cycle life in polypyrrole actuators," *Sensors and Actuators: A. Physical*, vol. 133, pp. 210–217, 2007.

[30] T. F. Otero, J. J. L. Cascales, and G. V. Arenas, "Mechanical characterization of free-standing polypyrrole film," *Materials Science and Engineering: C*, vol. 27, pp. 18–22, 2007.

[31] H. Tsai, T. J. Pence, and E. Kirkinis, "Swelling induced finite strain flexure in a rectangular block of an isotropic elastic material," *Journal of Elasticity*, vol. 75, pp. 69–89, 2004.

[32] Y. Fang, X. Tan, and G. Alici, "Robust adaptive control of conjugated polymer actuators," *IEEE Transactions on Control Systems Technology*, vol. 14, no. 6, pp. 600–612, 2008.

[33] H. Demirkoparan and T. J. Pence, "Torsional swelling of a hyperelastic tube with helically wound reinforcement," *Journal of Elasticity*, vol. 92, pp. 61–90, 2007.

[34] P. G. A. Madden, J. D. W. Madden, P. A. Anquetil, N. A. Vandesteeg, and I. W. Hunter, "The relation of conducting polymer actuator material properties to performance," *IEEE Journal of Oceanic Engineering*, vol. 29, pp. 696–705, 2004.

[35] B. Qi, W. Lu, and B. R. Mattes, "Control system for conducting polymer actuators," in *Smart Structures and Materials 2002: Electroactive Polymer Actuators and Devices (EAPAD)*, Y. Bar-Cohen, Ed. Bellingham, WA: SPIE - The International Society for Optical Engineering, 2002, pp. 359–366.

[36] T. A. Bowers, "Modeling, simulation, and control of a polypyrrole-based conducting polymer actuator," Master's thesis, Massachusetts Institute of Technology, 2004.

[37] K. J. Astrom and B. Wittenmark, *Adaptive Control*, 2nd ed. Addison-Wesley, 1995.

[38] T. S. Hansen, K. West, O. Hassager, and N. B. Larsen, "An all-polymer micropump based on the conductive polymer poly(3,4-ethylenedioxythiophene) and a polyurethane channel system," *Journal Of Micromechanics And Microengineering*, vol. 17, pp. 860–866, 2007.

[39] D. J. Laser and J. G. Santiago, "A review of micropumps," *Journal of Micromechanics and Microengineering*, vol. 14, p. R35CR64, 2004.

[40] A. Wego, H.-W. Glock, L. Pagel, and S. Richter, "Investigations on thermo-pneumatic volume actuators based on pcb technology," *Sensors and Actuators A: Physical*, vol. 93, pp. 95–102, 2001.

[41] R. Zengerle, M. Richter, F. Brosinger, A. Richter, and H. Sandmaier, "Performance simulation of microminiaturized membrane pumps," *7th International Conference on Solid-State Sensors and Actuators*, p. 106C109, 1993.

[42] J. G. Smits, "Piezoelectric micropump with three valves working peristaltically," *Sensors and Actuators A: Physical*, vol. 21, pp. 203–206, 1990.

[43] T.-B. Xu and J. Su, "Development, characterization, and theoretical evaluation of electroactive polymer-based micropump diaphragm," *Sensors and Actuators A: Physical*, vol. 121, pp. 267–274, 2004.

[44] W. Benard, H. Kahn, and A. Heuer, "Thin-film shape-memory alloy actuated micropumps," *Journal of Microelectromechanical Systems*, vol. 7, pp. 245–251, 1998.

[45] J. H. Kim, K. T. Lau, R. Shepherd, Y. Wu, G. Wallace, and D. Diamond, "Performance characteristics of a polypyrrole modified polydimethylsiloxane (pdms) membrane based microfluidic pump," *Sensors and Actuators A: Physical*, vol. 148, pp. 239–244, 2008.

[46] T. T. Nguyena, N. S. Goob, V. K. Nguyenc, Y. Yoo, and S. Park, "Design, fabrication, and experimental characterization of a flap valve ipmc micropump with a flexibly supported diaphragm," *Sensors and Actuators A: Physical*, vol. 141, pp. 640–648, 2008.

[47] L. B. Freund, J. A. Floro, and E. Chason, "Extensions of the stoney. formula for substrate curvature to configurations with thin. substrate or large deformations," *Applied Physics Letters*, vol. 74, pp. 1987–1989, 1999.

[48] Y. Fang, X. Tan, and G. Alici, "Robust adaptive control of conjugated polymer actuators," *IEEE Transactions on Control Systems Technology*, vol. 16, pp. 600–612, 2008.

[49] P. Magnusson, G. Alexander, V. Tripathi, and A. Weisshaar, *Transmission Lines and Wave Propagation*, 4th ed. CRC Press, 2001.

[50] G. F. Franklin, J. D. Powell, and A. Emami-Naeini, *Feedback Control of Dynamic Systems*, 5th ed. Upper Saddle River, NJ: Pearson Education, Inc., 2006.

[51] S. Satyanarayana, "Surface stress and capacitive MEMS sensor arrays for chemical and biological sensing," PhD thesis, University of California, Berkeley, 2005.

[52] C. O. Yoon, M. Reghu, D. Moses, and A. J. Heeger, "Transport near the metal-insulator transition: Polypyrrole doped with PF_6," *Physical Review B (Condensed Matter)*, vol. 49, pp. 10 851–10 863, 1994.

[53] T. F. Otero and J. M. Sansinena, "Bilayer dimensions and movement in artificial muscles," *Bioelectrochemistry and Bioenergetics*, vol. 42, no. 2, pp. 117–122, 1997.

[54] I. Ward, *Mechanical Properties of Solid Polymers*. Wiley, 1979.

[55] Y. Shen, N. Xi, K. W. C. Lai, and W. J. Li, "A novel PVDF micro force/force rate sensor for practical application in micromanipulation," *Sensor Review*, vol. 24, pp. 274–283, 2006.

[56] N. Lakshminarayanaiah, *Transport Phenomena in Membranes*. Academic Press, 1969.

[57] H. Mao, J. Ochmanska, C. Paulse, and P. Pickup, "Ion transport in pyrrole-based polymer films," *Faraday Discussions of the Chemical Society*, vol. 88, pp. 165–176, 1989.

[58] Y. Wu, G. Alici, G. M. Spinks, and G. G. Wallace, "Fast trilayer polypyrrole bending actuators for high speed applications," *Synthetic Metals*, vol. 156, pp. 1017–1022, 2006.

[59] G. Phillips, R. Suresh, J. Waldman, J. Kumar, J. I-Chen, S. Tripathy, and J. Huang, "Dielectric property of polypyrrole doped with tosylate anion in the far infrared and microwave," *Journal of Applied Physics*, vol. 69, pp. 899–905, 1991.

[60] F. Legros and A. Fourrier-Lamer, "Dielectric property of doped polypyrrole in the 5 hz - 1 ghz frequency range," *Materials Research Bulletin*, vol. 19, pp. 1109–1117, 1984.

[61] S. Saafan, M. El-Nimr, and E. El-Ghazzawy, "Study of dielectric properties of polypyrrole prepared using two different oxidizing agents," *Journal of Applied Polymer Science*, vol. 99, pp. 3370–3379, 2006.

[62] B. Chapman, R. Buckley, N. Kemp, A. Kaiser, D. Beaglehole, and H. Trodahl, "Low-energy conductivity of PF_6^--doped polypyrrole," *Physical Review B (Condensed Matter)*, vol. 60, pp. 13 479–13 483, 1999.

[63] D. W. Wang, H. S. Tzou, and H.-J. Lee, "Control of nonlinear electro/elastic beam and plate systems (finite element formulation and analysis)," *Journal of Vibration and Acoustics*, vol. 126, pp. 63–70, 2004.

[64] S. Sathiyanarayan, S. M. Sivakumar, and C. L. Rao, "Nonlinear and time-dependent electromechanical behavior of polyvinylidene fluoride," *Smart Materials And Structures*, vol. 15, pp. 767–781, 2006.

[65] J. Bonet and R. Wood, *Nonlinear continuum mechanics for finite element analysis*. Cambridge University Press, 1997.

[66] L. Treloar, *The Physics of Rubber Elasticity*. Oxford Press, 1975.

[67] R. C. Batra and T. S. Geng, "Enhancement of the dynamic buckling load for a plate by using piezoceramic actuators," *Smart Materials And Structures*, vol. 10, pp. 925–933, 2001.

[68] J. S. Yang and R. C. Batra, "A second-order theory for piezoelectric materials," *Journal of Acoustical Society of America*, vol. 97, pp. 280–288, 1995.

[69] S. Nemat-Nasser and Y. Wu, "Tailoring the actuation of ionic polymercmetal composites," *Smart Materials And Structures*, vol. 15, pp. 909–923, 2006.

[70] T. J. Pence and H. Tsai, "Swelling induced cavitation of elastic spheres," *Mathematics and Mechanics of Solids*, vol. 11, pp. 527–551, 2006.

[71] J. Merodio and R. W. Ogden, "Mechanical response of fiber-reinforced incompressible non-linearly elastic solids," *International Journal of Non-Linear Mechanics*, vol. 40, pp. 213–227, 2005.

[72] Z. Guo, X. Peng, and B. Moran, "Mechanical response of neo-hookean fiber reinforced incompressible nonlinearly elastic solids," *International Journal of Solids and Structures*, vol. 44, pp. 1949–1969, 2006.

[73] J. Ding, L. Liu, G. M. Spinks, D. Zhou, G. G. Wallace, and J. Gillespie, "High performance conducting polymer actuators utilising a tubular geometry and helical wire interconnects," *Synthetic Metals*, vol. 138, pp. 391–398, 2003.

[74] S. Therkelsen, "Constitutive modeling of active polymers," Master thesis, MIT, 2005.

[75] G. Qiu and T. Pence, "Remarks on the behavior of simple directionally reinforced incompressible nonlinearly elastic solids authors," *Journal of Elasticity*, vol. 49, pp. 1–30, 1997.

[76] K. Chen, L. Zhao, J. Tse, and J. Rodgers, "Elastic properties of platinum rh and rh3x compounds," *Physics Letter A*, vol. 331, pp. 400–403, 2004.

[77] C. Ho, I. Raistrick, and R. Huggins, "Application of a-c techniques to the study of lithium diffusion in tungsten trioxide thin films," *Journal of The Electrochemical Society*, vol. 127, pp. 343–350, 1980.

[78] Y. Bar-Cohen, "Electroactive polymers as artificial muscles – reality and challenges," in *Proceedings of the 42nd American Institute of Aeronautics and Astronautics*, 2001, pp. 2001–1492.

[79] W. Dunham, *Journey Through Genius: The Great Theorems of Mathematics*. John Wiley & Sons Inc., 1990.

[80] S. M. Naik, P. R. Kumar, and B. E. Ydstie, "Robust continuous-time adaptive control by parameter projection," *IEEE Transaction on Automatic Control*, vol. 37, no. 2, pp. 182–197, 1992.

[81] S. M. Naik and P. R. Kumar, "Robust indirect adaptive control of time-varying plants with unmodeled dynamics and disturbances," *SIAM Journal on Control and Optimization*, vol. 32, no. 6, pp. 1696–1725, 1994.

[82] G. Alici, P. Metz, and G. M. Spinks, "A methodology towards geometry optimisation of high performance polypyrrole (ppy) actuators," *Smart Materials and Structures*, vol. 15, pp. 243–252, 2006.

[83] D. Armani, C. Liu, and N. Aluru, "Re-configurable fluid circuits by pdms elastomer micromachining," *the 12th. IEEE International Conference on Micro Electro Mechanical Systems*, pp. 222–227, 1999.

[84] S. Huang and X. Zhang, "Extension of the stoney formula for film-substrate systems with gradient stress for mems applications," *Journal Of Micromechanics And Microengineering*, vol. 16, pp. 382–389, 2006.

[85] V. T. Srikar and S. M. Spearing, "A critical review of microscale mechanical testing methods used in the design of microelectromechanical systems," *Experimental Mechanics*, vol. 43, pp. 238–247, 2003.

[86] R. Bardell, N. Sharma, F. Forster, M. Afromowitz, and R. Penney, "Designing high-performance micro-pumps based on no-moving-parts valves," *Microelectromechanical Systems (MEMS), ASME*, vol. 62, pp. 47–53, 1997.